

**The Statistical Convergence of Spatial Variations in
Aerosol Deposition**

by

James C. Moran

B.S.M.E., University College Dublin (1994)

Submitted to the Department of Mechanical Engineering
in partial fulfillment of the requirements for the degree of

Master of Science in Mechanical Engineering

at the

MASSACHUSETTS INSTITUTE OF TECHNOLOGY

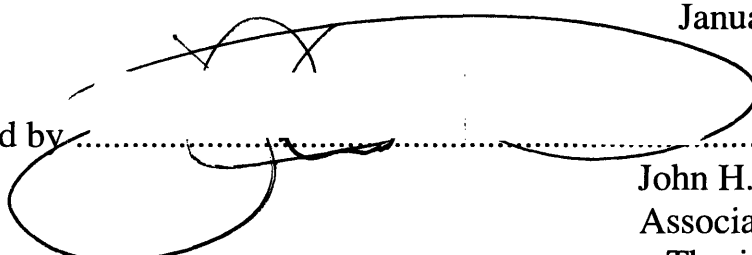
February 1996

© Massachusetts Institute of Technology, 1996. All Rights Reserved.

Author

Department of Mechanical Engineering
January 15, 1996

Certified by


John H. Lienhard V
Associate Professor
Thesis Supervisor

Accepted by


Ain A. Sonin
Chairman, Departmental Committee on Graduate Studies

MASSACHUSETTS INSTITUTE
OF TECHNOLOGY

MAR 19 1996

Eng

LIBRARIES

The Statistical Convergence of Spatial Variations in Aerosol Deposition

by

James C. Moran

Submitted to the Department of Mechanical Engineering on January 15, 1996, in partial fulfillment of the requirements for the degree of Masters of Science in Mechanical Engineering

Abstract

Aerosol deposition occurs in numerous engineering applications, such as coal combustors, pipe erosion and lung deposition. Spatial variations in measured deposition, due to random deposition of particles, can give misleading information. A model has been developed, based on Poisson arrival statistics, which describes the time evolution of the mean number of deposited aerosols and the standard deviation of deposited aerosols. It is related to the particle arrival rate, the sample measuring area and the length of time over which deposition occurs. A novel Laser-Induced Fluorescence (LIF) technique is used to sample liquid aerosol deposition, in a turbulent channel flow, over small areas (0.5mm^2). Numerical simulations of the deposition process were also performed. Both experiments and simulations agreed very well with the analytical model. The LIF output signal is proportional to the mass of particles in the probe area. However, questions still remain over the ability to calibrate LIF system accurately in order to account for such phenomena associated with liquid aerosols such as surface tension effects, curvature effects and agglomeration.

Thesis Supervisor: John H. Lienhard V

Title: Associate Professor

Acknowledgments

First of all I would like to start by thanking my family. If it was not for your encouragement at the beginning I would never have had the courage to take the chance and attend MIT. To Mam and Dad without your constant love and support I would never have made it through MIT. A million thanks. To my younger brothers, Andy and Vinny who have had to put up with me all their lives, many thanks.

To my advisor, Professor John H. Lienhard V, I feel privileged to have had the opportunity of working with you. You always seemed to have had the right answer on the tip of your tongue. It has been fun and a pleasure working with someone who treats all his students very fairly and with respect. Thank you very much for inviting me to work on this project.

To Andy (what are you t-r-y-i-n-g to do) Pfahnl who was a great help to me at the start, middle and end of my work. It has been great fun sharing the office with you, but remember food always tastes nice.

A thanks also goes to Professor Griffith who allowed me use the lab facilities, and for his daily cheer and humor.

To Leslie Regan who was a terrific help to me when I first came to MIT. Thanks for getting me over those first two months.

To everyone in the lab who made it such fun to work in; Marc, Dave, Sheit, Dominic, Tolga, Rudy, Hasham, Mike and Jim.

To Jonny, Mark, Tony and all other soccer players on the graduate team. I hope to see you all at the next World Cup.

Finally to my high school Math teacher, Mr. “Jimmy” Johnston who gave me the confidence to believe in my own abilities.

This work was supported by the MIT Center for Environmental Health Sciences under National Institute of Environmental Health Sciences grant No. P30-ES02109-17.

Table of Contents

Abstract.....	2
Acknowledgments	3
Table of Contents	5
List of Figures.....	7
1 Introduction.....	9
1.1 Project motivation.....	9
1.2 Aerosol Deposition	10
1.3 Mechanics of Aerosol Deposition.....	10
2 Instrumentation.....	12
2.1 Aerosol Deposition	12
2.2 The Laser-Induced Fluorescence (LIF) System.....	12
2.3 The Phase Doppler Particle Analyser	14
2.4 Wind-Tunnel Facility	15
2.5 Aerosol Generation	16
2.6 Unclogging the Array Generator	19
2.7 The Nebulizer Generator.....	20
3 Experimental Apparatus	23
3.1 Turbulent Channel	23
3.2 Additional Modifications	24
3.2.1 Cork Layer	25
3.2.2 Pressure Vessel	25
3.2.3 Variable speed D.C. Motor	27
3.2.4 Data Acquisition	28
4 Statistical Convergence Model.....	30
4.1 Poisson Distribution.....	30
4.2 Model for Statistical Convergence.....	31
4.3 Computer simulations	34
4.3.1 Simulation Results	36
4.3.2 Effects of Polydispersity	41

4.3.3	Effects of Sample Size	42
5	Experiments.....	46
5.1	Experimental Procedure.....	46
5.2	Experiment versus Numerical Results	60
6	Evaporation of Droplets	63
6.1	Evaporation.....	63
6.2	Evaporation inhibitors.....	64
6.3	Suitable Oils.....	66
6.4	Experiments with Oil	69
7	Uncertainties in LIF calibration.....	77
7.1	Particle arrival rates	77
7.2	LIF calibration	85
7.3	Oil experiments.....	87
7.4	Summary.....	91
8	Conclusions.....	94
	Bibliography	96
	Appendix A	99
A.1	Fortran code for numerics.....	99
	Appendix B	105
B.1	Quick Basic code for data acquisition system	105
	Appendix C	108
C.1	Uncertainty tests on sample mean and standard deviation	108

List of Figures

Figure 2.1: The LIF Deposition Measurement System.....	13
Figure 2.2: PDPA Optical System.	15
Figure 2.3: The Aerosol Suction Wind-Tunnel.	16
Figure 2.4: The Array Generator (AG) System.	17
Figure 2.5: Velocity distribution for the Array-Generator.....	18
Figure 2.6: Particle diameter distribution for the Array-Generator.	18
Figure 2.7: Nebulizer Assembly	21
Figure 2.8: Velocity distribution for Nebulizer with water based aerosols.	21
Figure 2.9: Diameter distribution for Nebulizer	22
Figure 3.1: Channel for Turbulent Aerosol Flow.	23
Figure 3.2: Effect of Cork Layer on initial large aerosol droplets.....	25
Figure 3.3: Connections to the Pressure Vessel.....	26
Figure 3.4: Arrangement of AG in settling section.....	27
Figure 3.5: Voltage Divider.	28
Figure 4.1: Histogram of particle arrival rates.....	36
Figure 4.2: Histogram of particle arrival rates.....	37
Figure 4.3: Mean deposition versus time for a parameter of 50.	38
Figure 4.4: Standard deviation versus time for a parameter of 50.....	39
Figure 4.5: Convergence ratio versus time for the simulation.....	40
Figure 4.6: Convergence rates for monodisperse and polydisperse aerosols.	41
Figure 4.7: Mean voltage for a sample size of 9 samples per data point.....	42
Figure 4.8: Standard deviation for a sample size of 9 samples per data point.....	43
Figure 4.9: Convergence ratio for a sample size of 9 data points per sample	43
Figure 4.10: Comparison of monodisperse and polydisperse distributions.....	44
Figure 5.1: Frequency histogram for an experimental run time of 100 seconds.	48
Figure 5.2: Frequency histogram for an experimental run time of 150 seconds.	49
Figure 5.3: Frequency histogram for an experimental run time of 180 seconds.	50
Figure 5.4: Frequency histogram for an experimental run time of 210 seconds.	51
Figure 5.5: Frequency histogram for an experimental run time of 240 seconds.	52

Figure 5.6: Frequency histogram for an experimental run time of 300 seconds.	53
Figure 5.7: Frequency histogram for an experimental run time of 330 seconds.	54
Figure 5.8: Frequency histogram for an experimental run time of 360 seconds.. . . .	55
Figure 5.9: Mean voltage versus time.....	56
Figure 5.10: Standard deviation versus time.....	57
Figure 5.11: Lambda versus time.....	58
Figure 5.12: Standard deviation to mean ratio versus time.	59
Figure 5.13: Convergence ratio versus time	61
Figure 6.1: Evaporation time for several droplets.	65
Figure 6.2: Velocity distribution for nebulizer with oil aerosols.....	70
Figure 6.3: Diameter distribution for nebulizer with oil.....	70
Figure 6.4: Frequency histogram for an experimental run time of 45 seconds.	72
Figure 6.5: Frequency histogram for an experimental run time of 75 seconds.	72
Figure 6.6: Frequency histogram for an experimental run time of 105 seconds.	73
Figure 6.7: Mean voltage versus time.....	73
Figure 6.8: Standard deviation versus time.....	74
Figure 6.9: Standard deviation to mean ratio versus time.	75
Figure 7.1: Calibration technique for LIF.....	79
Figure 7.2: Calibration curves for fluorescein in water	80
Figure 7.3: Emitted light from an aerosol droplet excited by laser source.....	82
Figure 7.4: View factor configuration.	82
Figure 7.5: View factor versus disc radius.....	83
Figure 7.6: Cubed root of voltage versus particle thickness/radius.	85
Figure 7.7: Droplet radius versus volume.....	86
Figure 7.8: Calibration curves for oil glo at a concentration of 0.01% by volume.	88
Figure 7.9: Calibration curves for oil glo at a concentration of 0.02% by volume.	88
Figure 7.10: Frequency histogram for an experimental run time of 120 seconds.	90

Chapter 1

Introduction

This chapter will introduce the motivation behind this particular research. Some background literature in the field of aerosol transport is presented along with some basic equations for the inertial transport of aerosols.

1.1 Project motivation

This project examines the statistical convergence of aerosol deposition. An aerosol is defined as [34] an assembly of liquid or solid particles suspended in a gaseous medium long enough to enable observation or measurement. Generally the sizes of aerosol particles are in the range $0.001 - 100\mu m$. In a turbulent channel flow aerosols are randomly deposited along the channel by the turbulent eddies. This random process results in large variances in measured deposition. The focus of this project is to determine if this variance will converge to an acceptably small limit as time increases. A statistical convergence model is developed. This model can be used to compute the ratio of standard deviation to mean of the measured deposition as a function of time. It is shown that as time increases this ratio will not usually decrease or converge to an acceptably small value. The aerosols used are water based droplets ranging from $20\mu m$ to $60\mu m$ in diameter and the deposition measurements are taken over small areas, ($0.5mm^2$). The lack of uniformity in deposition explains why one measurement by itself is not sufficient to determine characteristic deposition rates in the flow. Rather several measurements must be taken over a given area and a statistical average taken. An experiment is devised to do this.

Another issue dealt with was the problem of aerosol evaporation. Since the aerosols are water based droplets measurements of deposition can be effected by evaporation. Traditional evaporation suppressants such as n-docosanol and the surfactants Span and Tween

were investigated but were found not to be useful for our purposes. The best method of evaporation suppression was to use oil droplets for the experiments. An oil and dye with adequate properties were purchased.

1.2 Aerosol Deposition

Aerosol deposition occurs in numerous applications in both engineering and medical fields. The transport and deposition of harmful particulates in the lung is one such area. Pollutants such as cigarette smoke are inhaled and deposit in the tracheobronchial tract; knowledge of the spatial distribution of deposition is important in assessing the impact to human health.

In engineering applications deposition can also be damaging. When aerosols impinge on a surface they can enhance erosion (Smeltzer et. al. [29]). Tabakoff et. al. [32] discuss how gas turbine engine blades are damaged by small particles and debris. Elsner and Friedman [13], Miller [25] and Bixler [5] all deal with erosion in fluidized bed combustors due to aerosol deposition. Particle deposition is one of the major problems facing the semiconductor industry. Significant loss of product yield results from microcontamination problems during manufacturing, (Cooper, [8]).

1.3 Mechanics of Aerosol Deposition

Particles can be deposited on surfaces by sedimentation, diffusion, inertial impaction, interception, thermophoresis and diffusiophoresis, (Abuzeid et. al. [1]). For a particle size of 20 - 60 μm sedimentation and inertial effects dominate, (Hinds, [20] p.145). In gravitational settling Friedlander [18] gives an expression for the terminal velocity,

$$V_{ts} = \frac{g\rho_p d_p^2}{18\mu} C_s \left(1 - \frac{\rho}{\rho_p}\right) \quad (1.1)$$

Where:

ρ = gas density

ρ_p = particle density

g = gravitational acceleration

μ = gas viscosity (air)

d_p = particle diameter

The coefficient C_s is the Cunningham slip correction which is defined by:

$$C_s = 1 + \frac{\lambda}{d_p} \left(2.514 + 0.8 \exp \left(-0.55 \frac{d_p}{\lambda} \right) \right) \quad (1.2)$$

Here, λ is the mean free path of the gas which for air is $0.066 \mu m$ at $20^\circ C$. As can be seen from eq.(1.1) as the particle diameter increases so too does the gravitational settling rate.

The inertial deposition velocity (V^{\dagger}) in a turbulent flow is given by Friedlander [18],

$$V^{\dagger} = \frac{V}{u^*} \quad (1.3)$$

Where u^* is the turbulent friction velocity,

$$u^* = \sqrt{\frac{\tau_w}{\rho}} \quad (1.4)$$

And V is given by,

$$V = \frac{J}{C} \quad (1.5)$$

Where J is the particle deposition rate and C is the particle bulk concentration above the surface. Abuzeid et. al. [1] showed that in a turbulent channel flow turbulence fluctuations dominate the particle dispersion and deposition processes. This is important because later a model is presented which assumes that the random turbulent fluctuations dominate the deposition process.

Chapter 2

Instrumentation

This chapter describes the measurement technique used to measure aerosol deposition, the array generator used to create the liquid aerosols, the aerosol wind tunnel facility and the Phase Doppler Particle Analyzer (PDPA).

2.1 Aerosol Deposition

In the past several techniques have been developed to quantify aerosol deposition. To determine deposition in lung airways Sweeny et. al. [31] used radioactive counting. There was a large risk associated with this since radioactive materials were involved. Kim [23] used a dye-washing technique but this provides limited spatial resolution since large areas (2.5cm) must be washed. In order to correlate between deposition and flow-pattern much smaller spatial resolution is required. Feng [16] used transmission electron microscopy (TEM) to size and count particles on a surface, but this was expensive and time consuming.

2.2 The Laser-Induced Fluorescence (LIF) System

In light of the disadvantages associated with other deposition measurement techniques, Nowicki [27] developed a laser-induced fluorescence (LIF) system to quantify the mass density of a deposited liquid aerosol. Hoult et. al. [21] also used a similar technique to determine lubricant film thicknesses in automotive engines. The LIF system operates by exciting a small mass of deposited liquid aerosol with a laser. The aerosol contains a known concentration of a fluorescent dye (fluorescein) which absorbs the laser light and then emits light at a different wavelength. The intensity of this light is proportional to the mass of aerosol excited by the laser. In this way real time deposition measurements can be made over a relatively small area (0.5mm²).

Figure 2.1 from Nowicki [27], shows the LIF system. An Argon ion laser emits a beam at 488nm which excites the fluorescein in the liquid aerosol. Fluorescein has a peak absorptance wavelength at 490nm. The laser beam first passes through a bandpass filter at 490nm before entering a fiber optic cable. It exits via a focusing probe which focuses the beam onto a 0.5mm² area on the surface. This causes the fluorescein to fluoresce and emit light at a wavelength of 518nm. This emitted light enters the optical cable via a ring of 12 fibers surrounding the laser beam. Ambient light also enters these fibers and hence two optical interference filters centered at 518nm are used to isolate the fluorescent signal. This signal is focused onto a photomultiplier tube (PMT) which converts the incoming signal into current, and a transimpedance op-amp converts the PMT output current to a voltage. For a more detailed discussion of the LIF system and its electronics the reader is referred to Nowicki [27].

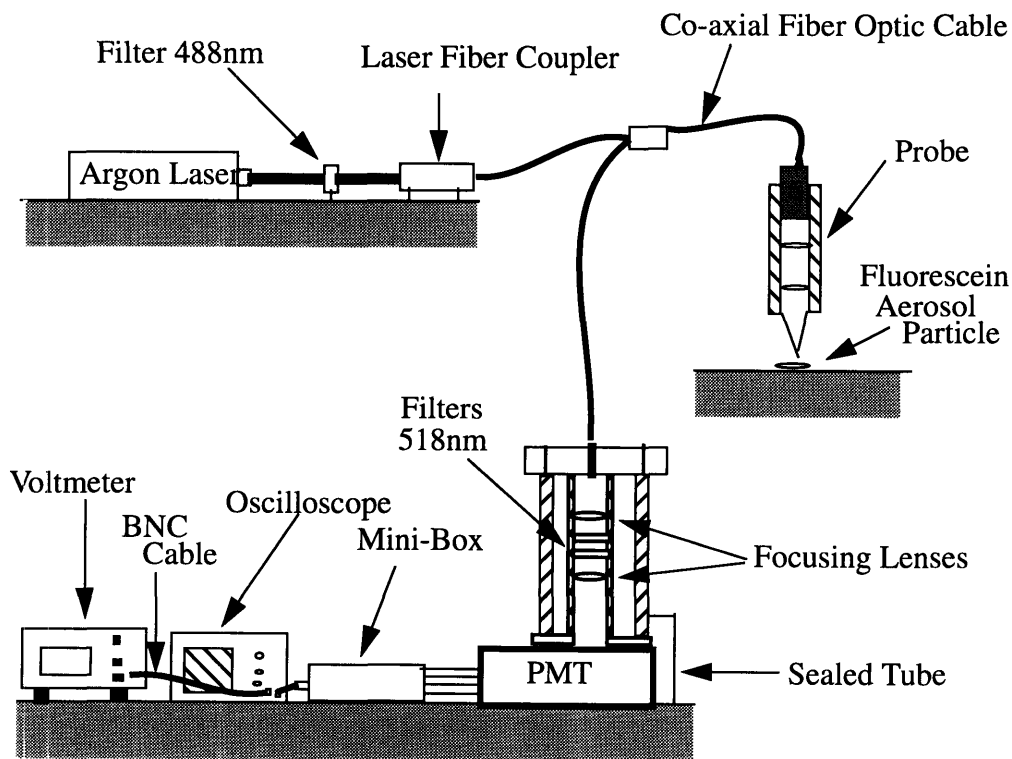


Figure 2.1: The LIF Deposition Measurement System (from Nowicki [27]).

2.3 The Phase Doppler Particle Analyser

The Phase Doppler Particle Analyser (PDPA) is an instrument capable of measuring a single component of particle velocity and particle diameter. It operates by focusing two laser beams each with a diameter of $133\mu\text{m}$ onto a focal point to form a probe volume. This probe volume consists of a set of fringes which are alternating bands of high and low intensity light. When a particle passes through the probe volume it scatters the light. This scattered light is collected by a 495nm receiving lens which focuses the light onto three photomultiplier tubes (PMT). The PMT converts this signal into a current. The gain is governed by the PMT voltage, V_{PMT} , which for our experiments was always set at 350V . The PDPA processor counts the time it takes for a certain number of crossings to occur. Since the fringe spacing is known the velocity may easily be calculated by dividing one by the other.

The particle diameter measurements are more complicated. The operating principle is based on the fact that larger particles will refract more light than smaller particles. By measuring the phase differences among the signals of the three PMTs, particle diameters can be calculated from Mie scattering theory. The variables are the refractive index of the medium (air), the geometry of the PMTs relative to the probe volume, the refractive index of the particles (water) and the particle diameter. The diameter is the only unknown. The PDPA software checks for consistency by comparing the particle diameter measurements between the first and second PMTs with that obtain between the first and third. If the two estimates differ then that measurement is rejected.

The transmitter and receiver of the PDPA is mounted on a Newport laser platform which in turn is mounted on a very sturdy Rambdaudi machining bed. This arrangement provides much needed stability to the sensitive PDPA optical system. The LIF system is

also mounted on this platform. The PDPA probe volume is located 15cm horizontally upstream, and 10cm vertically above the channel.

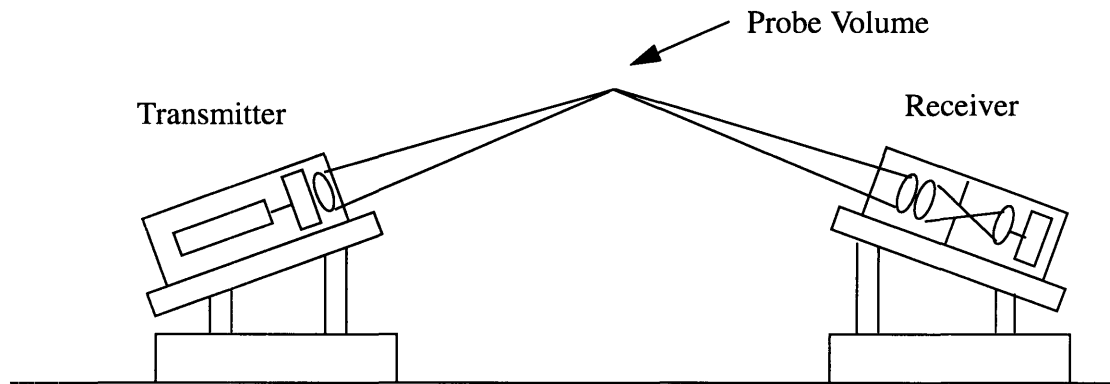


Figure 2.2: PDPA Optical System.

2.4 Wind-Tunnel Facility

The aerosol wind tunnel facility in the Heat and Mass Transfer lab is shown in Fig 2.3. This was designed and fabricated by Child [6], and Colmenares [7], and was later modified by Roth [28]. A 0.75 horsepower blower located at the outlet draws air through the tunnel. Air enters through a straw bundle which helps to create a uniform flow field across the inlet. An aerosol generator seeds the flow with droplets in the settling section. In this section the turbulence created by the generator decays before entering a 20:1 area ratio contraction. A five foot long test section follows where the aerosols can deposit along a flat sintra surface. Roth [28] performed extensive boundary layer thickness measurements in the settling, contraction and test areas of the tunnel to alleviate any flow separation problems. Obstacles may be placed in the test section and flow visualization techniques or deposition in secondary flow structures may be examined in detail (Roth [28]). For our purposes a small channel was built and placed in the test section to provide a turbulent

channel flow for the aerosols to randomly deposit in. This experiment is discussed in greater detail in Chapter 5.

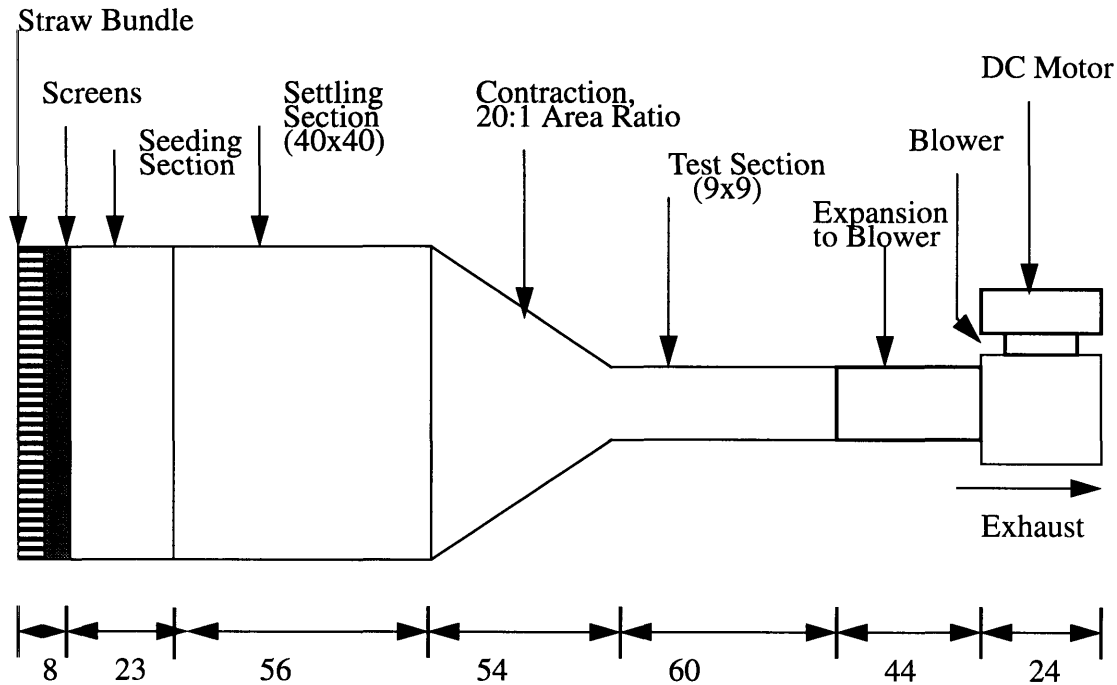


Figure 2.3: The Aerosol Suction Wind-Tunnel (from Roth [28]). Dimensions in inches.

2.5 Aerosol Generation

The aerosol generator used for most of the experiments was a two dimensional high-power acoustic droplet generator, (Array Generator or AG, [17]). It consists of a 225-orifice array (15 by 15 square), each orifice with a diameter of $25\mu\text{m}$. Figure 2.4 is a block diagram of the AG. Compressed air forces liquid from the five-gallon supply tank through a gelman $1.0\mu\text{m}$ nominal filter, a nuclepore $5.0\mu\text{m}$ membrane filter and into the assembly. The assembly consists of piezoelectric transducers which generate pressure variations in the fluid manifold which make velocity perturbations on the liquid jets. If the jet is unstable at the wavelength of the velocity perturbations then it breaks into drops at the fre-

quency of the stimulation signal. The stimulation signal is supplied by a frequency generator and amplified to 50-60V peak-to-peak by a McIntosh power amplifier. The jets are then forced through the orifice and breakup into droplets as a result of the excitation frequency.

About 1cm below the orifice there is a dispersion air nozzle. This is typically operated at 1/4 psi so that air gently disperses the aerosols once they leave the orifice. If this was not done droplets may run into each other and coagulate to form larger droplets. This scenario must be avoided and the dispersion air was very useful in optimizing particle uniformity.

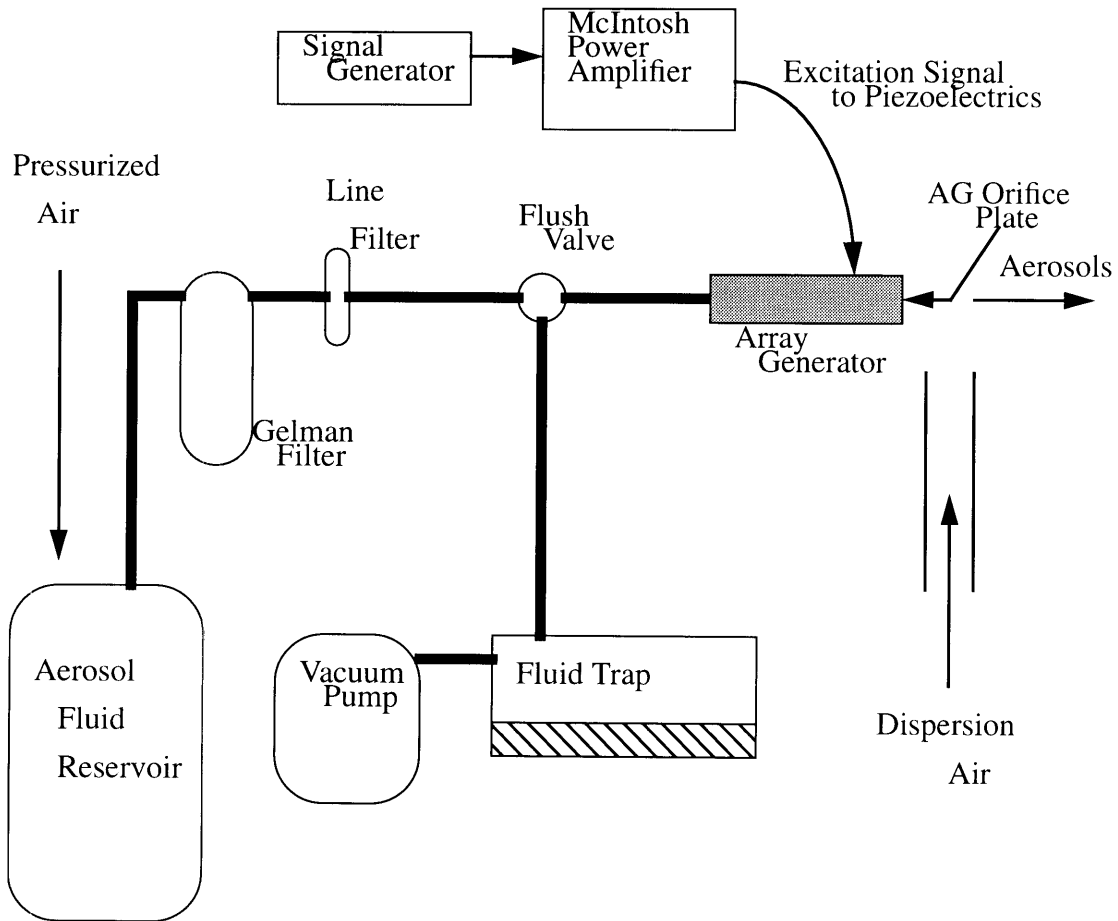


Figure 2.4: The Array Generator (AG) System.

A typical velocity and diameter distribution for the AG is shown below (taken with the PDPA). All PDPA measurements throughout this thesis were taken 15cm in front of the channel inside the test section.

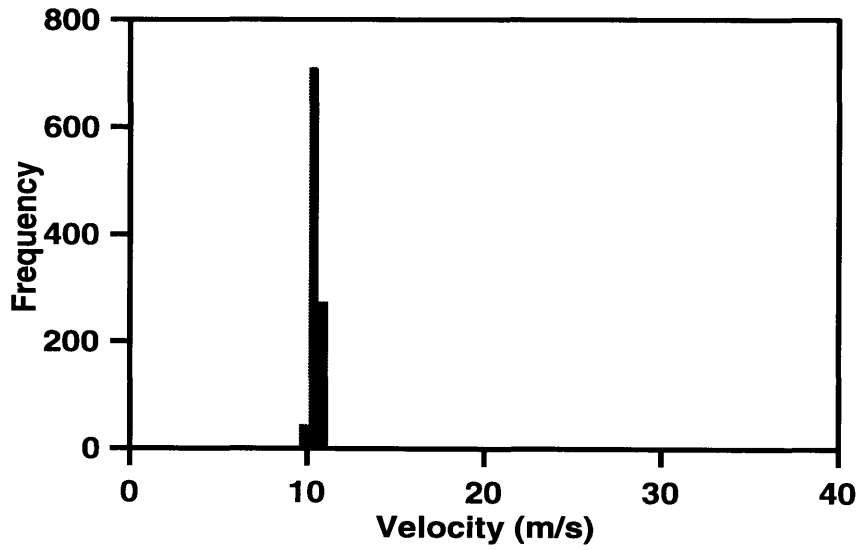


Figure 2.5: Velocity distribution for the Array-Generator

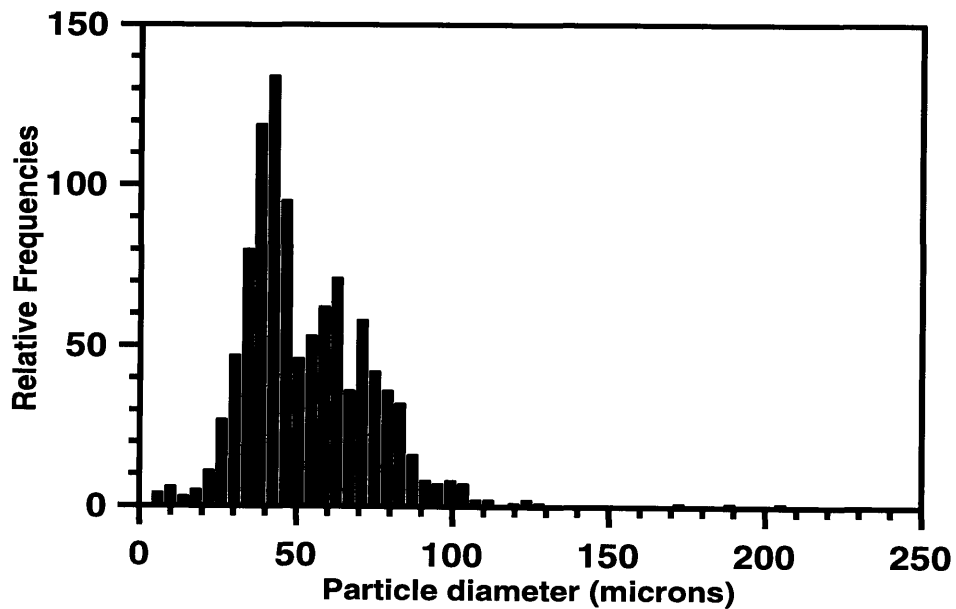


Figure 2.6: Particle diameter distribution for the Array-Generator.

These distributions were taken with a line pressure in the 5-gallon tank of 20psi, excitation frequency of 80kHz, wind-tunnel blower set at 50% of its rated value and a PMT voltage of 350V. All experiments and measurements in future chapters were performed with these specific parameters unless otherwise stated. The above diameter and velocity distributions are typical for the AG with these parameters. From the figures above the mean velocity was 10m/s and the mean particle volumetric diameter was $58\mu\text{m}$. Throughout this thesis the mean diameter of the particles is taken to be the volumetric mean diameter.

2.6 Unclogging the Array Generator

From Figure 2.6 the aerosol distribution is not monodisperse. This is a problem because it is not possible to tell if a given signal from the LIF resulted from several small particles or one large particle. The orifice plate must be kept clear at all times in order to prevent the distribution from becoming even more polydisperse. Small dirt particles can be troublesome with regard to clogging the $25\mu\text{m}$ holes in the array. The AG is fairly robust and several cleaning techniques are available.

Gently wiping the orifice with a soft tissue may sometimes cause embedded dirt particles to be dislodged. A more effective technique is to blow air from a compressed air can through the orifice. This is quite effective but if the orifice is badly clogged then more drastic measures are needed. The orifice may be placed in clean filtered aerosol fluid and the flush valve opened to allow the vacuum pump draw filtered fluid through the manifold and into the liquid trap. The piezoelectric actuators should be excited at their natural frequencies ($\sim 10\text{kHz}$) as this helps dislodge embedded particles.

Finally as a last resort the nozzle head may be disassembled and placed in a jar of alcohol or lacquer thinner and placed in an ultrasonic bath for 10-15 minutes. This method

should only be used as a last resort as small debris gets generated in the screw threads when reassembly takes place which may cause further clogging. In one unusual case, an algae growth developed in the gelman filter which continually clogged the membrane filter and the AG. A 10% Ammonia solution was used to purge out the entire system after which clogging became a minor problem.

2.7 The Nebulizer Generator

The AG is useful for producing reasonably monodisperse, high number density jets but its main disadvantage is the ease with which it gets clogged. This meant that only very pure (millipore) water could be used to generate aerosols. Any other liquid or even tap water would undoubtedly block the orifice. Since oil was a liquid being considered for aerosolization, owing to its low vapor pressure, another generator clearly had to be used. An expensive filtration system could have been hooked up to the AG but this was rejected because the higher oil viscosity would have resulted in a larger velocity gradient in the AG manifold which would cause each jet to have a different velocity which would lead to irregular jet breakup and a polydisperse spray.

In light of these developments a compressed air nebulizer (Figure 2.7) was used. It consists of two copper tubes each 1/4 inch in diameter mounted on an aluminium shaft. Yoon [35] provides a detailed account of nebulizer operation. Basically the copper tube with the 90° bend is connected with tubing to a beaker of fluorescein and water. The air is connected to the straight copper tube. The house air is then pumped through the straight tube at 30psi. This creates a low pressure area over the second copper tube which draws liquid up through the tubing. As the water layer approaches the near wall of the copper tube, it encounters the high velocity airstream, breaks up into fine droplets and is carried into the airflow. Since the tube diameters are so much larger (1/4 inch) than the AG orifice holes (25 μ m) clogging is not a problem and oil can just as easily be used as water.

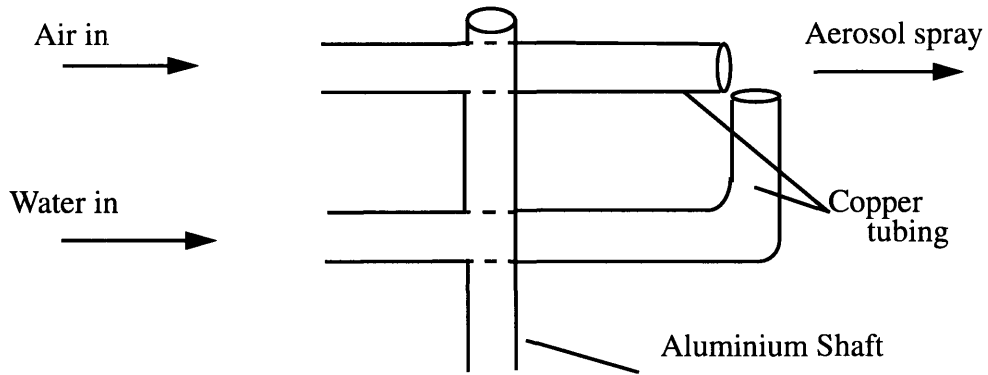


Figure 2.7: Nebulizer Assembly (from Yoon [35]).

Typical velocity and diameter distributions for water are as follows:

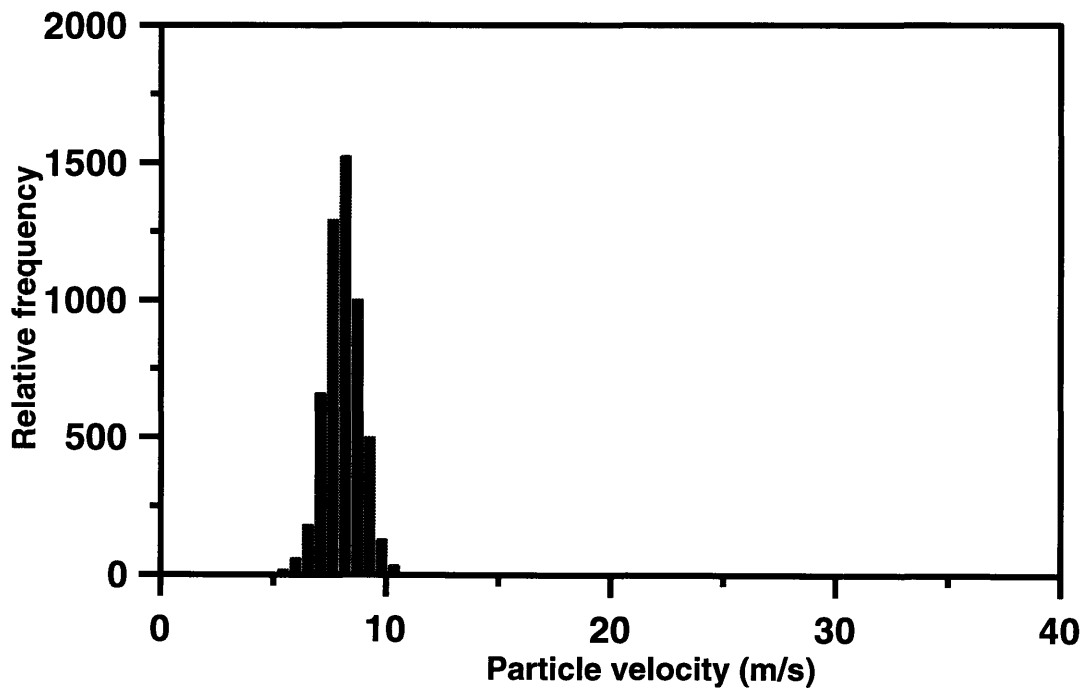


Figure 2.8: Velocity distribution for Nebulizer with water based aerosols.

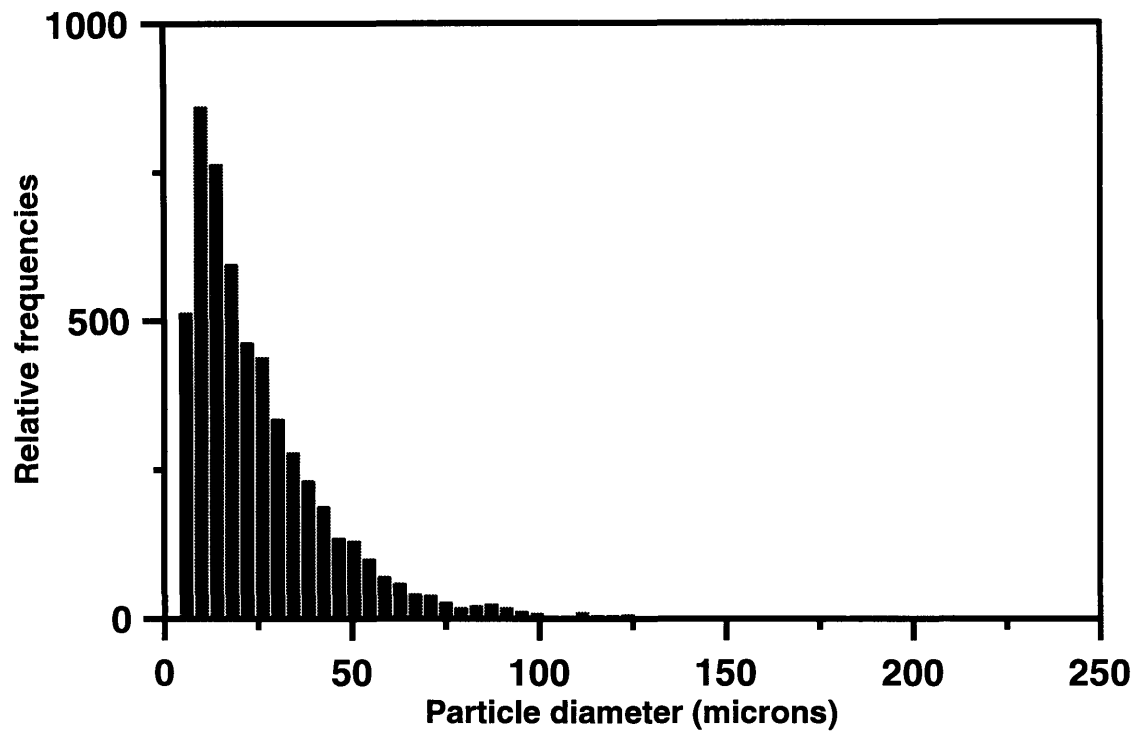


Figure 2.9: Diameter distribution for Nebulizer

As can be seen the distributions are far more polydisperse than that of the AG. The mean velocity was 8m/s and mean volumetric diameter was 41.2 μ m.

Chapter 3

Experimental Apparatus

This chapter introduces the experimental procedure used for the deposition experiments. Each aerosol must have an equal probability of deposition at any particular point in the measurement area. Concentration gradients in the axial or lateral directions are to be avoided. The reason why this is necessary shall be explained in chapter 4. In order to accommodate this requirement modifications to the existing experimental apparatus were necessary. These are discussed in this chapter.

3.1 Turbulent Channel

A channel was built and placed in the test section of the aerosol wind tunnel (Fig 2.3). A Reynolds number based on hydraulic diameter, Re_h , of 10^4 in the channel was considered an appropriately high value for ensuring a well developed turbulent channel flow. The following channel was designed:

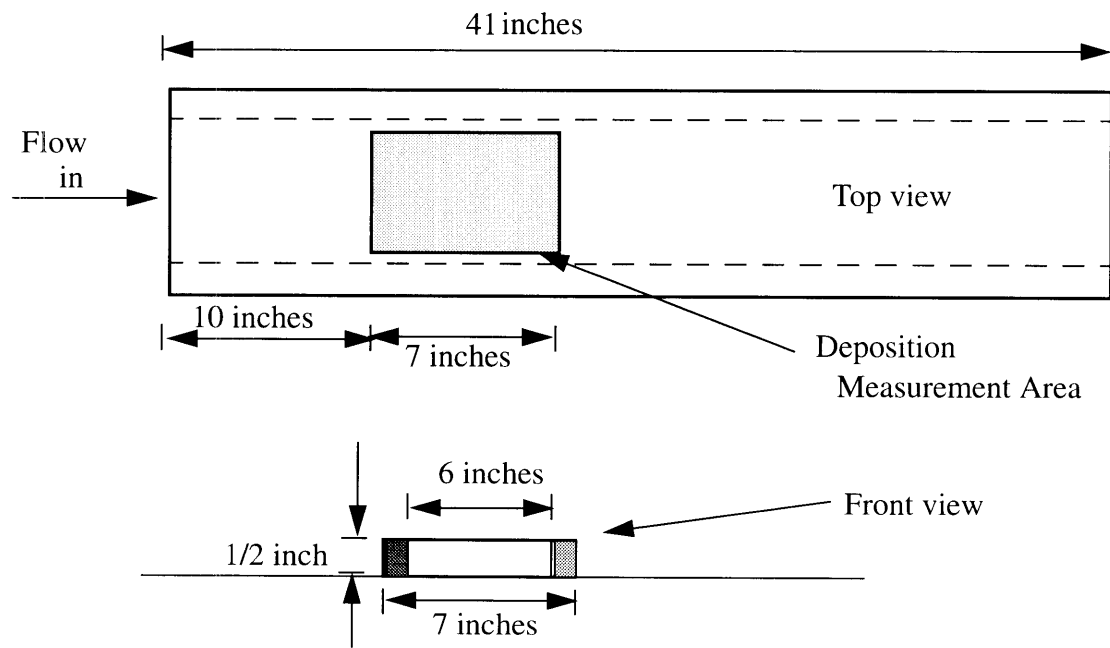


Figure 3.1: Channel for Turbulent Aerosol Flow.

The hydraulic diameter, d_h , is defined as being four times the cross-sectional area divided by the wetted perimeter.

$$d_h = \frac{4 \cdot \text{height} \cdot \text{width}}{2(\text{height} + \text{width})} = 0.0234m$$

For a bulk velocity of say 10(m/s) and an air kinematic viscosity, ν , of $14.77 \times 10^{-6} (m^2/s)$ for a temperature of 290K, the Reynolds number, based on hydraulic diameter, of the flow is then:

$$Re_h = \frac{U \cdot d_h}{\nu} \quad (3.1)$$

Using the value for d_h gives a Reynolds number of, $Re_h = 15,800$.

To ensure that aerosols have an equal probability of depositing along the channel the flow must be fully developed. Generally a flow becomes fully developed after 5 hydraulic diameters. That would mean a fully developed flow 4.62 inches into the channel. To leave a margin of safety data is not taken until after 10 inches.

Deposition measurements are taken with the LIF laser probe (see fig.2.1) across a grid of 280 points in the shaded area of the channel in fig 3.1. The signal from the LIF is then recorded every half an inch for seven inches down the length of the measurement area. The probe is then moved a quarter of an inch across the channel width and the procedure repeated. This continues until the probe has moved five inches across the channel width. The channel width is six inches therefore the probe starts and finishes half an inch inside the channel walls. An advantage of this is that boundary layers at the walls will not affect the measured deposition substantially. Therefore a total number of (14x20) 280 deposition measurements are taken for each experiment.

3.2 Additional Modifications

In order to successfully deposit aerosols at random, a number of small but important

modifications had to be carried out on existing facilities. This section describes what those modifications were.

3.2.1 Cork Layer

Originally when the aerosols came into contact with the channel they tended to form large droplets around the sharp leading edge of the channel. This was a problem since these large droplets tended to flow down the channel destroying the deposited particles after only a few minutes. They also tended to block a large section of the inlet and so helped prevent uniform deposition. Paper towels were secured to the sintra surface in an effort to absorb these droplets but they tended to rise up from the surface and block the channel. In the end a layer of cork was placed in front of the channel so that large droplets would form along its leading edge. When these droplets started to run they were absorbed by the cork and eventually ended up passing harmlessly underneath the cork as shown in fig.(3.2).

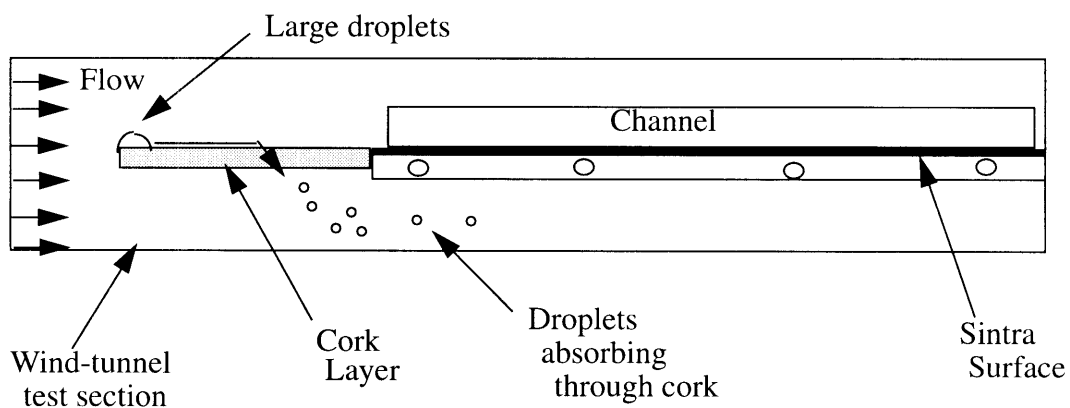


Figure 3.2: Effect of Cork Layer on initial large aerosol droplets.

3.2.2 Pressure Vessel

In figure 2.4 the dispersion air which helps to separate the aerosols immediately after they leave the array generator is connected via a pressure regulator to the house air supply.

The house air is at a pressure of 125psi but this varies over time. This variation causes a variation in the dispersion air pressure which is supposed to be constant at 0.25psi. Too little dispersion air means particles may agglomerate to form larger droplets. Too much dispersion air means the aerosols are propelled further upwards. As they descend they are swept by the air stream into the channel. This greatly increases the number density in the channel and severely effects the statistical convergence. It is vitally important to keep the number density constant during experiments since this is directly proportional to the convergence of the data. In this regard it is not too important if the dispersion air pressure is set anywhere between 0.15 - 0.45psi so long as it stays at that pressure throughout the duration of the experiment.

To keep the air pressure constant a six foot, 140psi pressure vessel was hooked up to the house air (fig.3.3). A regulator keeps the pressure in the tank at 35psi. The tank is then connected to the dispersion air line and to the aerosol fluid reservoir. This damped out the variances in the house air line. Fig 2.4 shows the remainder of the connections to the AG system.

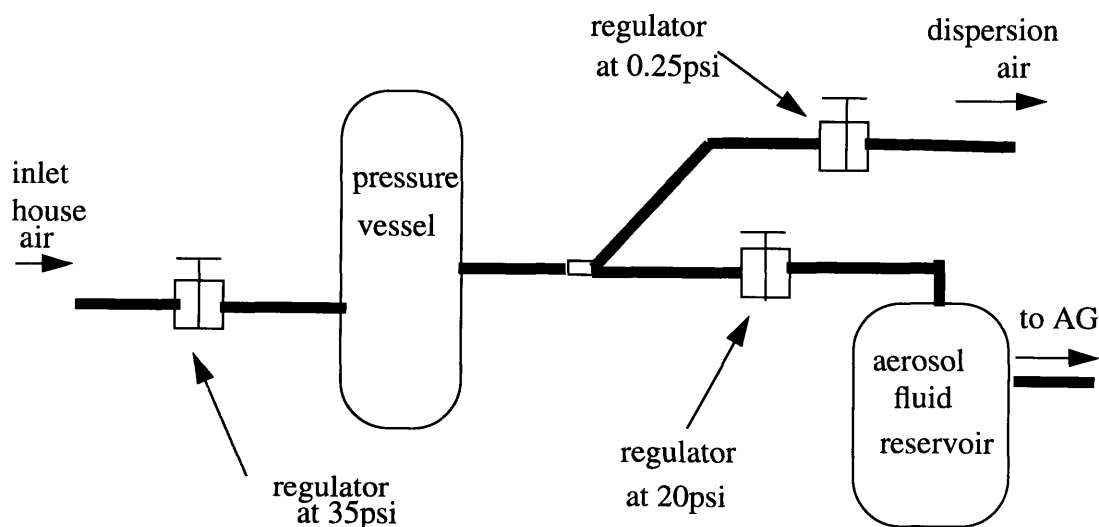


Figure 3.3: Connections to the Pressure Vessel.

3.2.3 Variable speed D.C. Motor

The settling section of the wind tunnel is 40 inches wide and leads to the 9 inch test section via a contraction. The array generator was mounted on a retort stand in the middle of the settling section. The problem was that this tended to give a larger number density down the centre of the test section and less at the sides. This led to an increased probability that deposition occurred down the centre more so than the sides. It was necessary that each aerosol have an equal probability of depositing anywhere along the channel so the array generator was mounted on a lead screw. The lead screw was powered by a variable speed, 0.02 Hp, DC electric motor from the Bodine Electric Company. It was also located in the settling section. It moved the AG out 8 inches on either side of the centre of the settling section at a speed of 20 inches per minute. When it reached one end of the lead screw a switch was turned which reversed the direction of the current. This caused the AG to travel back to the other end. The net effect of this is to cause the aerosols to disperse more uniformly across the channel.

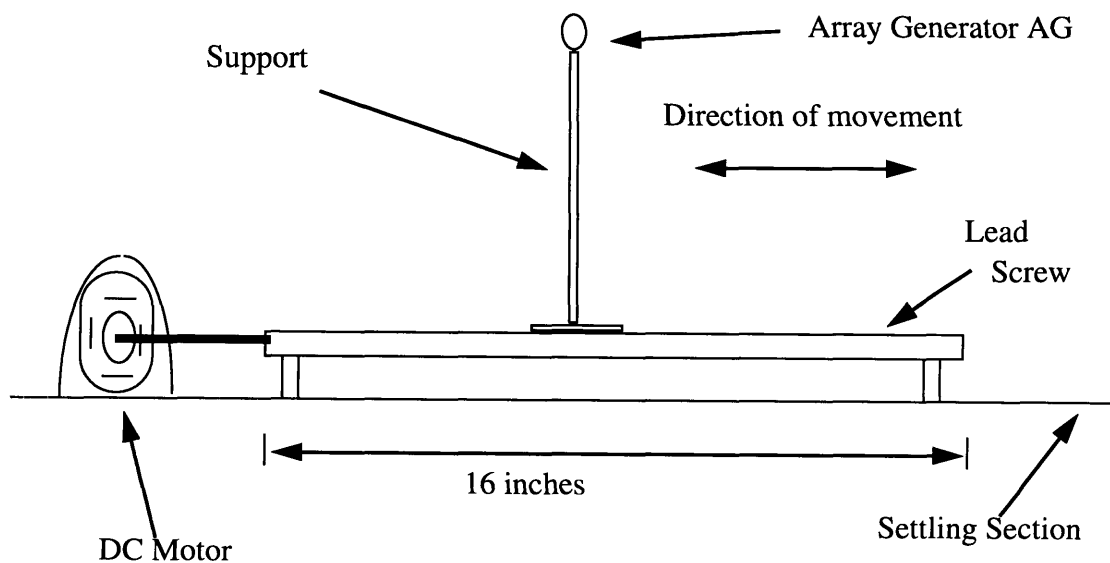


Figure 3.4: Arrangement of AG in settling section.

3.2.4 Data Acquisition

After each experiment data was taken across the length and breadth of the measurement area in the channel. A total of 280 specified points were taken. The probe was placed over a point, the reading was taken by hand from a voltmeter. This procedure was time consuming which meant that the droplets on the surface had time to evaporate before the measurement was taken. There is not a minimum time by which the readings must be recorded since evaporation starts instantaneously but the shorter the time required for the data to be taken the better.

It was decided to connect a data acquisition board to the LIF system. The probe would have to be manually moved but then the board would read the voltage signal directly into a file. This would save time in recording the data and also time would be saved in analyzing the data because it would already be saved onto a computer file. This would mean the data could automatically be loaded into software packages instead of having to manually type the file into the system.

A Das-8 data acquisition board was used for the task along with an IBM 386. Nearly all voltages from the LIF are between 0 and 15 volts. However the Das-8 can only read voltages between 0 and 5 volts. A voltage divider (fig.3.5) was used which divided the signal from the LIF by three. The new signal was fed into the board and the software multiplied the answer by three before printing the voltage to a file and the screen.

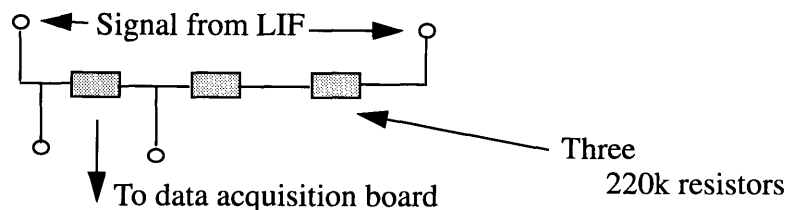


Figure 3.5: Voltage Divider.

The data acquisition board contains eight analog input channels. Its A/D converter has a conversion time of $25\mu s$ resulting in data throughput rates of 30kHz. A standard 37-pin male connector is connected to it at the back of the computer. The signal from the potential divider and the ground are connected to two of the pins. The software program for the DAS-8 acquisition board is presented in Appendix B.

Chapter 4

Statistical Convergence Model

This chapter develops the statistical convergence model for aerosol deposition. The model is based on Poisson arrival statistics. The advantage of using a statistical approach to the problem is that the complicated equations of motion and the actual mechanics of transport are avoided. The focus of interest is just on statistically analyzing the distribution of particles after they have deposited. Computer simulations of the random deposition process are also presented.

4.1 Poisson Distribution

It is a very complicated task to model the deposition of aerosols using the Lagrangian equation of motion. This has been tried before but results have been complicated and difficult to verify experimentally. A new approach is taken to the problem which just deals with the statistical distribution of deposited aerosols and avoids dealing with the actual physical process or mechanism of deposition. Therefore the equation of motion does not enter into the model.

There are three probability distributions of great universality which occur in a great variety of problems. These are, with ramifications throughout probability theory, the binomial distribution, the normal distribution and the Poisson distribution. The Poisson distribution:

$$p(k;\lambda) = e^{-\lambda} \frac{\lambda^k}{k!} \quad (4.1)$$

represents the probability of finding exactly k points or events within a fixed interval of specified length, if the mean number of events in that interval is λ . This distribution has been used to model a wide variety of everyday observations. Tyagi et al [33] uses it to

model defect spatial distribution in wafer scale integration (WSI). Nielsen et al [26] explore the implications of non-Poisson behavior in hemacytometer cell count distributions. Feller [15] uses it to determine the probability of a certain number of α -particles from a radioactive substance reaching a given portion of space during a time t . He also uses it to model chromosome interchanges in cells and telephone connections to a wrong number. However it was his modelling of flying bomb hits on London during World War II that attracted our interest. He found the spatial distribution of dropped bombs on London fitted the Poisson distribution with 90% accuracy. The spatial distribution of bombs dropping on a city is rather similar to the distribution of aerosols depositing on a plate.

There are three assumptions which must be made in order for a Poisson distribution to be valid. The first is that the conditions of the experiment must remain constant in time so therefore the probability of a particle arriving at a particular location does not vary in time. The second is that non-overlapping time intervals are stochastically independent in the sense that information concerning the number of events in one interval reveals nothing about the other. The third is that the probability of two or more occurrences in a very short interval is approximately zero. The deposition of inertia aerosols in a turbulent channel flow meets these three criteria. Particles are entrained in the random turbulent eddies and are deposited randomly along the channel. So long as the number density of aerosols in the channel remains essentially constant over the measurement region, i.e. the conditions of the experiment remain unchanged, it may be assumed that the Poisson model applies to the spatial distribution of particles within that region.

4.2 Model for Statistical Convergence

In a turbulent channel flow the probability of x particles arriving at a specific location in space during a time interval τ is modelled using the Poisson distribution:

$$p(x, \lambda\tau A) = \frac{(\lambda\tau A)^x \cdot e^{-\lambda\tau A}}{x!}, \text{ For } x = 0, 1, 2, 3, \dots \quad (4.2)$$

Here λ is the average number of particles deposited per unit area during a time interval τ , A is the probe area, and x is the actual number deposited in the area A during time τ . The mean of this distribution is

$$\mu_x = \lambda\tau A$$

and the variance is

$$\sigma_x^2 = \lambda\tau A \quad (4.3)$$

Suppose that N is the total number of particles measured after a time T in an area A . Then

$$N = A \cdot \int_0^T n'' dt \quad (4.4)$$

where n'' is the actual number of particles depositing per unit area per unit time.

On the other hand, the expected number of particles deposited, μ_n , is simply

$$\mu_n = A\lambda T \quad (4.5)$$

In order to find the standard deviation of the number of particles deposited, σ_n , it is necessary to find the standard deviation of the integral (eq. (4.4)). If the integral is treated like a sum of deposition events x_i over many small time intervals τ , then

$$A \cdot \int_0^T n'' dt \cong \sum_{i=1}^m x_i \quad (4.6)$$

for $m=T/\tau$. The value of m should be large for this approximation to apply.

Equation(4.6) implies that $Var\left[A \cdot \int_0^T n'' dt\right] \cong Var\left[\sum_{i=1}^m x_i\right]$.

But
$$Var\left[\sum_{i=1}^m x_i\right] = E\left[\left(\sum_{i=1}^m x_i - E\left[\sum_{i=1}^m x_i\right]\right)^2\right] \quad (4.7)$$

from the definition of variance, where $E[]$ represents the expectation value of a random variable. Since $E[x_i] = \mu_x$

$$E\left[\left(\sum_{i=1}^m x_i - E\left[\sum_{i=1}^m x_i\right]\right)^2\right] = E\left[\sum_{i=1}^m (x_i - \mu_x)\right]^2 = \sum_{i=1}^m E[(x_i - \mu_x)^2] = \sum_{i=1}^m \sigma_x^2 \quad (4.8)$$

where the variance of x is defined by:

$$\sigma_x^2 \equiv E[(x_i - \mu_x)^2]$$

If we denote the variance of the integral as σ_n^2 , then:

$$\sigma_n^2 \equiv Var\left[A \cdot \int_0^T n'' dt\right] = (m \cdot \sigma_x^2) \quad (4.9)$$

Hence,
$$\sigma_n = \sqrt{m} \cdot \sigma_x = \sqrt{\frac{T}{\tau}} \cdot \sigma_x \quad (4.10)$$

Equation (4.10) shows that the standard deviation of deposition measurements increases as the square root of time. On the other hand, the mean number of particles deposited increases linearly with time, so that the *relative* magnitude of the spatial variations of the data will decrease in time. To examine the temporal convergence of the measurements, we form the ratio of σ_n and μ_n using equations (4.5) and (4.10):

$$\frac{\sigma_n}{\mu_n} = \frac{\sigma_x}{A\lambda T} \sqrt{\frac{T}{\tau}} \quad (4.11)$$

Substitution of eq.(4.3) gives the final result:

$$\frac{\sigma_n}{\mu_n} = \frac{1}{\sqrt{\lambda TA}} \quad (4.12)$$

The standard deviation to mean ratio depends on three experimental parameters: λ the mean rate of particle deposition; A , the sample area ($0.5mm^2$) for our laser probe; and T the length of the experiment. One expects on physical grounds that the longer the experimental run time the smaller this ratio will be. It would also seem a valid assumption to

expect the ratio to be lower with a higher number density of particles depositing per unit time, λ , in the channel. The model validates both of these assumptions. It is necessary to choose a value as an arbitrary reference to indicate when the data has sufficiently converged. A value of 0.1 was chosen. Therefore if $\{\frac{\sigma_n}{\mu_n}\} \leq 0.1$ the data will be said to have converged.

4.3 Computer simulations

Computer simulations were carried out for several reasons. We were interested in understanding how random particle deposition behaves and in obtaining initial estimates for the accuracy of the convergence model presented. Also the effects of aerosol polydispersity could be analysed in more detail by comparing simulated results for monodisperse and polydisperse distributions. Finally different sample sizes used to determine the experimentally measured mean, \bar{n} and standard deviation, s_n can be studied and checked to see if they are good estimates for the true mean and standard deviation.

The simulation was based on our actual experimental setup. The test area where deposition is measured is a square area 16.5cm by 12.7cm (See figure 3.1). The laser spot size is 0.8mm in diameter when focused correctly on to the sintra surface. A matrix is generated in the code which has, $165/0.8 \approx 207$ rows and, $127/0.8 \approx 159$ columns. The assumption in this model is that the power of the laser is uniform in its own plane which is not completely true in practice but is accurate for the purposes of this model.

With the matrix set up the code then randomly 'deposits' random points onto the matrix by a fixed specified amount each second. For example, one may specify it to deposit 50 particles per second for 1000 seconds. It will generate 50 pairs of random numbers, one set between the range of 1 - 207 and another between the range of 1 - 159. Each random pair specifies a coordinate on the matrix. That coordinate now contains one parti-

cle so the value corresponding to that coordinate is incremented by one. The whole process would then repeat itself 1000 times and the value associated with each coordinate would be stored in the computers memory.

The next step is to calculate the sample mean number of particles, \bar{n} , and sample standard deviation, s_n , within the test matrix. Experimentally 280 data points were collected and the mean and standard deviation calculated. For the purposes of the simulation a total of 210 points on the matrix were sampled. These points were not randomly sampled; they were taken in fixed regular pattern every time. The number of particles in each of these points was used to compute the mean number of particles and the standard deviation. The procedure was then repeated for different run times and the results plotted.

A problem with the above numerical method is that it assumes that all particles are the exact same size. In the experiments the particles generated contain different size diameters as shown in figure (2.6). If the particles were distributed according to this distribution our model would be more representative of the test conditions. Therefore this measured distribution is read into the code at the start. It is scaled according to the number of particles the user wishes to deposit per second. The mean value in each matrix point is then calculated from the number of particles times each of their respective diameters times a constant. This method was considered the most accurate for simulating the experimental LIF measurements since the LIF output is dependent upon the relative sizes of aerosols within its probe area. The standard deviation is calculated in a similar way. In this way the effect of polydispersity was analysed. The size distribution may vary when different experimental conditions are used. Therefore, two other distributions were read into the code and the statistical results were compared to those of a uniform size aerosol and to the distribution of Fig.(2.6). The code for this simulation can be found in appendix A.

4.3.1 Simulation Results

The first necessary objective was to test the arrival rate of the particles in the matrix. A key assumption in our model is that the particle arrival rate was Poisson distributed. This essentially was a reflection on the accuracy of the random number generator. If it was a poor generator that repeated the numbers generated periodically, the simulation would not be valid. In order to test this the following procedure was carried out. The particle arrival rate was kept at 50/second and the simulation run time was ten thousand seconds. Each time a particular run was completed the number of particles in row 100 of the matrix was counted. The procedure was repeated 10,000 times and a bar graph was plotted of the number of particles counted versus their relative frequency.

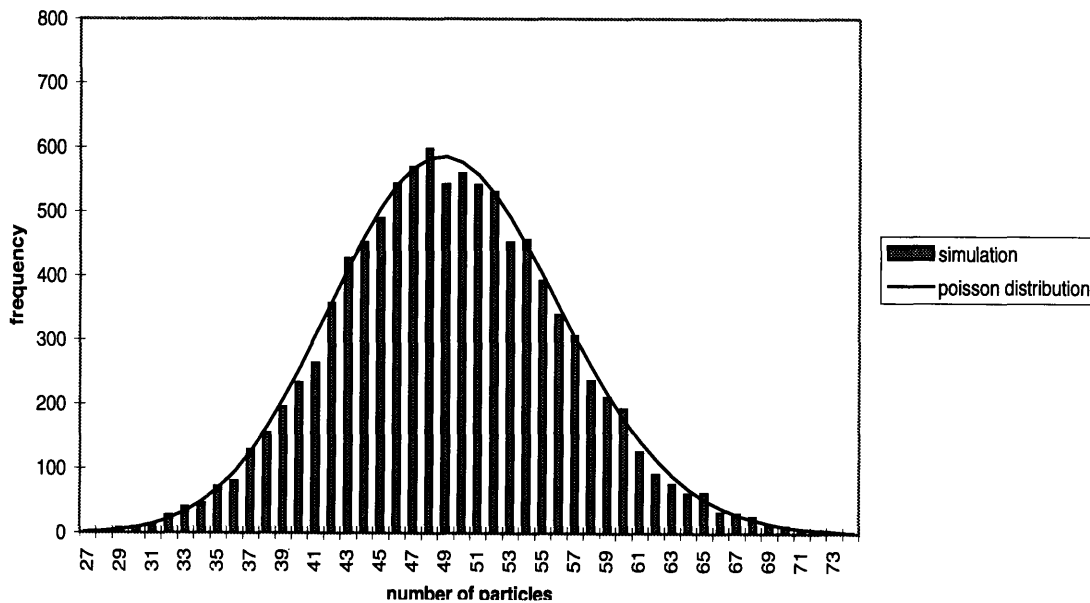


Figure 4.1: Histogram of particle arrival rates.

A Poisson distribution was superimposed over the bar graph. The parameter of the poisson distribution is 50. This graph shows the particle arrival is Poisson. However for large numbers on the x-axis (typically greater than 30) the Poisson distribution is approxi-

mately normal. Therefore the procedure was repeated except this time the number of particles deposited per second was limited to 6. This would give a lower number on the x-axis so the Poisson distribution could be distinguished from the normal distribution.

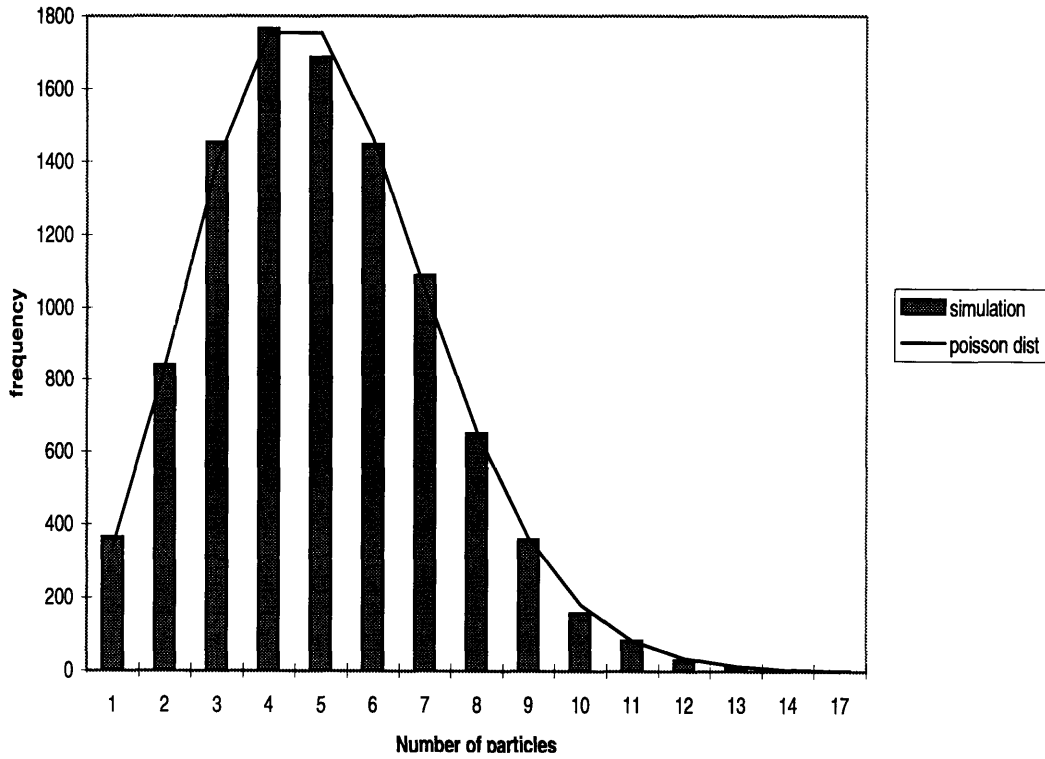


Figure 4.2: Histogram of particle arrival rates.

The above graph is certainly Poisson as opposed to normal. Therefore it is possible to conclude that the particle arrival in the simulation is poisson.

The next step is to calculate the evolution of the sample mean \bar{n} , the sample standard deviation s_n , and the ratio of the two, $\frac{s_n}{\bar{n}}$. The code in appendix A was used for this purpose. It started off by calculating the mean and standard deviation for a simulation run time of 100 seconds and then incrementing the next simulation by 100 seconds for the next run. This was repeated until the simulation run time was 10,000 seconds. The mean number of particles deposited per second was specified to be 50. From here on a parameter

of 50 means that 50 particles per second were deposited into the test matrix. Finally the diameter distribution used was the same as shown in figure (2.6). The results are shown below.

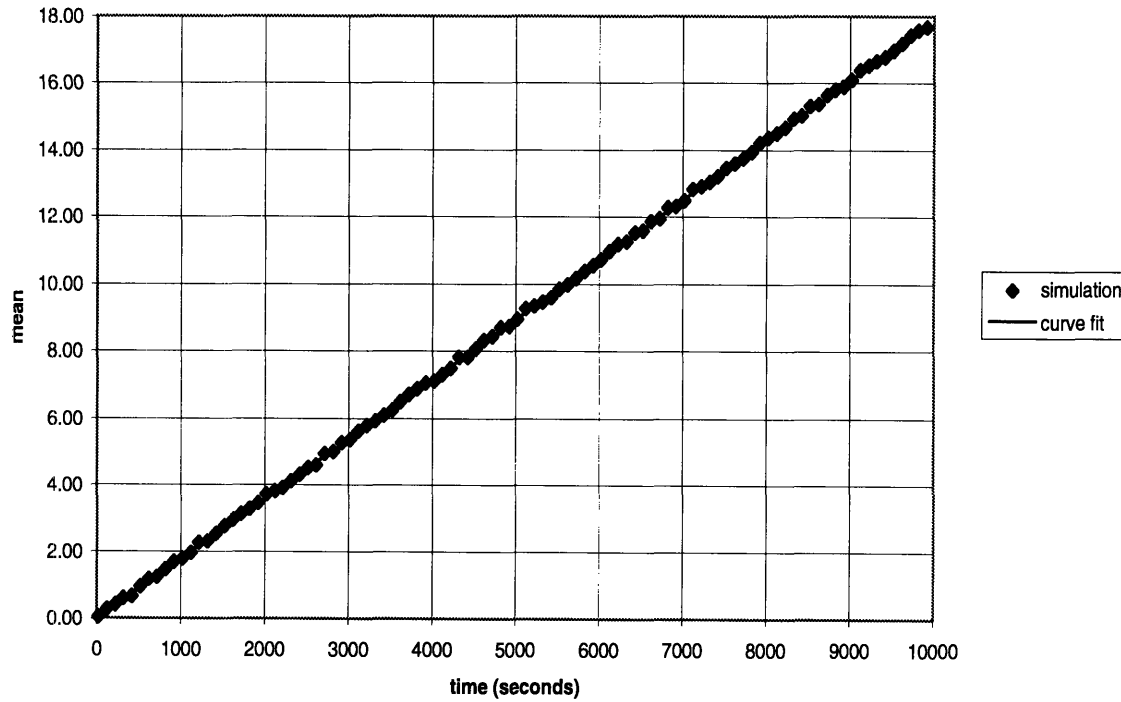


Figure 4.3: Mean deposition versus time for a parameter of 50.

The curve fit (which is difficult to see due to the straightness of the data points) has the equation, $\bar{n} = 0.001787T$. This shows the mean is directly proportional to time in our simulation. If eq.(4.12) is to hold this would require the standard deviation to be proportional to the square root of time. The standard deviation is as follows:

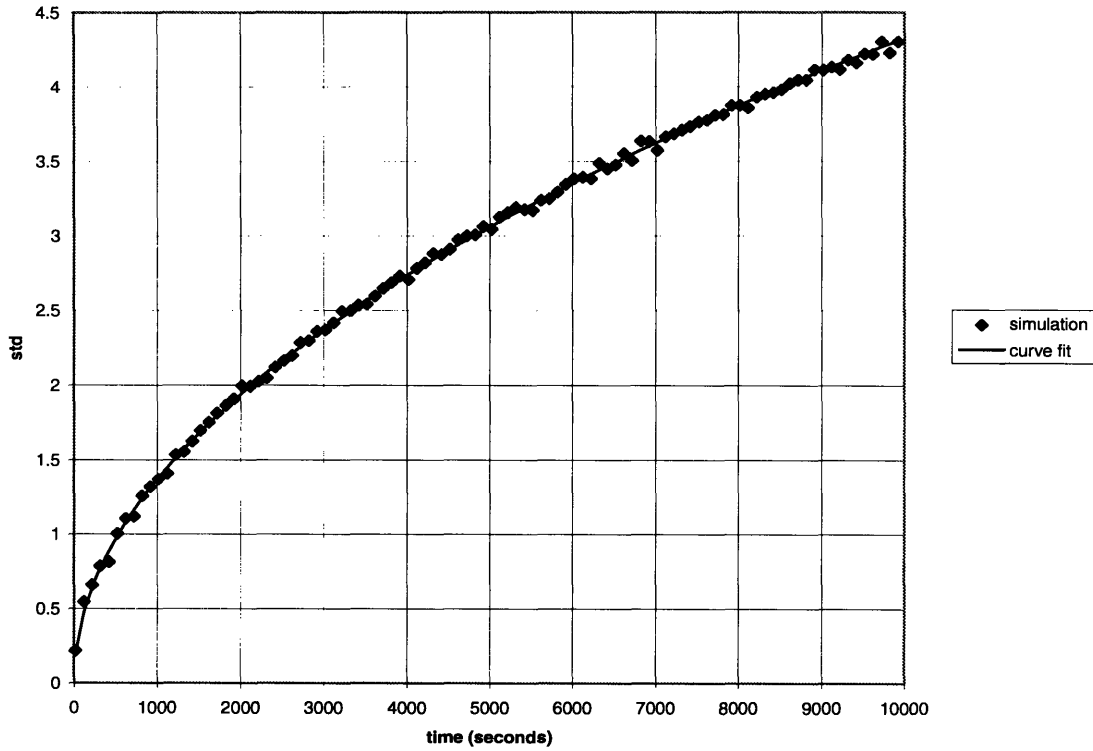


Figure 4.4: Standard deviation versus time for a parameter of 50.

The equation for the curve fit is, $s_n = 0.04328 \cdot \sqrt{T}$. From the accuracy of the curve fit it is fairly certain that the standard deviation is proportional to the square root of time in this simulation.

Now the ratio of the two are plotted. This time instead of fitting a curve eq.(4.12) is used to predict the shape. In our model the parameters λA , signify the number of particles arriving per unit time. In the simulation model this parameter is represented by the number of particles arriving at each matrix point. The number of matrix points is $159 \cdot 207 = 32913$ points. The particle arrival rate at each of these points is then $50/32913$ particles/second. Therefore our theoretical model becomes:

$$\frac{\sigma}{\mu} = \frac{1}{\sqrt{\frac{50}{32913} \cdot T}} \quad (4.13)$$

If this equation is plotted along with the numerical results for $\frac{\sigma}{\mu}$ the following graph is obtained.

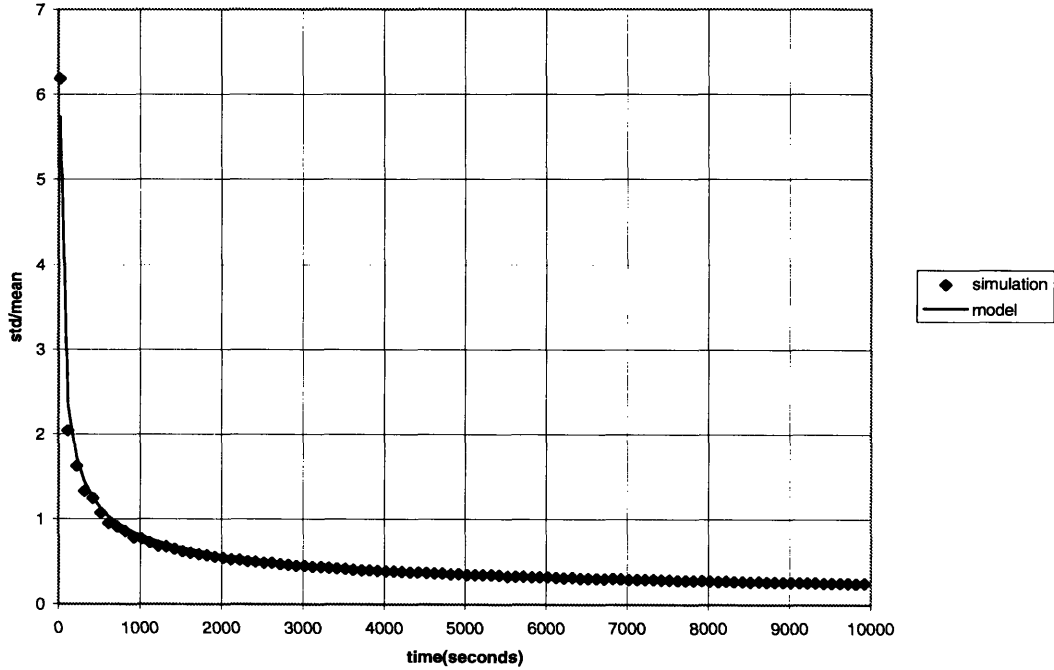


Figure 4.5: Convergence ratio versus time for the simulation, $\frac{s_n}{n}$ and the model, $\frac{\sigma_n}{\mu_n}$.

The model agrees very well with the numerical results. If the criteria for convergence is now applied to the above simulation which was stated earlier on as being:

$$\left\{ \frac{\sigma}{\mu} \right\} \leq 0.1$$

This can be written using the theoretical equation as:

$$\frac{1}{\sqrt{\frac{50}{32913} \cdot T}} \leq 0.1$$

This condition gives a value for T greater than or equal to 16 hours. Depositing 50 particles/second for 16 hours represents an arduous experiment. The numerical results seem to suggest that convergence to an acceptably small limit will only occur after very

long run times or else very high particle deposition rates. To back up this statement it is necessary to obtain experimental data which will be done in the next chapter.

4.3.2 Effects of Polydispersity

The effects of polydispersity on the aerosol distribution are examined in this section. Most aerosol distributions in practice are polydisperse and so it is important to understand if a polydisperse distribution has a major effect on the convergence statistics. Two simulations, for 1000 second run times, were completed, the first containing the aerosol distribution in Fig.(2.6) and the second with no input distribution. Therefore just the number of particles were counted at each matrix point in the second simulation, they were not scaled by their relative sizes so the distribution was monodisperse.

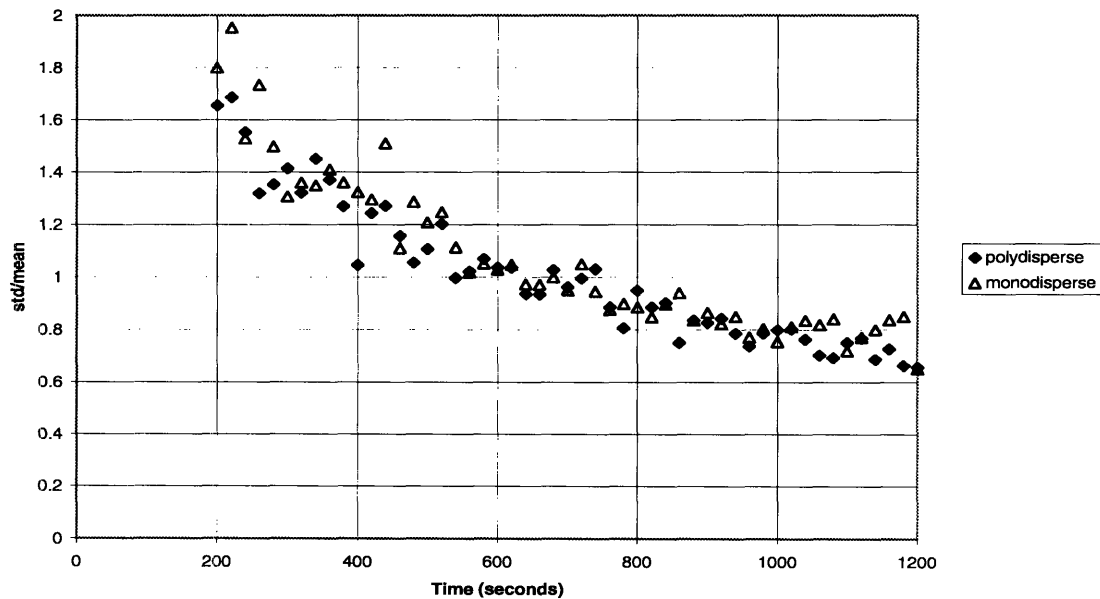


Figure 4.6: Convergence rates for monodisperse and polydisperse aerosol distributions.

The above graph contains the convergence ratios, $\frac{s_n}{n}$ for the two separate distributions. The effect of polydispersity appears to be negligible. These results are among the most important findings of the numerical simulations because they show that the statistical model is accurate for polydisperse situations as found in most experiments.

4.3.3 Effects of Sample Size

In all simulations the sample mean and sample deviation were calculated by sampling the deposition matrix at 210 points. At this number it was assumed the sample mean would be a good approximate to the true mean. As can be seen in Fig.(4.5) this assumption appears to be a valid one. A simulation was run with a parameter, λ of 50 but with a sample size, N , of 9 instead of 210. The following graphs were obtained:

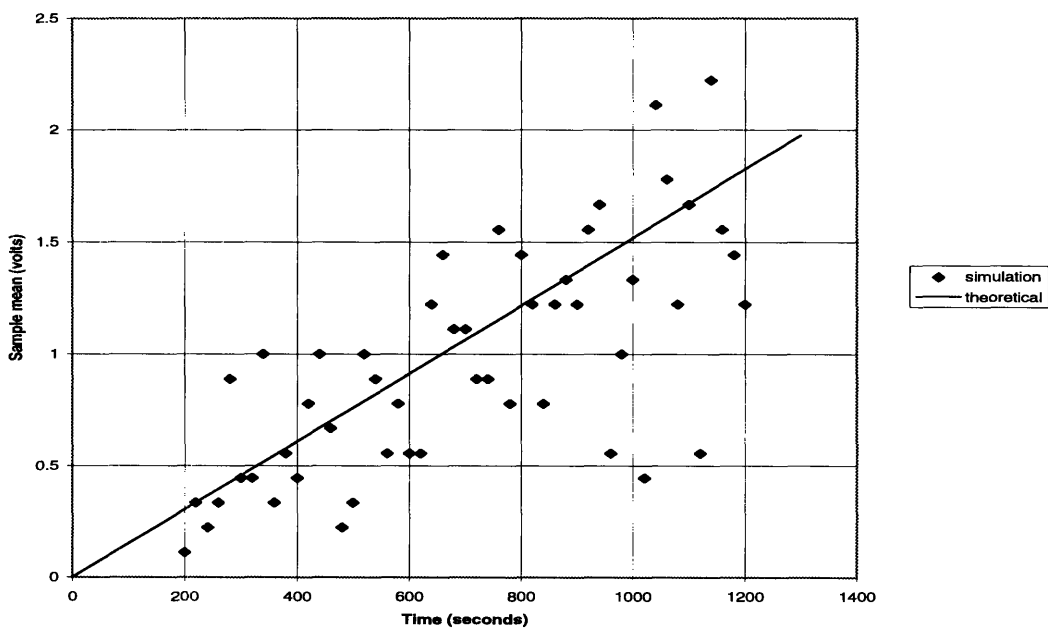


Figure 4.7: Mean voltage versus time for a sample size of 9 data points per sample

The theoretical mean is plotted from, $\mu_n = \lambda AT = \frac{50}{32913} \cdot T$. The theoretical standard deviation is plotted from, $\sigma_n = \sqrt{\lambda AT} = \sqrt{\frac{50}{32913} \cdot T}$;

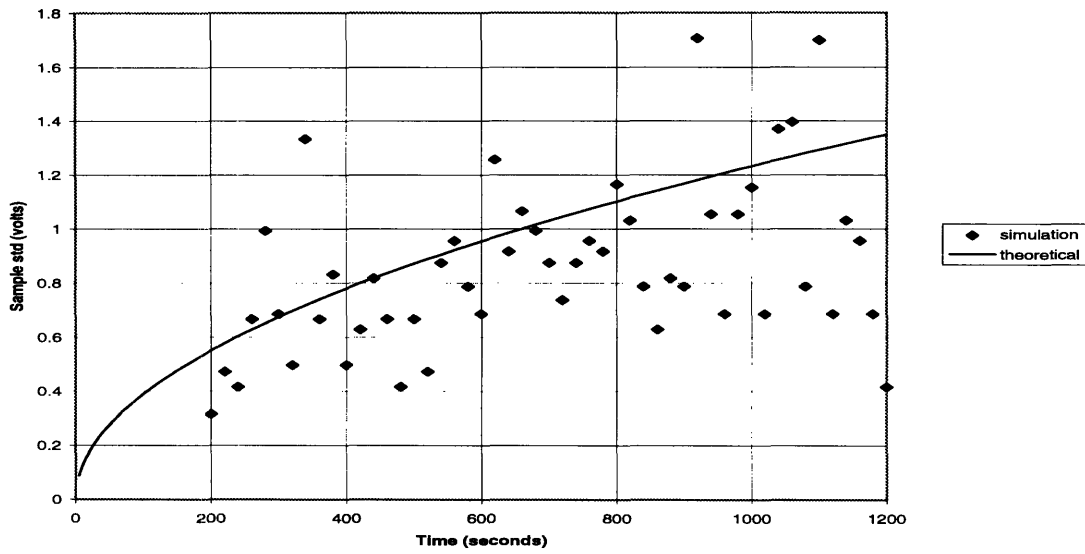


Figure 4.8: Standard deviation versus time for a sample size of 9 data points per sample

Finally the theoretical convergence ratio is plotted from, $\frac{\sigma}{\mu} = \frac{1}{\sqrt{\frac{50}{32913} \cdot T}}$;

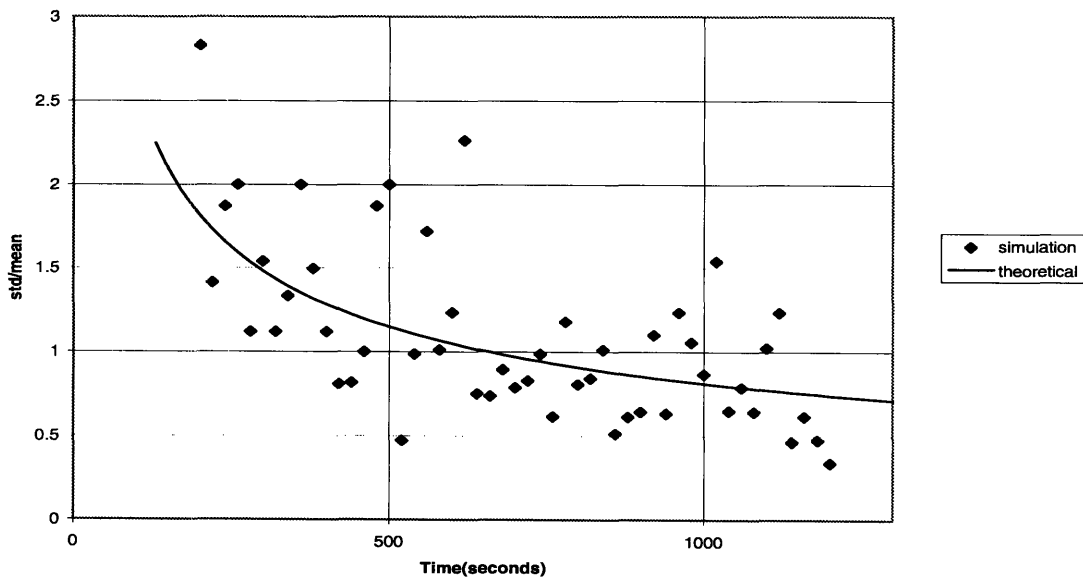


Figure 4.9: Convergence ratio for a sample size of 9 data points per sample

The three previous graphs were for a monodisperse distribution. If a graph, of the respective convergence ratios for a polydisperse and monodisperse distributions, is plotted;

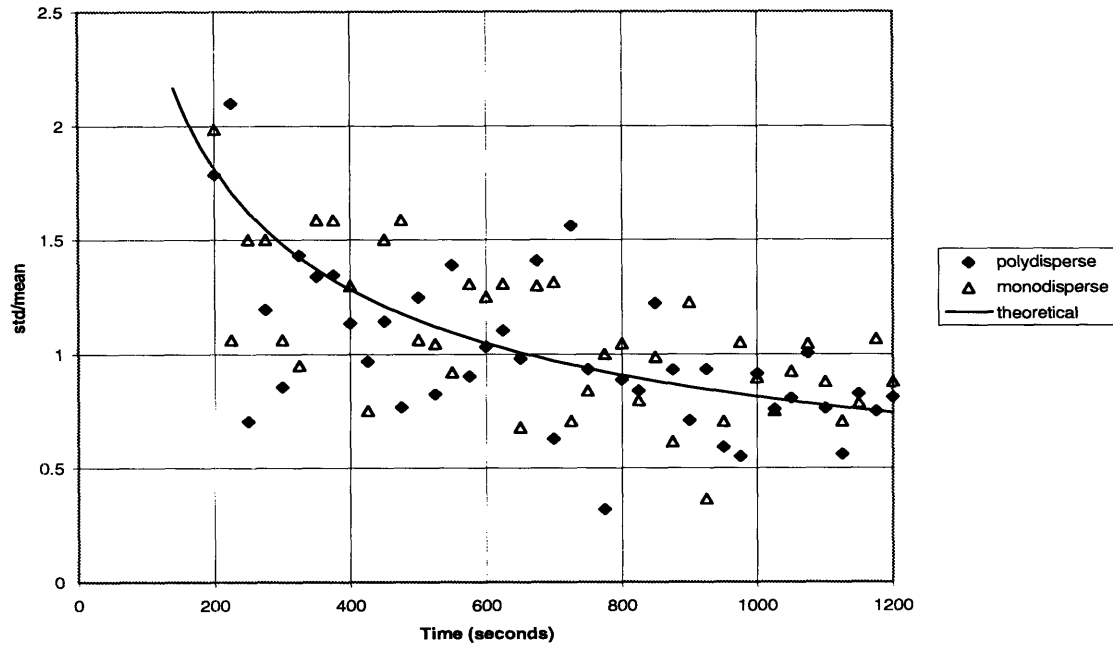


Figure 4.10: Comparison of monodisperse and polydisperse distributions for 9 sample points.

A great deal of scatter is seen on all the above graphs. Although the general trend of the theoretical curves are followed, most individual points are inaccurate, some being off by a factor of over 100%. Also a polydisperse distribution tends to cause more scatter in the data at low sample sizes. This clearly demonstrates the need for large sample sizes in order to effectively estimate the true mean and true standard deviation.

A 95% confidence interval for the true mean is as follows [2]. For a sample size greater than 30,

$$\bar{n} - \frac{1.96\sigma_n}{\sqrt{N}} \leq \mu_n \leq \bar{n} + \frac{1.96\sigma_n}{\sqrt{N}} \quad (4.14)$$

where N is the number of samples taken to calculate the sample mean. With $\sigma_n = \sqrt{\lambda AT}$ this gives

$$|\mu_n - \bar{n}| \leq 1.96 \cdot \frac{\sigma_n}{\sqrt{N}} = 1.96 \sqrt{\frac{\lambda AT}{N}}$$

For a sample size, N of 210 points, $|\mu_n - \bar{n}| \leq \pm 0.135\sigma_n$. This shows that the error in the sample mean increases in time. The percentage error, however, is of greater significance:

$$\frac{|\mu_n - \bar{n}|}{\mu_n} \leq \frac{1.96}{\sqrt{N}} \cdot \frac{\sigma_n}{\mu_n} = \frac{1.96}{\sqrt{N}} \cdot \frac{1}{\sqrt{\lambda A T}} \quad (4.15)$$

Therefore, for our sample size, N of 210 points, the percentage error becomes

$$\frac{|\mu_n - \bar{n}|}{\mu_n} \leq \frac{1.96}{\sqrt{N}} \cdot \frac{\sigma_n}{\mu_n} = 0.135 \frac{\sigma_n}{\mu_n}. \text{ If } \frac{\sigma_n}{\mu_n} = 0.5 \text{ then:}$$

$$\% \text{ error} = 6.5\%.$$

While for 9 sample points, $\% \text{ error} = 33\%$.

If a deposition rate is fixed and the time for an experiment is constrained by other factors then eq.(4.15) can be used to estimate the required sample size, N needed to obtain a small percentage error in the calculation of the sample mean. These statistical methods are discussed in more detail in Appendix C.

Chapter 5

Experiments

In this chapter, experiments with water based aerosols doped with fluorescein dye are described. Eight experiments were conducted. Each parameter that affects the number of deposited particles was kept constant except for time which varied from run to run.

5.1 Experimental Procedure

The array generator was placed in the settling section of the wind tunnel (fig.2.3) about 20 inches from the contraction. It was necessary to have a procedure that was highly repeatable. The probability of aerosols depositing along the measurement area in the channel must not vary from experiment to experiment. The only parameter allowed to vary is the length of time for which the experiment runs. From eq.(4.12), which is repeated here for the reader's convenience, the convergence ratio depends on λ and T .

$$\frac{\sigma_n}{\mu_n} = \frac{1}{\sqrt{\lambda TA}}$$

The time, T , varies while every effort is made to keep the parameter λ (no. of particles arriving/unit time/ unit area) constant. In this way, the convergence can be monitored as a function of time only.

In order to do this, it is necessary that the air flow through the wind tunnel is not obstructed or varied between runs. Therefore the motor speed was always set at 50% of its maximum rated value which produced a test section velocity of 10m/s. The doors of the laboratory were always left open during runs. No experiments were every run while there was obstacles, e.g. parked cars, in the area where the wind tunnel vented out the exhaust air.

The dispersion air and the AG pressurizing air were regulated to 1/4 and 20psi respectively, (see fig.3.3). The array generator was moved back and forth across the width

of the contraction area continuously at a speed of 20 inches per minute. If one or more of the jets appeared skewed this meant the array generator was partially blocked. In that case the experiment was stopped and the AG was unclogged as described in section 2.6.

These procedures help ensure that aerosols distribute evenly and equally along the measurement area. In order for the LIF to detect this and give accurate and consistent readings between runs the following steps must be taken. The signal received from the system depends on two parameters, the first is the concentration of fluorescein dye in the water and the second is the intensity of the incoming laser light. To keep measurements consistent, the fluorescein was always kept at a concentration of 0.001% in the water solution. If a different concentration was desired, the fluid lines, filters and aerosol fluid tank must first be cleared of existing fluid. Then at least 10 liters of the new solution must be pumped through the system to purge the lines. However in our case the experiments always had a fluorescein concentration of 0.001%. The laser power also effected the signal strength. The larger the incoming laser power, the larger the intensity of the returned signal. The laser power was always kept at a value of 1mW. As it passes through the optics it is attenuated to a value of around 0.1mW. The power reading is taken from the internal power meter attached to the laser. Over a period of time the laser tended to drift. This was a nuisance as every minute the power meter had to be checked and the power adjusted to maintain the output at a constant value of 1mW.

Once these procedures were developed experiments were run. If any conditions or parameters changed during the test, the data was then disregarded. Experiments lasting 100, 150, 180, 210, 240, 300, 330 and 360 seconds were completed. Run times shorter than these gave low signal to noise ratios while longer run times were not possible due to rivulets travelling through the measurement area. A total of 280 data points were taken for each experiment. These were plotted on a frequency histogram, with the signal strength

(voltage) along the x-axis and the number of observations of each voltage, or relative distribution, along the y-axis. These plots can be seen on the following pages.

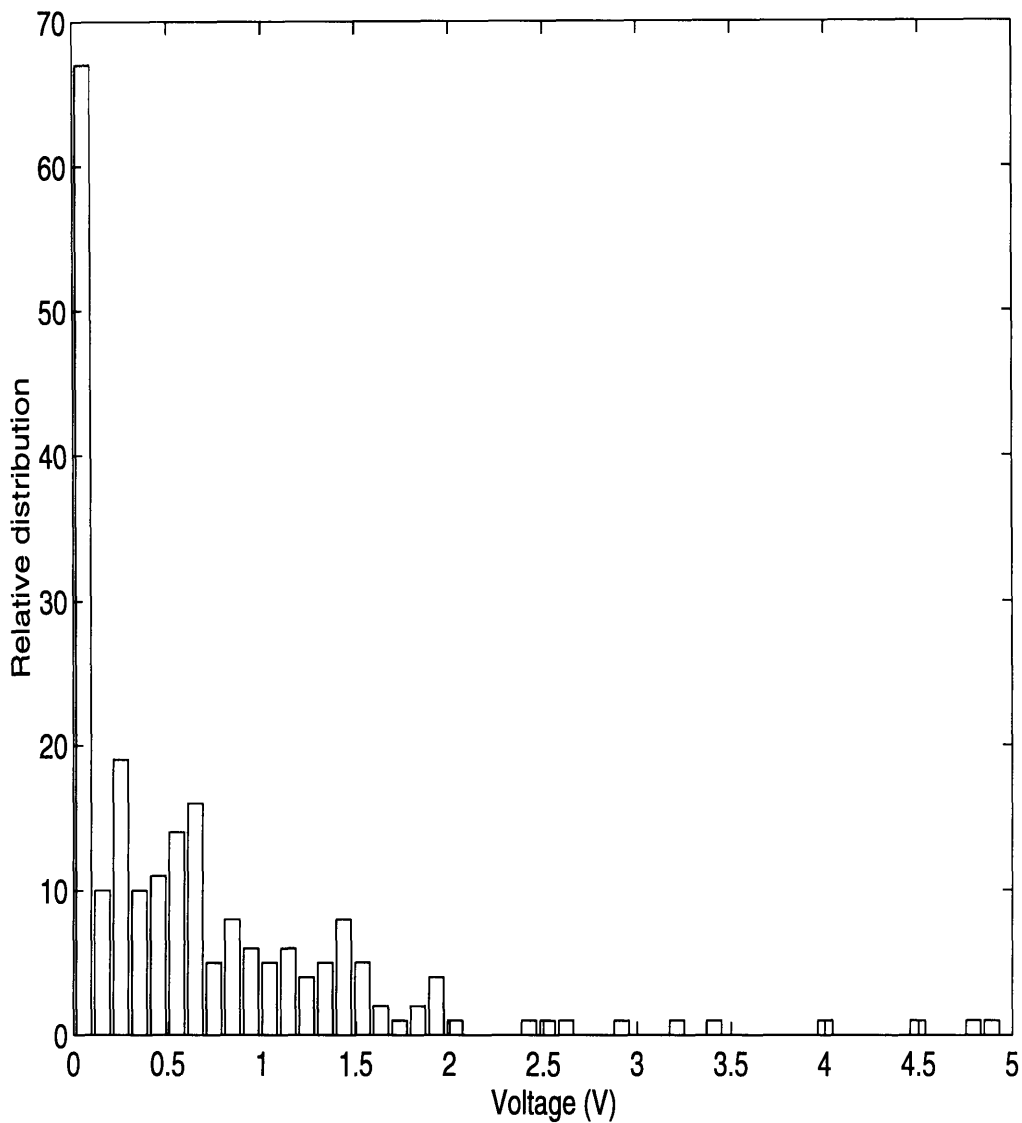


Figure 5.1: Frequency histogram for an experimental run time of 100 seconds. The mean LIF voltage for this experiment is 0.270 volts and the standard deviation is 0.84 volts.

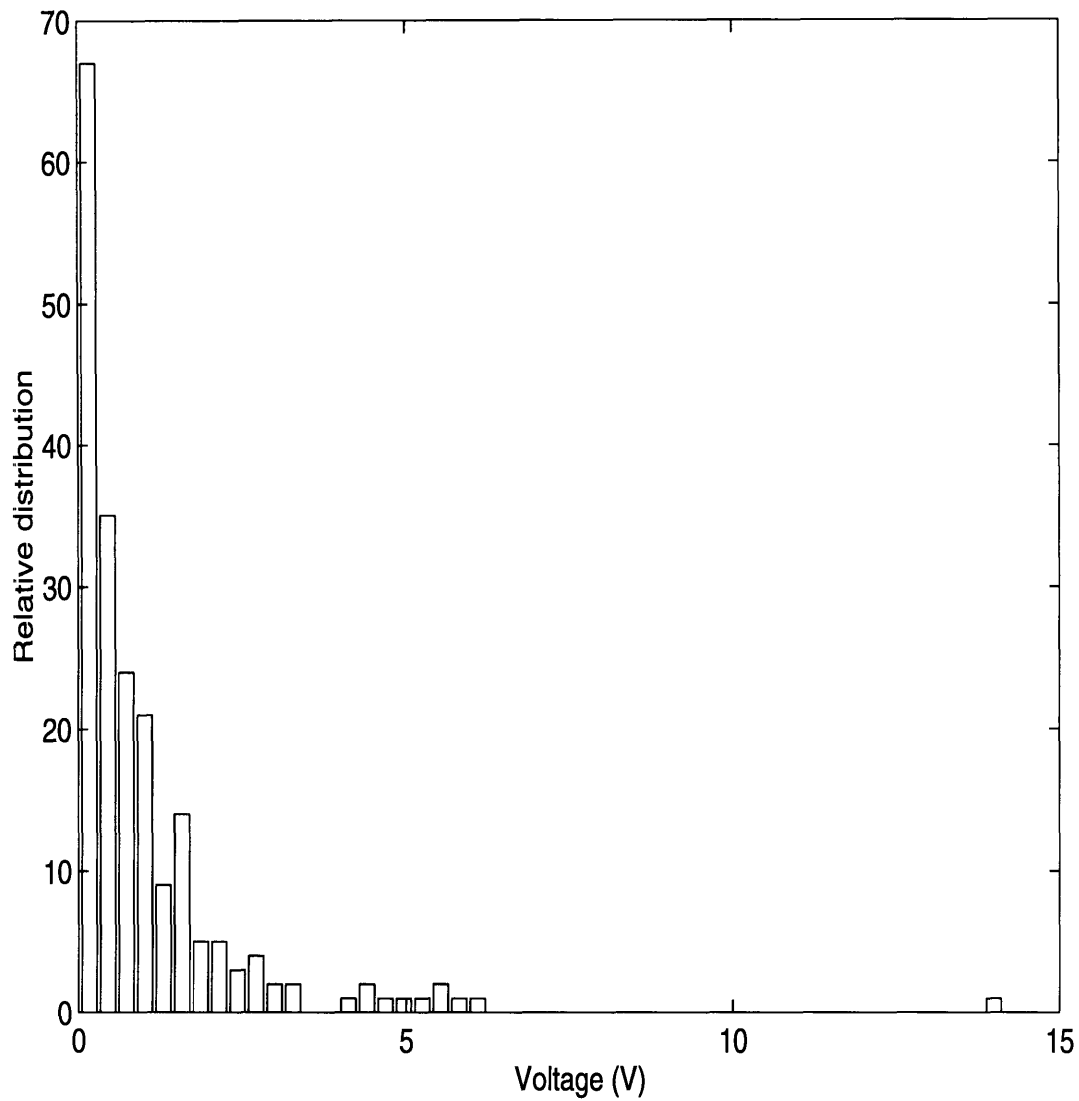


Figure 5.2: Frequency histogram for an experimental run time of 150 seconds. The mean LIF voltage for this experiment is 0.546 volts and the standard deviation is 1.500 volts.

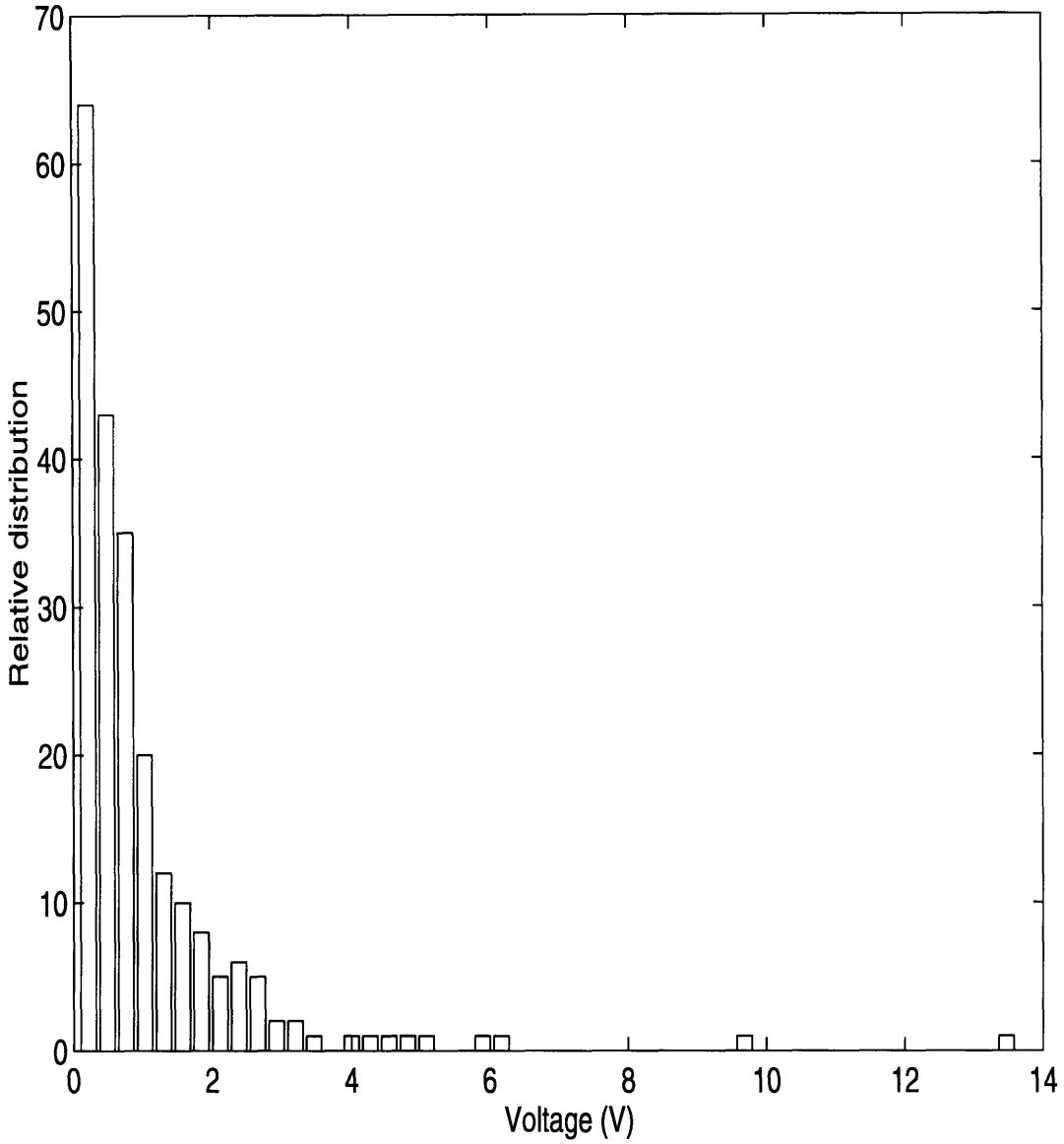


Figure 5.3: Frequency histogram for an experimental run time of 180 seconds. The mean LIF voltage for this experiment is 0.655 volts and the standard deviation is 1.451 volts.

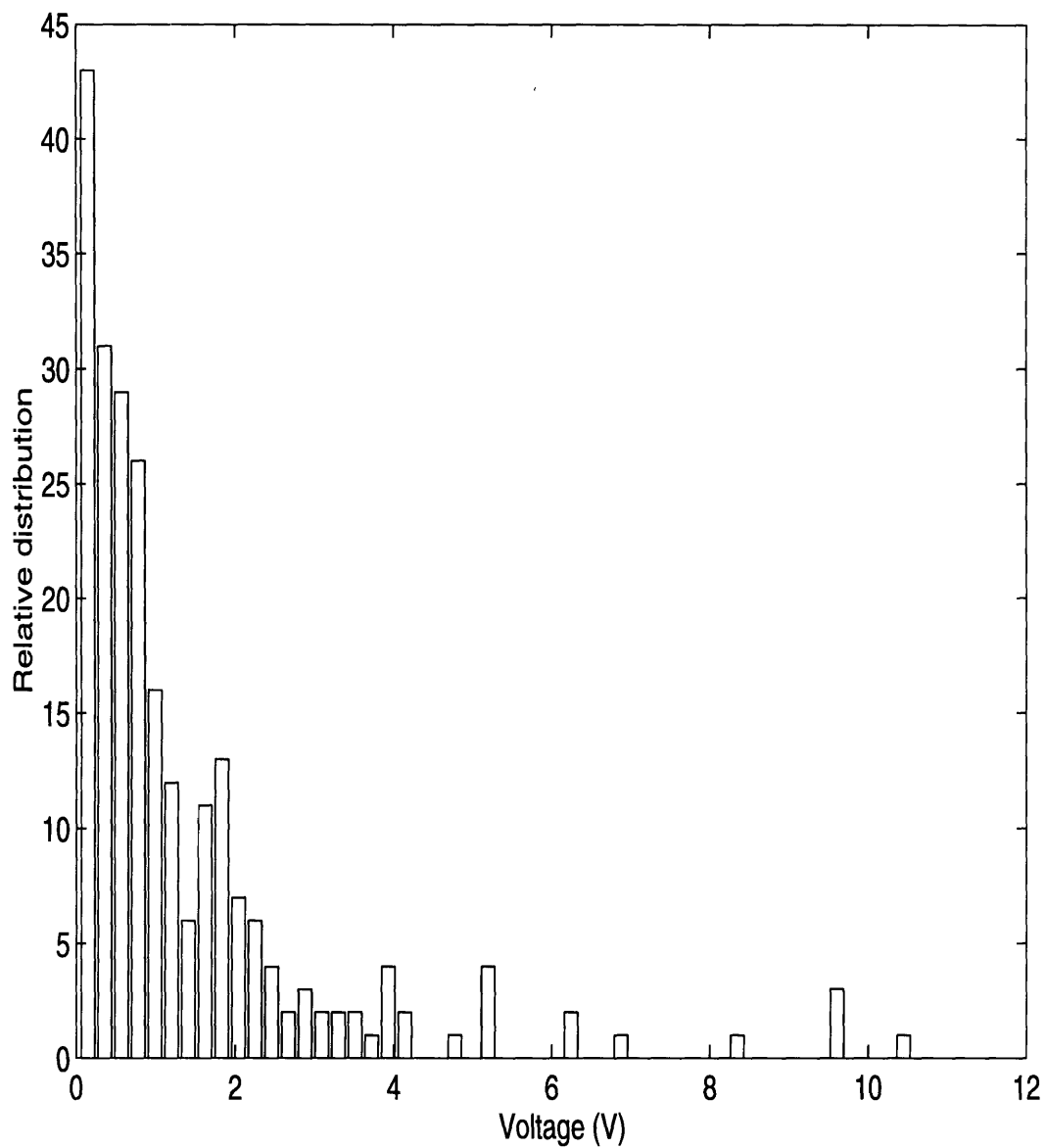


Figure 5.4: Frequency histogram for an experimental run time of 210 seconds. The mean LIF voltage for this experiment is 0.766 volts and the standard deviation is 1.736 volts.

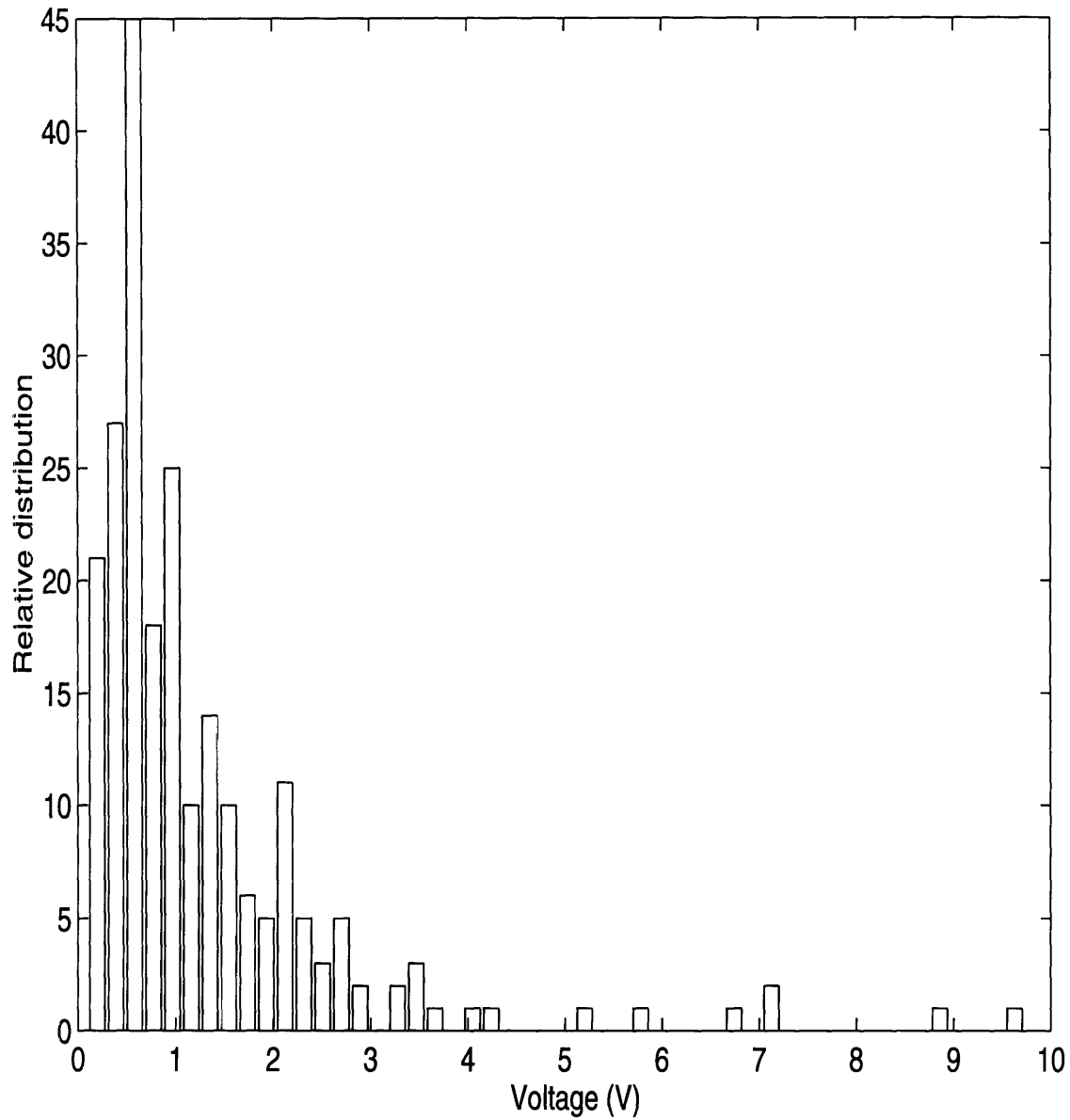


Figure 5.5: Frequency histogram for an experimental run time of 240 seconds. The mean LIF voltage for this experiment is 0.873 volts and the standard deviation is 1.382 volts.

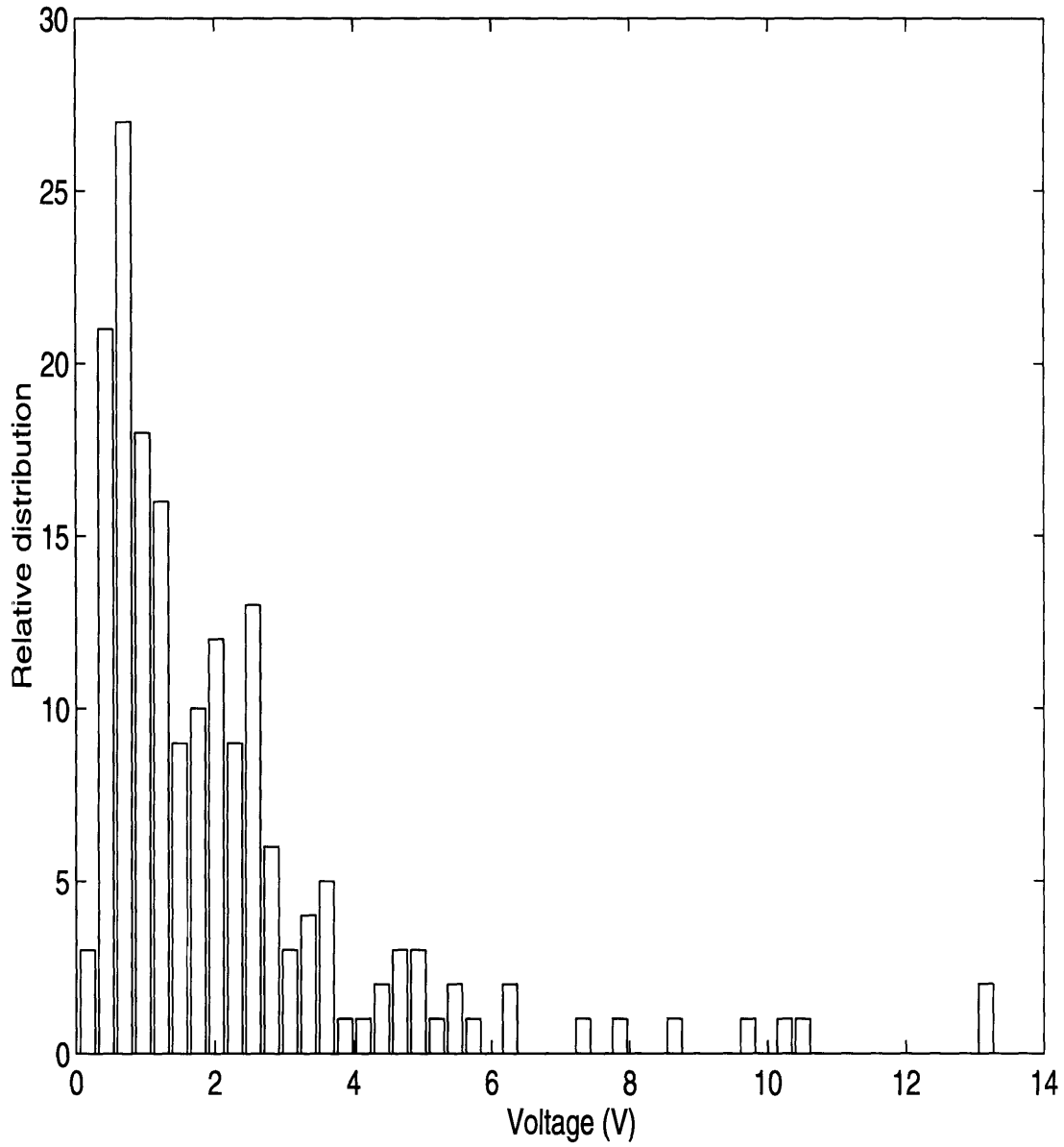


Figure 5.6: Frequency histogram for an experimental run time of 300 seconds. The mean LIF voltage for this experiment is 1.494 volts and the standard deviation is 2.204 volts.

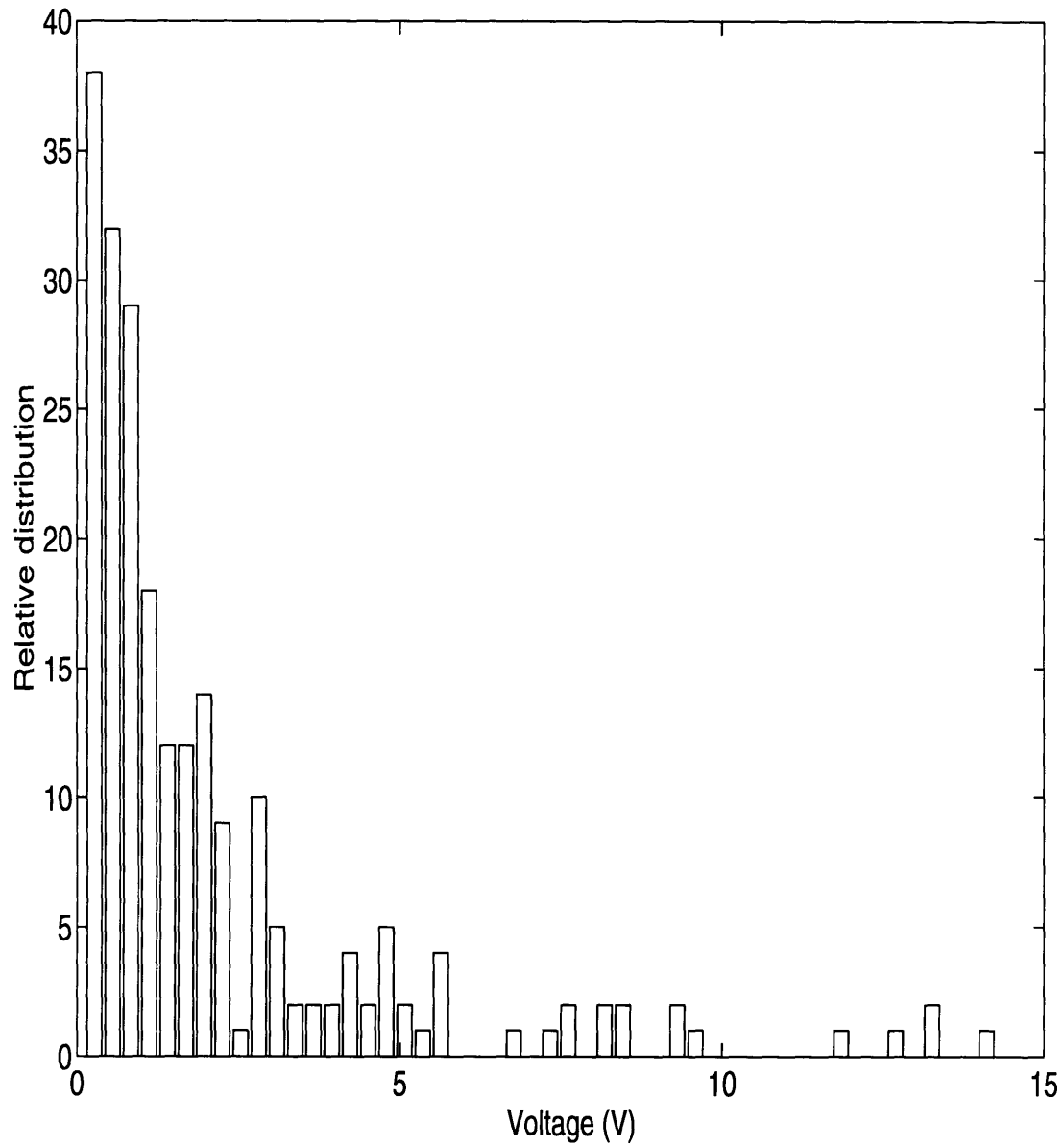


Figure 5.7: Frequency histogram for an experimental run time of 330 seconds. The mean LIF voltage for this experiment is 1.226 volts and the standard deviation is 2.589 volts.

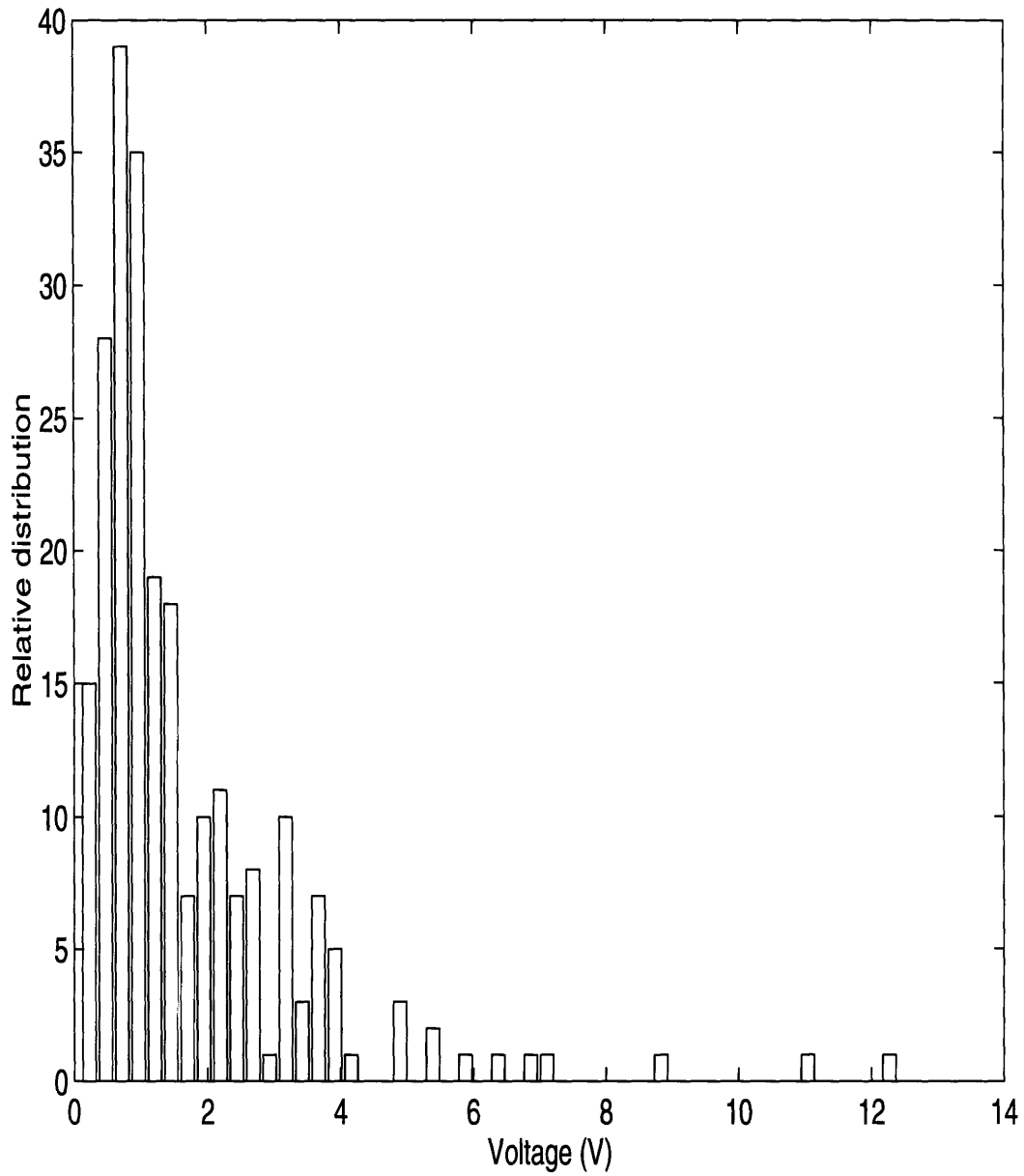


Figure 5.8: Frequency histogram for an experimental run time of 360 seconds. The mean LIF voltage for this experiment is 1.192 volts and the standard deviation is 1.662 volts.

If a graph of the mean voltages of each of the last eight experiments is plotted against each experimental run time the following plot is obtained.

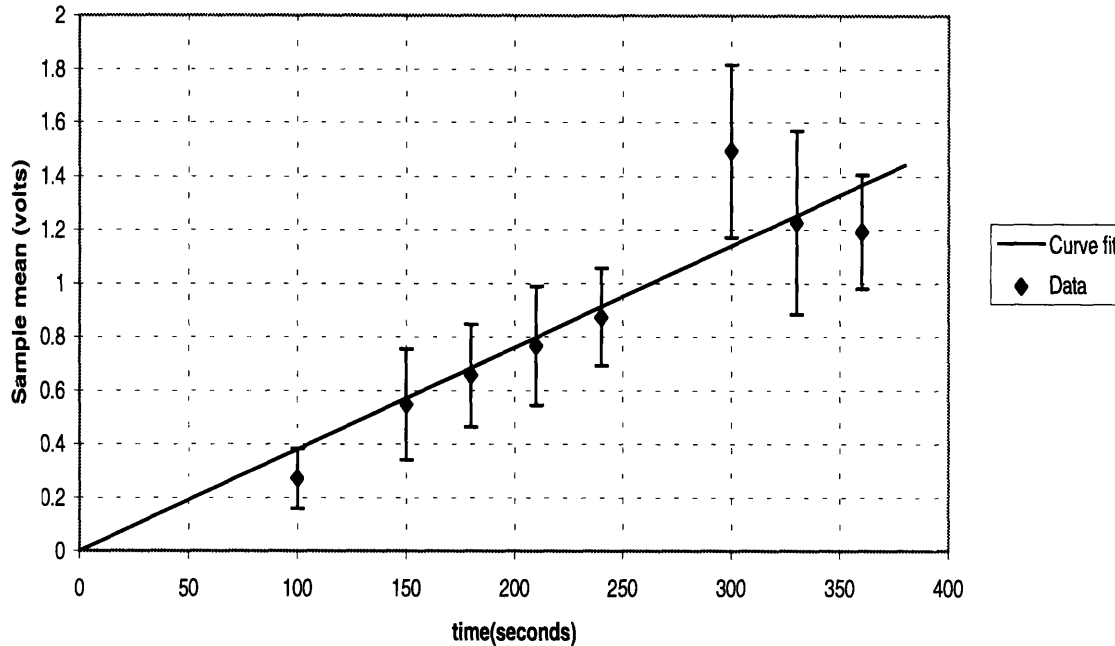


Figure 5.9: Mean voltage versus time.

The point (0,0) was assumed in forming the curve fit because at an experimental run time of 0 seconds no voltage would be recorded. The equation $\bar{n} = 0.003796T$ represents the curve fit, where \bar{n} is the mean voltage (V) and T is the time (seconds). With the exception of the 300 sec and 360 sec data points the points are very linear indicating that the mean voltage is directly proportional to the time. The error bars for the individual mean readings are calculated using a student t-test with a 95% uncertainty level. The reader is referred to Appendix C for a more complete explanation on how the error bars on this graph and on other graphs were calculated.

If the standard deviation of each experiment is plotted against the experiment time the following graph is obtained.

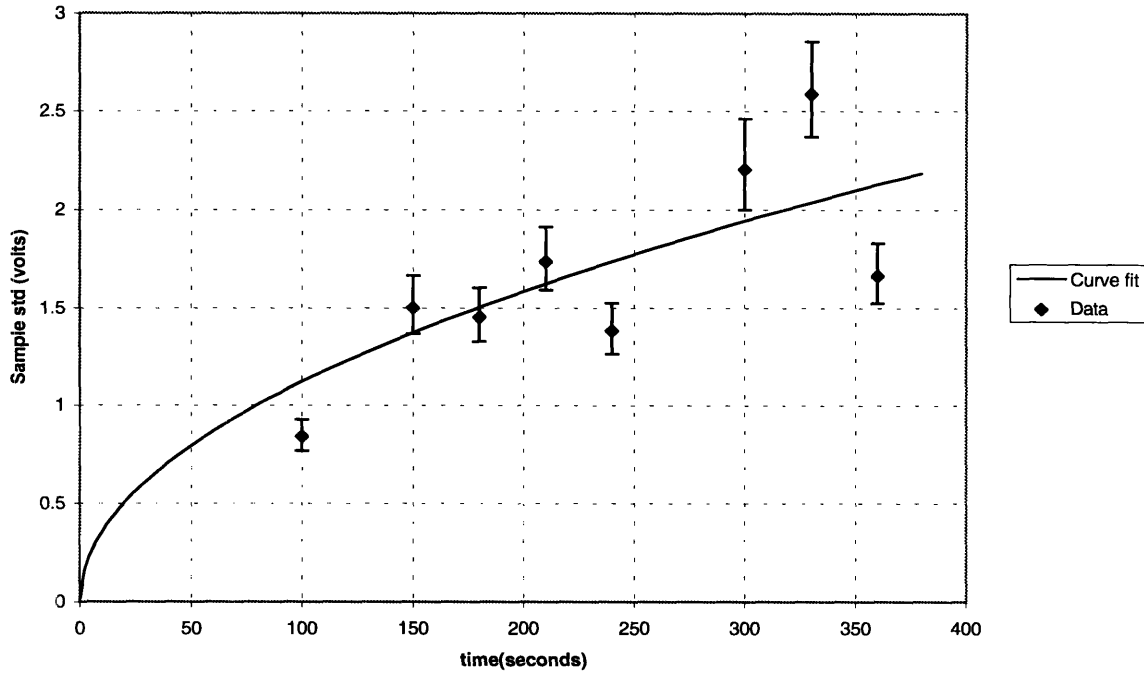


Figure 5.10: Standard deviation versus time.

The equation $s_n = 0.1121\sqrt{T}$ is plotted with the data where s_n is the standard deviation and T is the time. The curve fitted to the data is assumed to be proportional to the square root of time. The error bars were calculated using 95% uncertainty level with the chi-square test. (See Appendix C)

By rearranging eq.(4.12), λ may be determined:

$$\lambda = \left(\frac{\mu_n}{\sigma_n}\right)^2 \frac{1}{TA} \quad (5.1)$$

If the parameters that govern each experiment remain constant, the value of λ should be the same for each experiment. Using eq.(5.1) the value of λ is plotted against time in Fig.(5.11) assuming that $\mu_n \approx \bar{n}$ and that $\sigma_n \approx s_n$.

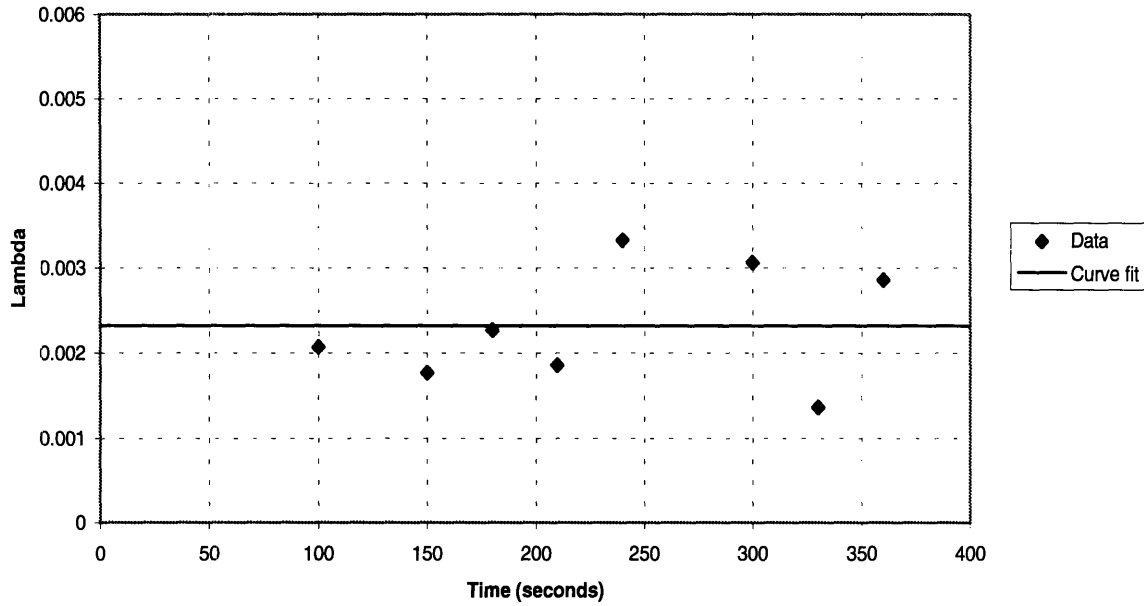


Figure 5.11: Lambda (λ) versus time.

Although the data for this plot is somewhat scattered, the data are centered about a single value. The mean value of λ is 0.00232 particles/area/sec, with a standard deviation of 11%. Substituting this value into eq.(4.12) and letting the time, T, vary between 5 and 370 seconds the standard deviation to mean ratio, $\frac{\sigma_n}{\mu_n}$, can be plotted. The following graph contains this plot with the actual experimental data points for $\frac{s_n}{n}$ included for comparison.

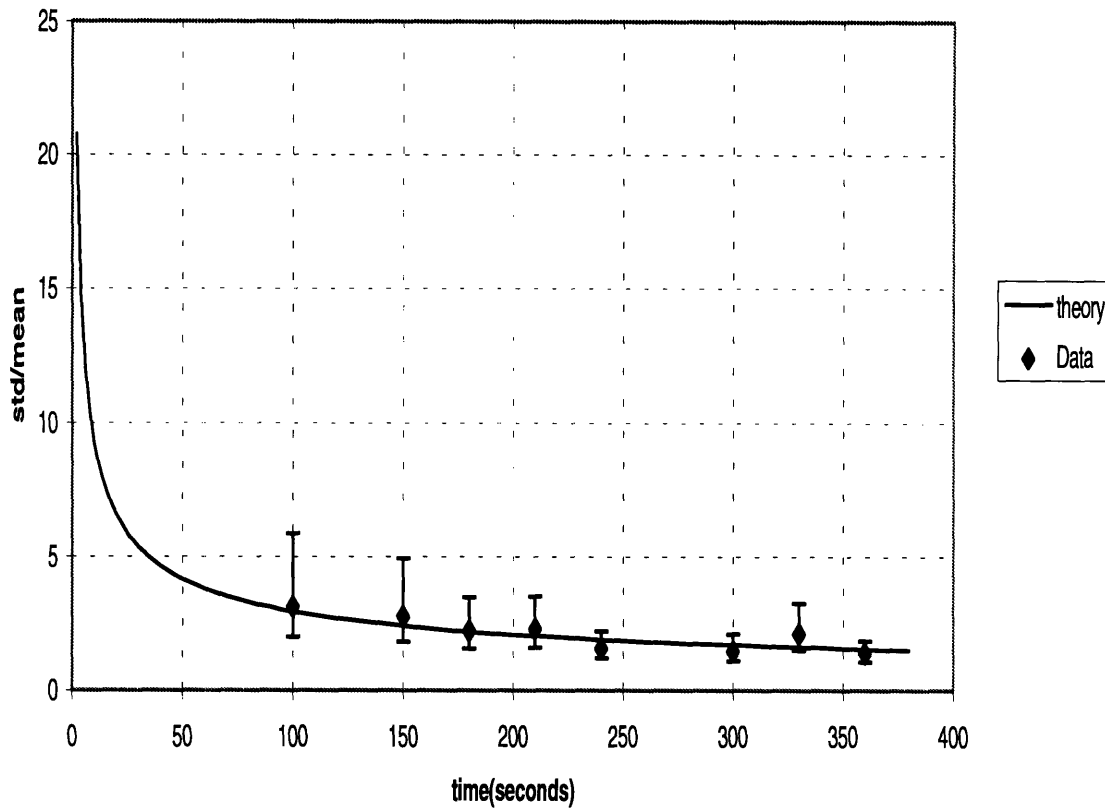


Figure 5.12: Standard deviation to mean ratio versus time.

It is important to note here that the model line plotted in figure 5.12 is not a curve fit. It represents the standard deviation to mean ratio from eq.(4.12) for a value of λ equal to 0.00232 particles/ mm^2 /sec.

The experimental data can be seen to fit the theoretical curve quite accurately, thereby verifying experimentally the model represented by eq.(4.12). Experiments longer than 360 seconds were difficult to run due to very high levels of aerosol deposition in the channel. This led to rivulets which destroyed deposition on the surface. The high deposition levels also led to the LIF signal reaching the voltage saturation limit of the amplifiers. Experiments shorter than 100 seconds were difficult to run because the lack of sufficient deposition did not provide an adequately high signal to noise ratio for the LIF system.

The AG was originally placed at a location 35 inches from the mouth of the contraction as compared with the 20 inches used for all experiments presented throughout this thesis. This gave a much lower number density in the channel than for these experiments, as sedimentation removed many of the particles. With the AG 35 inches upstream experiments could be performed for up to two hours. Several such experiments were performed for various time periods ranging from half an hour to two hours. Unfortunately the data from those tests was inconsistent and unreliable. Evaporation was blamed for this. The longer run times meant more time for evaporation to occur. The lower aerosol number densities meant that there was a high surface area to volume ratio for the isolated deposited droplets which promoted higher evaporation rates. This is why the present AG configuration was used. The higher aerosol number densities humidified the channel and reduced evaporation. The shorter run times also helped inhibit evaporation by reducing the effective time available for evaporation to occur.

5.2 Experiment versus Numerical Results

The next step is to compare these experimental results to the simulations performed in subsection 4.3.1. From figure.(5.11) the experimental value for λ was 0.00232 particles/ mm^2 /second. When this value is multiplied by the test area, the corresponding parameter input to the simulation, 48 particles/sec is obtained. The simulation starts at 10 seconds, calculates the ratio, s_n/\bar{n} , increments itself by 10 seconds and repeats this procedure up to a final time of 400 seconds. The analytical solution is based upon the simulation where the following equation was used:

$$\frac{\sigma_n}{\mu_n} = \frac{1}{\sqrt{\frac{48}{32913} \cdot T}}$$

Collecting the experimental, numerical and analytical results yield the following graph.

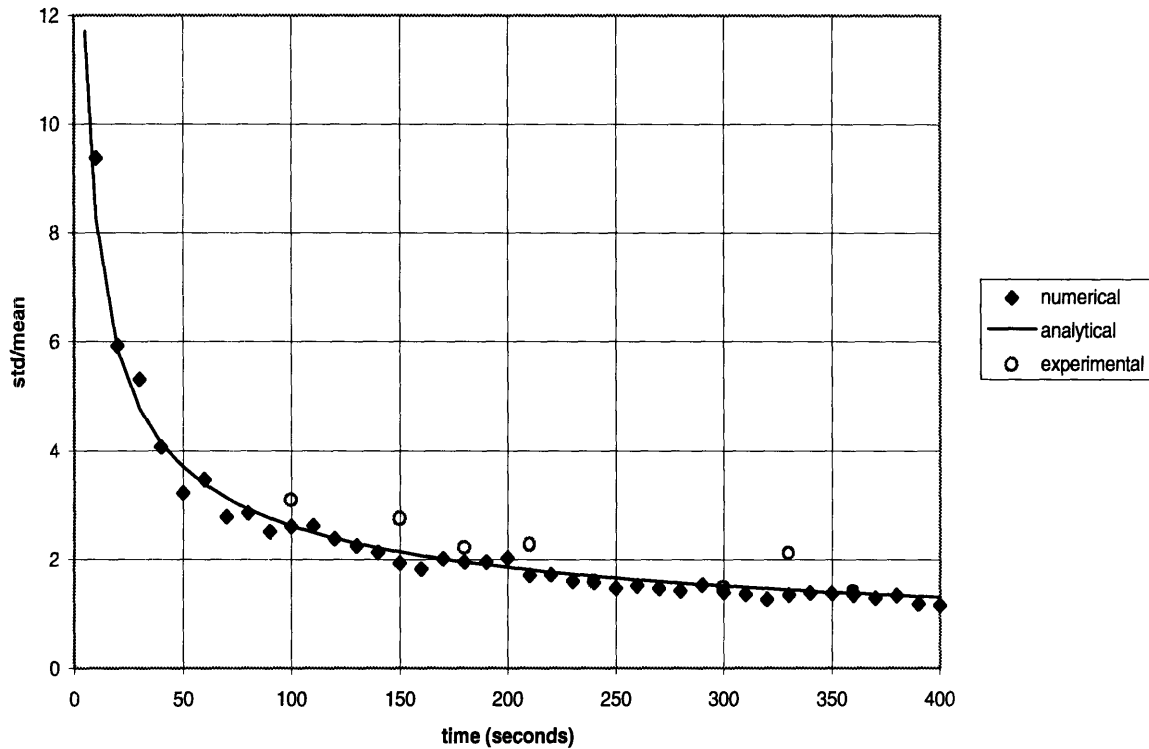


Figure 5.13: Convergence ratio versus time

The agreement is very good despite the assumptions that went into the simulation model. The experimental data points for 240, 300, 360 seconds are difficult to see because they lie on the analytical curve. The original criterion for convergence was stated as being when, $\frac{\sigma_n}{\mu_n} \leq 0.1$. Applying this to the experimental data yields the following condition:

$$0.1 = \frac{1}{\sqrt{0.00232 \cdot 0.5 \cdot T}}$$

The corresponding value for time, T , is approximately 24 hours. This is an extremely long time, far too long to run an experiment for. It corresponds to a total of 200 particles arriving in each $0.5mm^2$ over the entire time period. Such a high number density is

extremely difficult to reach experimentally. This is because the actual volume of aerosols needed would flood the test section. The deposition would not be possible to measure because discrete droplets would not exist, they would form part of a liquid continuum. Therefore our ideal convergence ratio of 0.1 is not achievable in practice.

However, the convergence ratio that would limit errors in a single measurement to 10% can be obtained from equation (4.15);

$$\frac{|\mu_n - \bar{n}|}{\mu_n} \leq \frac{1.96}{\sqrt{N}} \cdot \frac{\sigma_n}{\mu_n} = 0.1$$

or, for $N = 210$, when

$$\frac{\sigma_n}{\mu_n} = 0.1 \left(\frac{\sqrt{210}}{1.96} \right) = 0.739$$

This value is reached after 26.3 minutes, which is quite reasonable. If instead only 9 points per sample were used, the required run time would be more than 10 hours.

Chapter 6

Evaporation of Droplets

This chapter deals with the problem of evaporation of aerosol droplets during the experiments. Various solutions are proposed and analysed. An oil medium for producing the droplets is explored. The experimental results for this medium are presented.

6.1 Evaporation

One of the main causes of experimental error in our system is evaporation of droplets. Droplets evaporate as they travel down the wind tunnel and, after they deposit, they continue to evaporate. This could have a serious effect on the measured deposition. According to Davies [11], a $10\ \mu\text{m}$ water particle in air at 30°C with a relative humidity of 50% evaporates in 0.6 seconds. Even though our particle size was five times larger and temperature 10°C lower it still suggests that significant evaporation occurs as the particle travels downstream. As the particle is deposited on the sintra its surface area is reduced and it is located in a humidified channel both of which would suggest that the evaporation rate would reduce. However the fluorescein dye in the water does not evaporate at all. The effect of water evaporating is to increase the concentration of fluorescein in the droplet. This in turn results in a larger LIF signal. So the system has a natural compensating effect built in which reduces the effect of evaporation on the measured signal. In order for the fluorescein to emit a signal it must be in solution. Experiments have shown that if the entire droplet evaporates the deposited fluorescein will not respond to the laser excitation at all. Therefore it is important to have a high number density in the channel to continually reabsorb deposited fluorescein into solution. It is also important to take the deposition measurements quickly to record a signal before the aerosols completely evaporate.

6.2 Evaporation inhibitors

A solution to this problem is to add substances that inhibit evaporation to the aerosol mixture. Eisner [12] found that droplet life can be increased by a factor of several hundred by adding small quantities of a fatty alcohol in the water by means of a dispersing agent. Davies [11] recommended adding a long chain alcohol called n-docosanol to the water to suppress evaporation. Crow [9] found that up to 25% of evaporation losses on small ponds could be prevented by applying and maintaining a chemical film or monolayer of hexadecanol on the water surface.

All long chain alcohols used are not very soluble in water and do not assume a uniform concentration throughout the water. To insure an adequate monolayer on the surface of each droplet a uniform concentration must be achieved. In most cases a dispersing agent such as ether or ethylene oxide was used to ensure an even distribution. However both of these dispersing agents are extremely flammable and prone to explosion so safety considerations precluded their use.

Roth [28] used two commercially available detergents to help inhibit droplet evaporation. Span-20 and Tween-40, which are two fatty acid esters, were used. They are both surfactants which means they form a monolayer on the surface of the droplet. This layer is what inhibits evaporation. FSN-Zonyl, another surfactant made by DuPont, was also explored. In order to test the evaporation suppressing ability of Span-20 and Tween-40, of FSN-Zonyl, and of n-docosanol the following experiment was devised. Several droplets of known volume were injected with a micro-syringe onto the surface. The laser probe was placed over a droplet and the signal was recorded every minute. In this way the effect of evaporation on the signal strength could be observed over time. The results from four droplets, one containing no inhibitors, one containing a mixture of 1% Span and 1% Tween, one containing 1% Zonyl and finally one containing 1% of the alcohol 1-Hexa-

docasonal. The droplets are 0.1ml in volume which means they are considerably larger than the droplets generated by the AG.

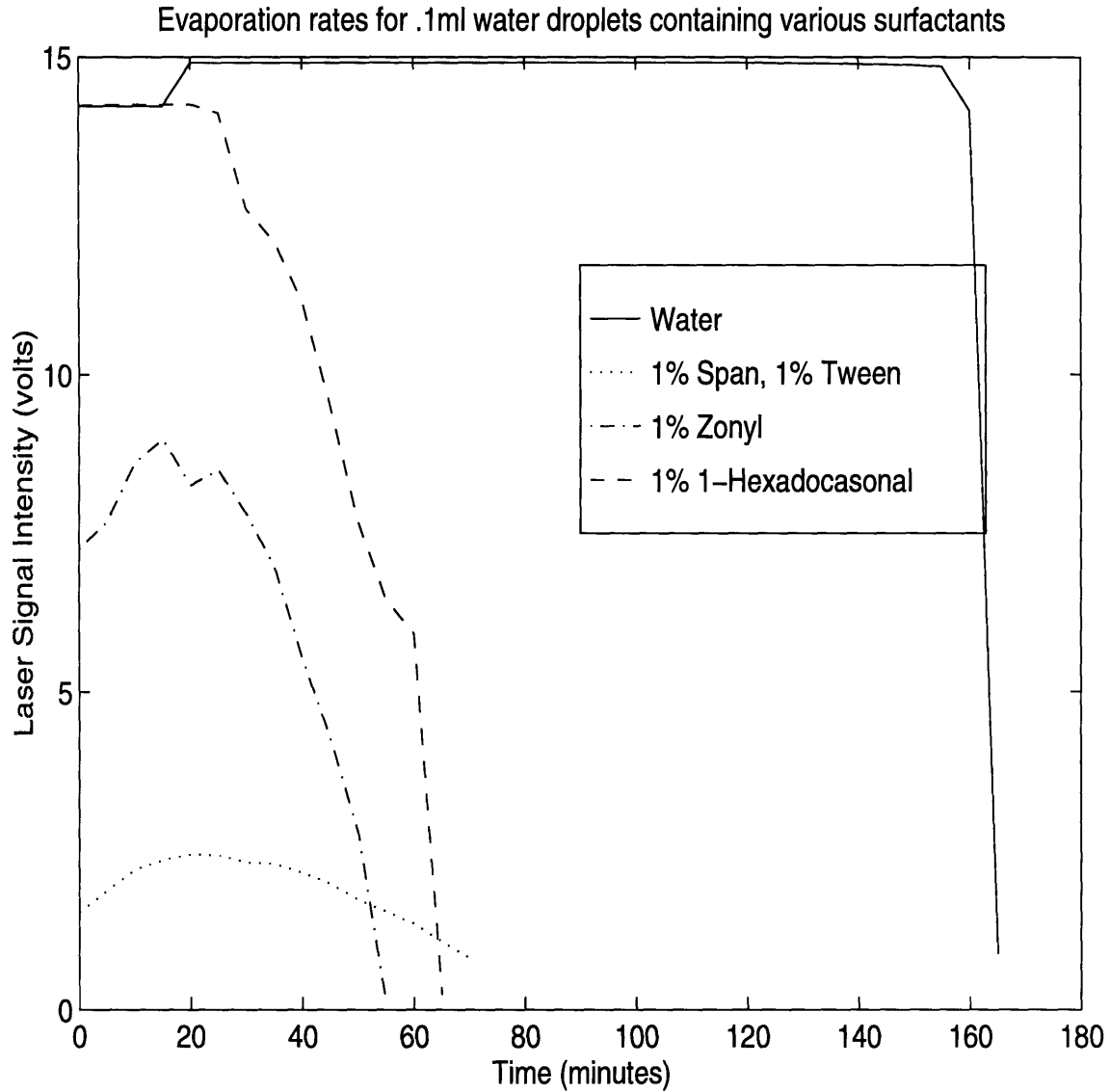


Figure 6.1: Evaporation time for several droplets.

The results from figure 6.1 are very surprising as they seem to contradict results from the literature. The surfactants and the long chain fatty alcohol seem to increase the evaporation rate not reduce it. The water droplet with no inhibitors lasts up to three times longer

than the others. However this particular case is not the same as those reported in the literature. Our droplets were placed on a surface. As a result of the surfactants the surface tension of the water is reduced the droplet tends to spread out more on the surface. This can be seen from the reduced initial voltage received by the LIF for the droplets containing the surfactants. This reduced signal may also be the result of the additional chemicals which may block some of the optical signal. Since the evaporation rate is proportional to the surface area of each droplet the additional spreading increases the rate of evaporation. The rate at which they evaporate may be slower than the pure water droplets, but the larger surface area has a more significant effect. The data also proves that the fluorescein deposited on the surface once the water has evaporated does not produce any meaningful signal. It was decided not to pursue the option of mixing evaporation inhibitors into the aerosol solution once these results were understood.

6.3 Suitable Oils

An obvious solution to this problem is to use a low vapor pressure oil as a liquid for aerosolization. Several oils were investigated; olive oil, mineral oil, lubricating oil, cottonseed oil and sunflower oil. Several properties were required from any potential oil. It must have a low enough vapor pressure to inhibit evaporation. The viscosity must be low so that it flows smoothly through the nebulizer. It must have a low flammability level and be non-toxic since the wind tunnel vented out to the atmosphere. Finally the price was also an issue.

The most suitable oil based on those conditions was found to be a lubricant from Mobil called Velocite-6. Its viscosity at 40°C is approximately 9 times that of water. Considering most oils investigated had a viscosity well over 100 times that of water this figure is relatively good. Its flash point is at 166°C and its vapor pressure is less than 0.1mm Hg

at 20°C (Compare this to water which has a pressure of 22.5mm Hg at a similar temperature). Finally it was non-toxic and inexpensive.

A problem with the Velocite-6, as with every other suitable oil considered, was that the fluorescein will not dissolve in it. The dye just settles to the bottom of the container. It was necessary to find another type of dye that dissolves in oil. This dye must be excited by one of the argon-ion laser lines. The two strongest lines were the blue line at 488nm which is the line used for all of our tests and the green line at 516nm. The photomultiplier tube can detect light anywhere in the visible spectrum; however, two filters at its input block all light outside the 508-528nm range. Nowicki [27] investigated several types of dyes for use. Many firms claimed their particular dyes dissolved in oil but in practice it was extremely difficult to get any dissolution at all. The following table details the dyes that were investigated:

Table 6.1: Fluorescent oil dyes (from Nowicki [27])

Fluorescent Dye	λ max abs	λ max emit	Dissolve in oil	Toxicity	Price per gram
Rhodamine B	554 nm	627 nm	very slightly	possible carcinogen	\$22.75
Coumarin 540A	423 nm	530 nm	very slightly	undetermined	\$44.00
LD 688	516 nm	618 nm	very slightly	possible carcinogen	\$150.00
Nile Red	553 nm	630 nm	slightly	undetermined	\$115.00
Coumarin 500	392 nm	495 nm	very slightly	undetermined	\$59.00
Coumarin 503	393 nm	490 nm	very slightly	undetermined	\$35.00
Coumarin 540	458nm	520nm	very slightly	undetermined	\$62.00
Coumarin 523	442nm	458nm	very slightly	undetermined	\$77.00

A dissolving agent known as dichloromethane was supposed to help dissolve the coumarin dyes in the oil. However this was found not to be the case. The dyes stayed in their crystalline form. Also dichloromethane was a highly toxic material which discouraged its use anyway.

Exciton [14] said that their Pyrromethene dyes should dissolve in oil. Specific dyes numbered 580 and 567 both absorbed light at 518nm which was possible to achieve with our laser. They both emitted at 550nm. However, since they both cost \$150 per gram and as a result of previous failures with other dyes, it was decided not to purchase them.

Finally, a fluorescent oil additive called oil glo 22 was found. It is manufactured by Spectronics Corporation and is used for leak detection in machinery. It is a dark reddish

liquid and is highly soluble in oil. When its solution in oil was placed underneath the laser a signal was detected. This signal was about five times smaller than the fluorescein and water signal, but it was detectable nonetheless. The dye was manufactured for leak detection purposes. It is injected into a system, when the oil glo comes out it fluoresces, in the visible wavelength, under the influence of a mercury lamp. The emitted color is a yellow/green combination which would imply its wavelength is about 510nm. There is no available data for the absorption spectra of oil glo. Since it is excited by a mercury lamp it must have its main absorption bands in the mid 300nm range, but mercury lamps also have visible bands (546nm) so it must also be excited by higher wavelengths.

6.4 Experiments with Oil

Oil glo was mixed at a concentration of 0.02% by volume with the velocite 6. The mixture was too viscous and impure to be used with the array generator so the nebulizer (see section 2.7) was used instead. This gave a more disperse diameter distribution than the array generator and its number density varied as the house air line which drove it fluctuated. However it did not block or clog over time, which was why it was used. The velocity and diameter distributions for the nebulizer and oil (taken with PDPA) are as follows:

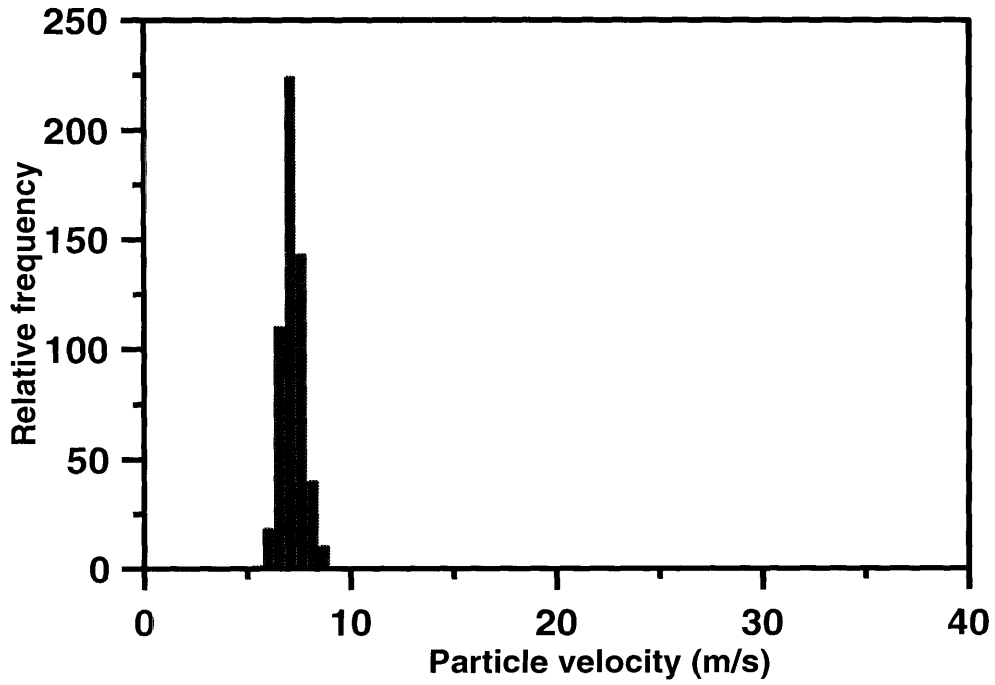


Figure 6.2: Velocity distribution for nebulizer with oil aerosols.

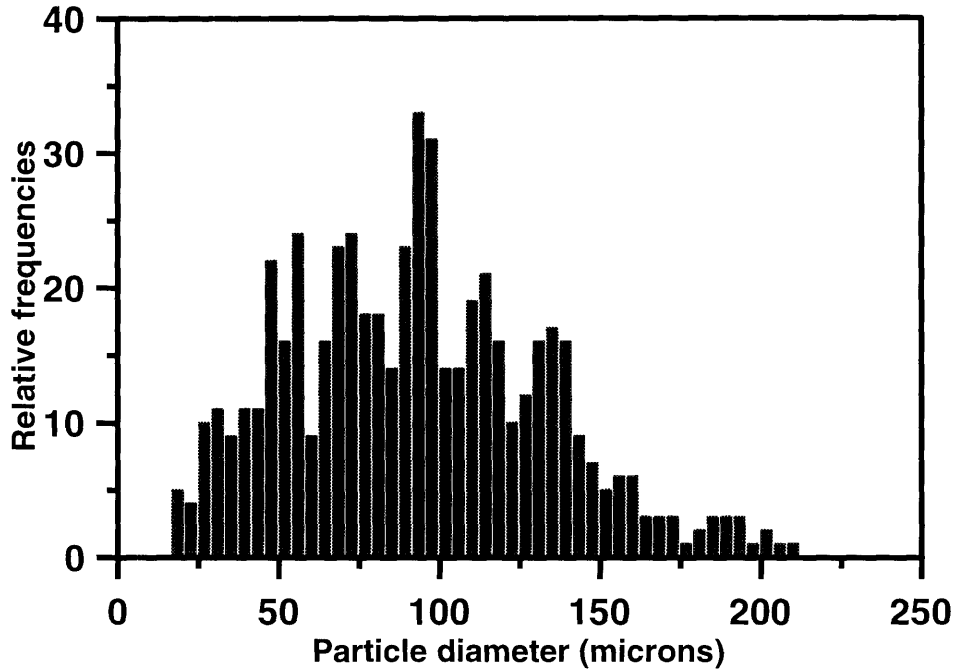


Figure 6.3: Diameter distribution for nebulizer with oil.

The mean velocity for the oil is 7.18m/s while the mean volumetric diameter is $104.5\mu\text{m}$. As can be seen the diameter distribution is very polydisperse.

The experimental setup was the same as for water except the AG was replaced by the nebulizer. The compressed air came from the house air supply at a pressure of 25psi. The nebulizer was not moved from side to side across the channel due to its larger size and because the jet dispersed itself extremely well across the channel width owing to the much higher levels of turbulence in the jet.

Experiments were run for times of 15, 30, 45, 50, 60, 70, 75, 80, 90, 100, 105, 110, 115 and 120 seconds. It was difficult to run for longer times because the oil would form a thin liquid layer on the sintra surface instead of the discrete droplets which were preferred. The lower surface tension of the oil caused it to spread out a lot more than the water-based droplets. Also as the level of oil in the nebulizer decreased the pressure required to generate the same number of droplets increased. Therefore as time increased the number density decreased. Shorter run times were optimal for both these reasons. Some sample distributions are shown;

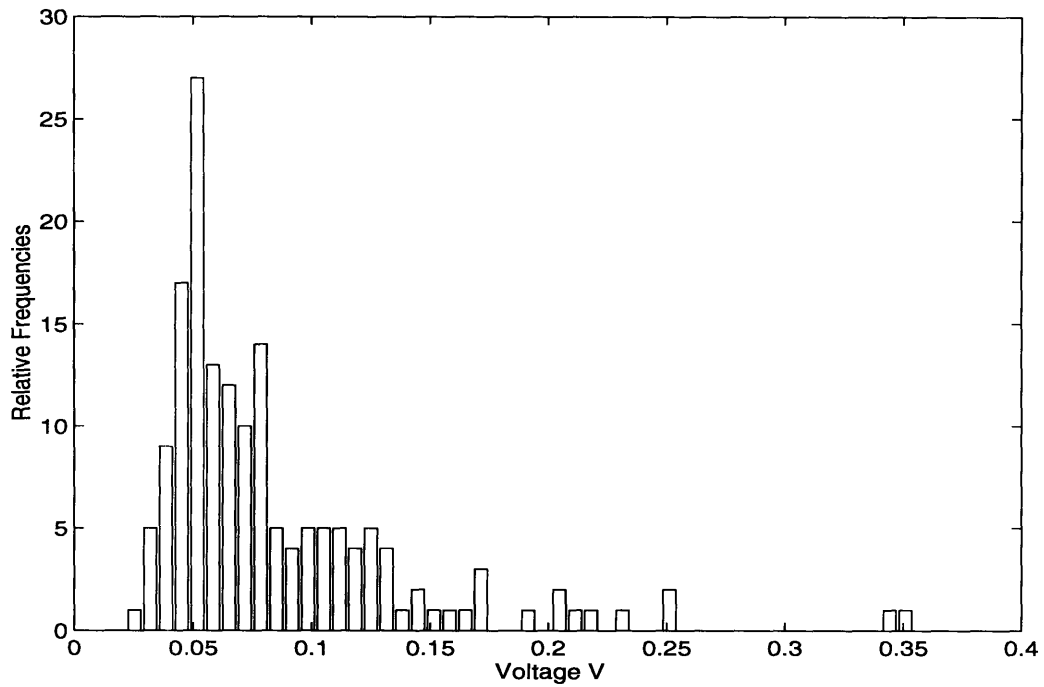


Figure 6.4: Frequency histogram for an experimental run time of 45 seconds. The mean LIF voltage is 0.085 volts and the standard deviation is 0.054 volts.

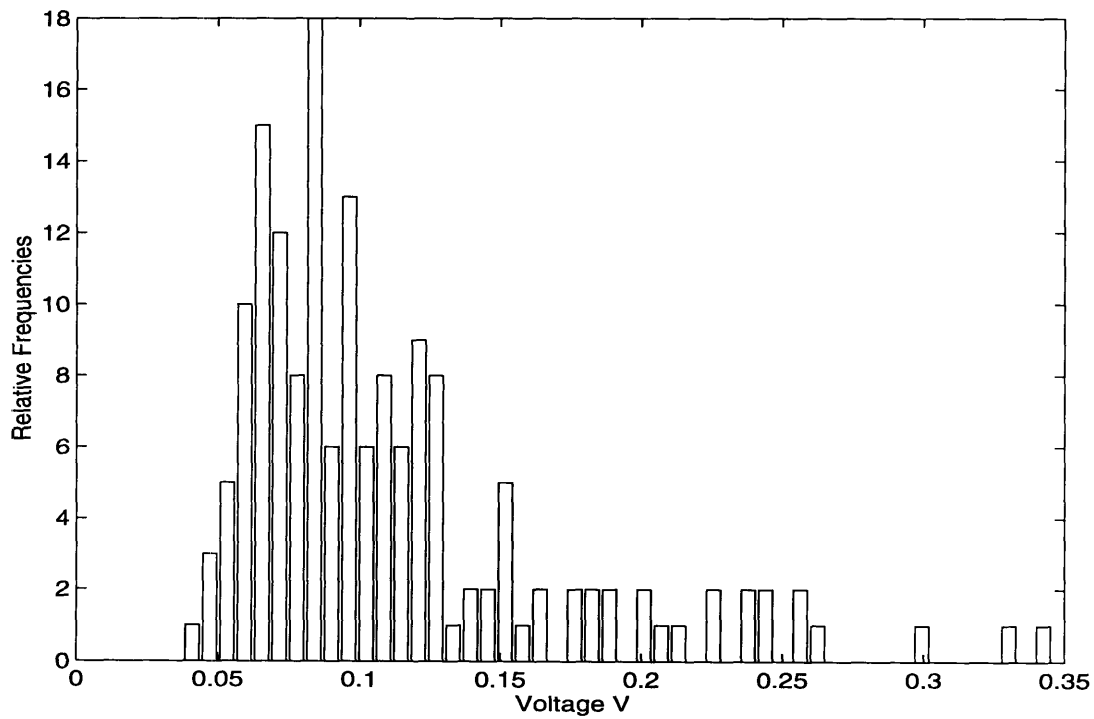


Figure 6.5: Frequency histogram for an experimental run time of 75 seconds. The mean LIF voltage is 0.112 volts and the standard deviation is 0.057 volts

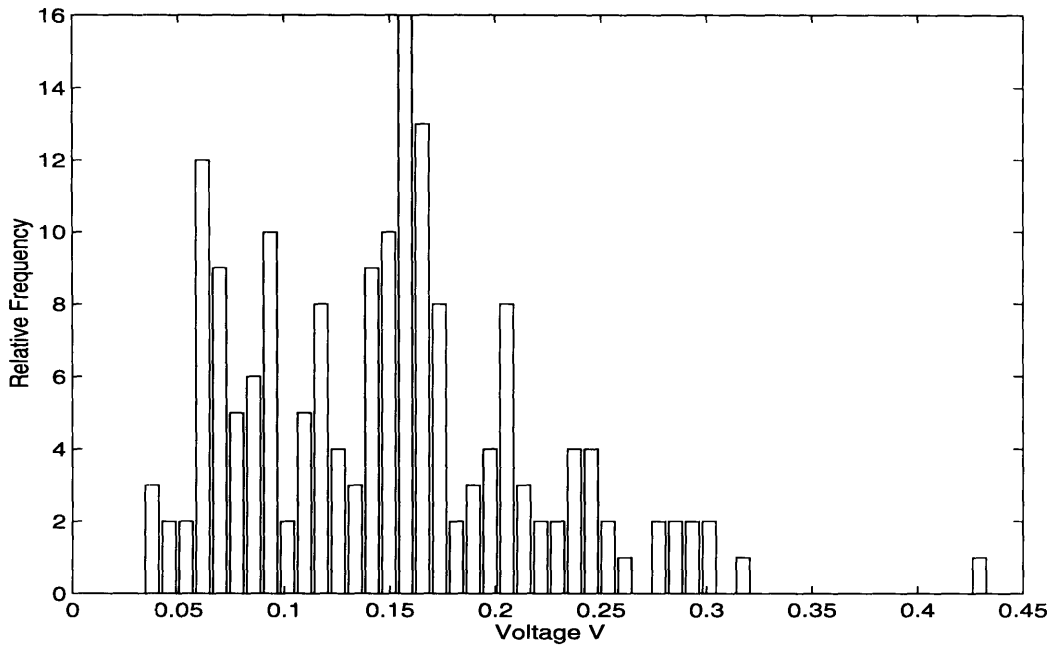


Figure 6.6: Frequency histogram for an experimental run time of 105 seconds. The mean LIF voltage is 0.149 volts and the standard deviation is 0.068 volts

The mean voltage from all of these experiments versus time is shown:

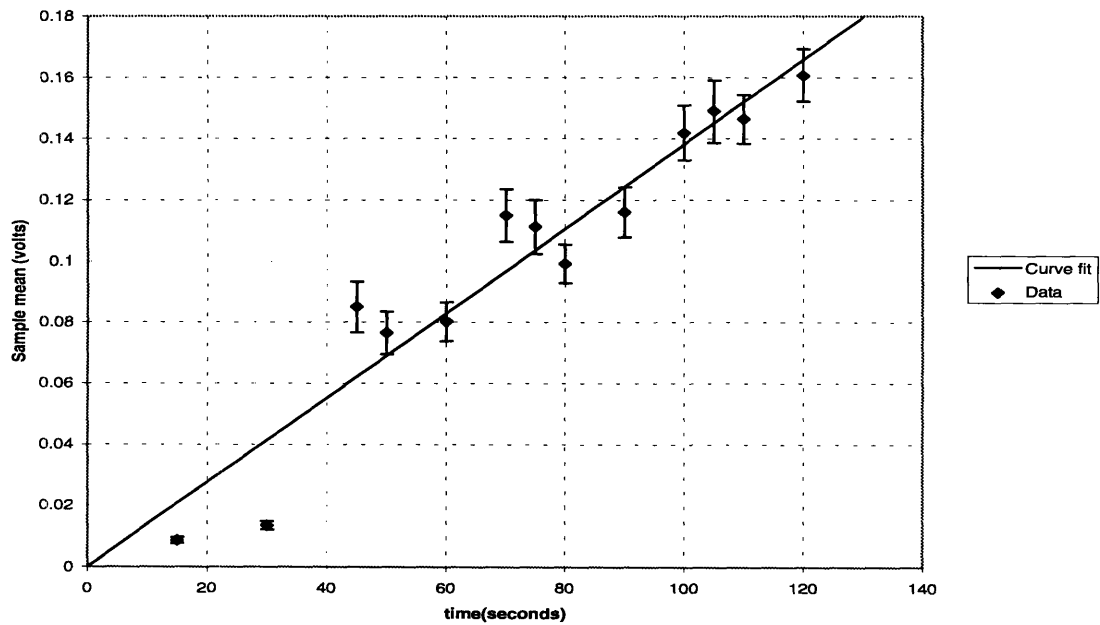


Figure 6.7: Mean voltage versus time

The error bars represent a 95% uncertainty level. The reader is referred to Appendix C for more information on how they were calculated. The majority of the data points fall within range of the curve fit which is made to go through the origin. The first two points (15 sec, 30 sec), are out of range. A reason for this may be the fact that these times are too low. There may not be enough deposition on the surface to cause a signal every time. This would result in a low value for the mean voltage recorded. The background noise level is approximately constant at 1-2 millivolts. This constant value results in the variance in the deposition being fairly low and so the standard deviation for these two points would also be low.

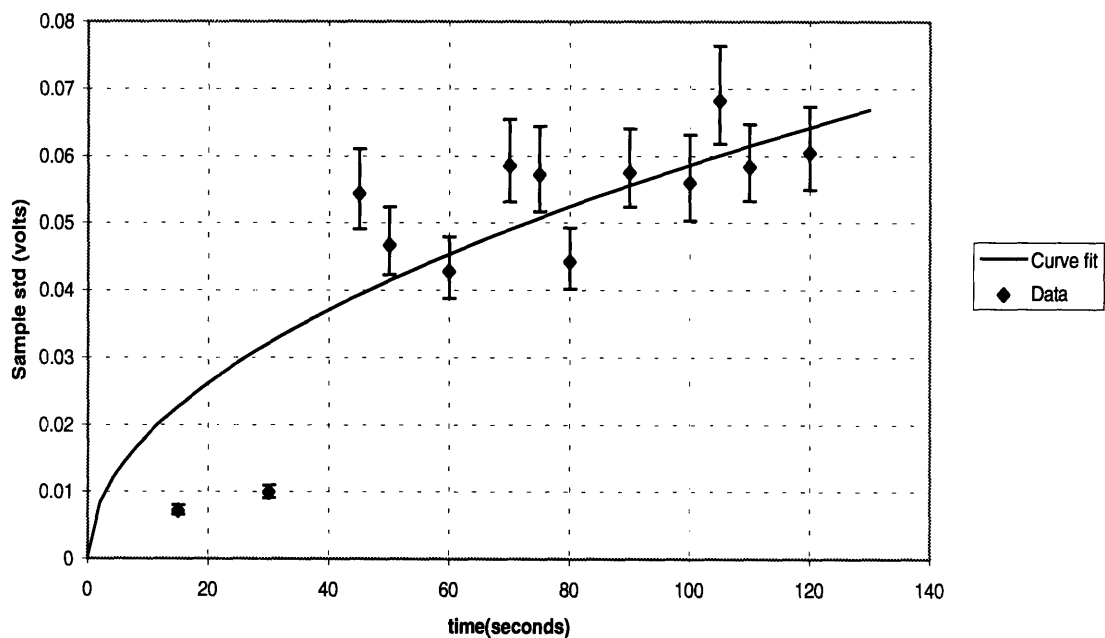


Figure 6.8: Standard deviation versus time.

The curve fit is made to go with the square root of time through the origin. The error bars are calculated using a chi-square test with a 95% uncertainty level. As predicted the

two run times at 15 and 30 seconds are out of range. This is probably due to the constant background noise level stabilizing the standard deviation at these low run times.

Finally if the standard deviation to mean ratio is plotted the following graph is obtained:

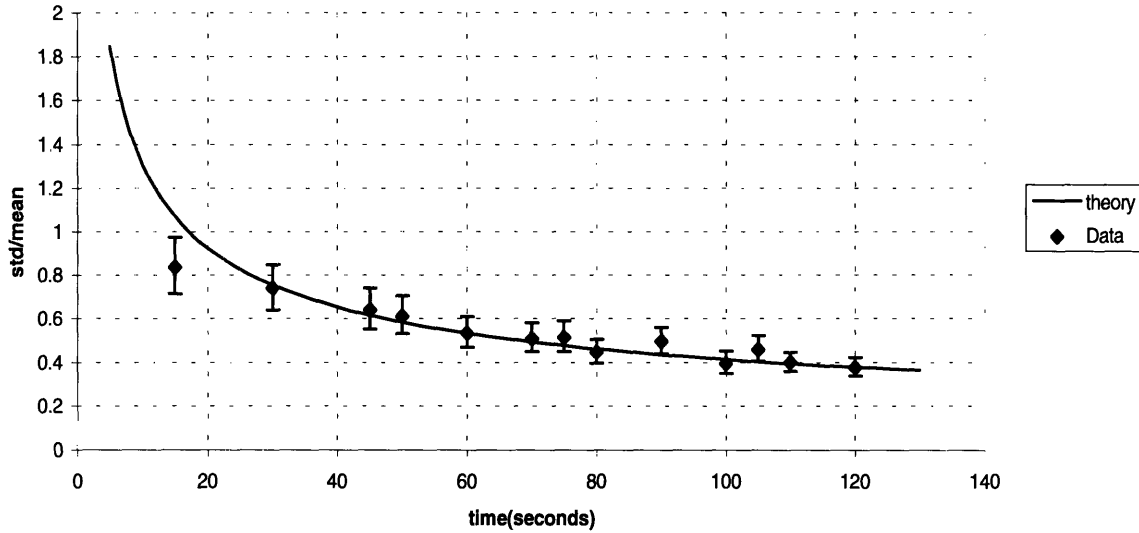


Figure 6.9: Standard deviation to mean ratio versus time.

The analytical curve is obtained using our model with a value for lambda, λ of $0.1172 \text{ particles/mm}^2/\text{second}$. The data appears to fit this curve accurately. The first two points fit because their mean and standard deviation were both low so the negative effects from this cancelled. Therefore, they both fit more from luck than any experimental achievement. Using this value for lambda and our criterion for convergence that

$$\frac{\sigma}{\mu} \leq 0.1$$

yields the following equation,

$$0.1 = \frac{1}{\sqrt{0.1172 \cdot 0.5 \cdot T}}$$

which gives a value for time of 1702 seconds or approximately 30 minutes. This is the time it will take to deposit $200 \text{ particles/mm}^2$ in the test section. Once again it is not possible to run an experiment for such a long time due to the oil forming layers instead of discrete droplets and due to the constraints of the nebulizer generator.

The results do show good agreement with theory. The fact that evaporation is not important is a significant factor. This was the main reason why it was decided to run these experiments. These results, taken together with those for the fluorescein-water system, show that the statistical convergence model is substantially independent of the physical characteristics of the deposited aerosol provided that reasonable precautions are taken to avoid phenomena such as drying, or flow of the deposited liquid. There is every reason to believe that the statistical model will apply equally well, or better, to solid aerosols.

Once again the convergence ratio which would limit the percentage error in the sample mean to 10% is given by equation (4.15), and for the sample size, $N = 210$, this gives

$$\frac{\sigma_n}{\mu_n} = 0.1 \left(\frac{\sqrt{210}}{1.96} \right) = 0.739$$

This value is reached after 31.2 seconds which is very reasonable. If on the other hand, 9 points per sample were used, the required run time would be over 12 minutes, which is over 23 times longer than the first case.

Chapter 7

Uncertainties in LIF calibration

The LIF instrumentation was calibrated to enable the user convert the voltage reading to a mean deposition thickness. Different types of deposition can yield different calibration constants. If the aerosols have high surface tension between the liquid and solid medium they will tend to form spherical shaped droplets. There exists evidence to suggest that these particles may have a different calibration constant to those with low contact angles that spread out and form thin layers across the surface. This chapter discusses these ideas in more detail.

7.1 Particle arrival rates

From eq.(4.12) the value of λ can be calculated from the formula:

$$\left(\frac{\mu_n}{\sigma_n}\right)^2 \frac{1}{AT} = \lambda \quad (7.1)$$

The constant λ has the dimension of the number of particles arriving per unit area per unit time. It is related to the number density of particles in the channel. Another model for estimating the number of particles/area/time is to use the mean voltage of the LIF to compute a mean thickness of aerosol deposition along the channel. Multiplying this by the laser probe area ($0.5mm^2$) gives the average volume in the laser probe. Using the PDPA to get the average volumetric diameter of each particle and dividing this into the laser probe volume gives the average number of particles that have landed in the laser probe area. Then dividing by the length of time of the experiment and the probe area gives the number of particles arriving/ per unit time/ per unit area.

There are a number of uncertainties in this model. There is a degree of uncertainty with the PDPA measurements. The mean particle diameter has a large error associated

with it. The polydispersity of the flow will affect the model, as will evaporation. Therefore this model is not highly accurate but it could be used to compare both values of λ and to check the relationship between voltage and deposition thickness. From the second model we have that:

$$\lambda = \frac{(\mu/k) Area}{\frac{\pi}{6} (d_p)^3 AT} \quad (7.2)$$

where μ is the average voltage recorded on the LIF, and:

k is the calibration constant for the LIF in $(mV) / (\mu m)$;

Area is the laser probe area in μm^2 ;

d_p is the mean volumetric diameter of the particles in μm . Taken from PDPA;

A is the laser probe area in mm^2 ;

and T is the experimental run time in seconds.

In order to calibrate the LIF, a procedure was developed by Nowicki [27]. Metal shims of thicknesses, $25.4\mu m$, $50.8\mu m$, $76.2\mu m$ were used to create liquid films. Aerosol liquid was placed in the hole in the shim and a microscope slide was secured on top, figure (7.1). The fluid was compressed to the shim thickness and the voltage was recorded.

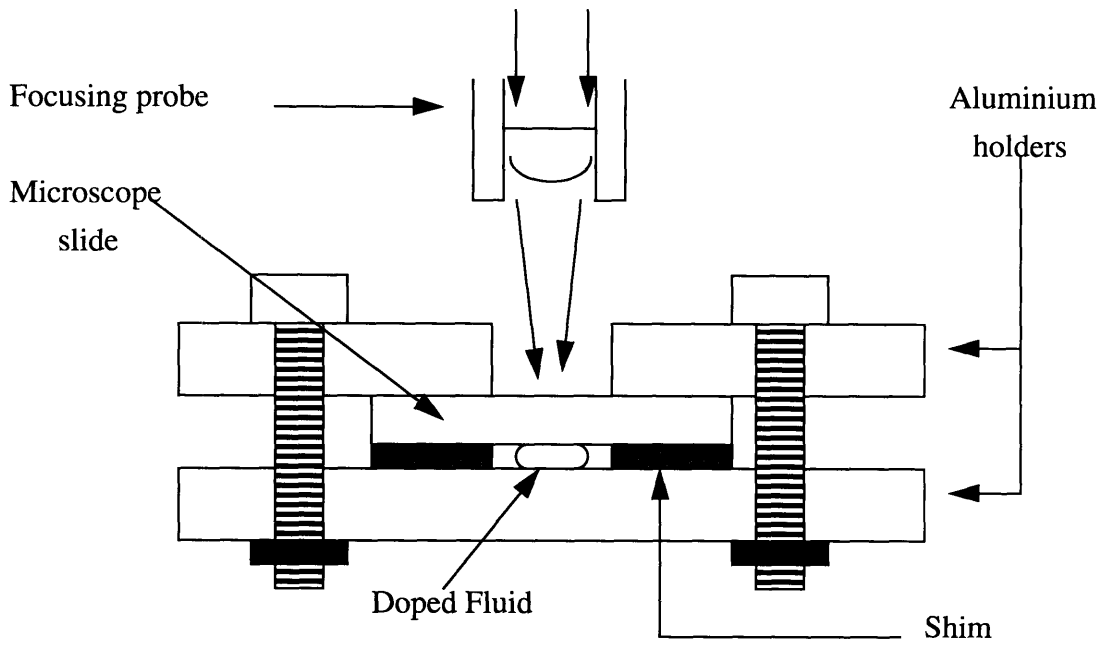


Figure 7.1: Calibration technique for LIF (from Nowicki [27])

The results for this calibration procedure are presented below for various different concentrations of fluorescein in water.

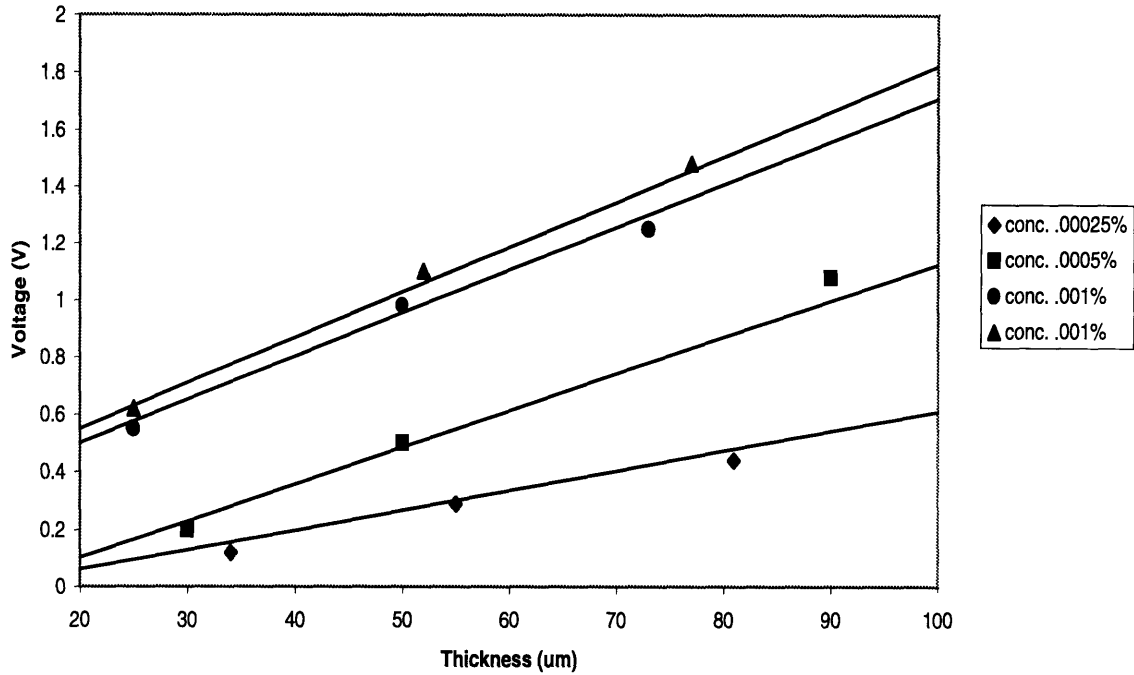


Figure 7.2: Calibration curves for fluorescein in water at a laser power of 0.1mW (from Nowicki [27]).

For our experiments the concentration of fluorescein was always kept at 0.001% by weight. With an output laser power of 0.1mW this gave an average calibration constant of 15.5mV/ μ m.

Once the calibration constant has been determined it is now possible to compare the two models above for their values of particle arrival time. If figure 5.4 and figure 5.8 from chapter 5 are taken as random figures. They will be used to compare the models. From eq.(7.1) we have that:

$$\lambda = \left(\frac{\mu_n}{\sigma_n}\right)^2 \frac{1}{AT}$$

From figure 5.4:

$$\mu_n = 0.766V$$

$$\sigma_n = 1.7358V$$

A is 0.5mm^2 and T is 210 seconds.

$$\lambda = \left(\frac{0.766}{1.7358} \right)^2 \frac{1}{(0.5) \cdot (210)} \quad (7.3)$$

$$\therefore \lambda = 1.855 \times 10^{-3} \text{particles}\backslash\text{mm}^2\backslash\text{sec} \quad (7.4)$$

Using eq.(7.2) with $k = 15.5\text{mV}/\mu\text{m}$ and $d_p = 58\mu\text{m}$ to get a second estimate of the particle arrival rate:

$$\lambda = \frac{(766.1/15.5) (500,000)}{\frac{\pi}{6} (58)^3 (0.5) (210)} \quad (7.5)$$

$$\therefore \lambda = 2.304 \text{particles}\backslash\text{mm}^2\backslash\text{sec} \quad (7.6)$$

Comparing these two values of λ reveals that the second value is 1242 times greater than the first. This result is unexpected. A difference of a factor of 10 might be acceptable but certainly not a factor of 1242. If the results from figure 5.8 are used similar results are obtained. The mean for this experiment is 1.1918V, and the standard deviation is 1.6625V, and the run time is 360 seconds. Using the first model we get:

$$\lambda = \left(\frac{1.1918}{1.6625} \right)^2 \frac{1}{(0.5) \cdot (360)} \quad (7.7)$$

$$\therefore \lambda = 4.2825 \times 10^{-3} \text{particles}\backslash\text{mm}^2\backslash\text{sec} \quad (7.8)$$

If the second model is used instead to give:

$$\lambda = \frac{(1191.8/15.5) (500,000)}{\frac{\pi}{6} (58)^3 (0.5) (360)} \quad (7.9)$$

$$\therefore \lambda = 3.136 \text{particles}\backslash\text{mm}^2\backslash\text{sec} \quad (7.10)$$

Comparing eq.(7.8) with eq.(7.10) it can be seen that they differ by a factor of 732 which is still far too high. In fact all the other experiments reveal similar results. The two models never fall within a factor of 100 of each other no matter what test is taken.

In order to explain the large discrepancies it is necessary to look more closely at the way the LIF system was calibrated. A flat thin liquid layer of doped fluid was gradually

increased and the successive voltages recorded. However the deposited aerosols do not form a flat layer. They take on the shape of a hemisphere. The contact angle between the water and the sintra force the droplets into hemispheres.

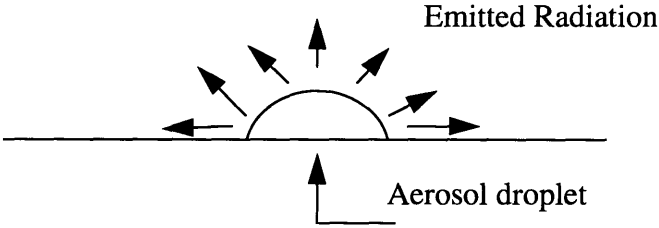


Figure 7.3: Emitted light from an aerosol droplet excited by laser source.

The emitted light from the droplet spreads in all directions and a percentage is intercepted by the optical array from the LIF. Does the fraction of light reaching the optics change as the size of the droplet increases? If we model the droplet / ring configuration as being a disk to a parallel coaxial annular ring, i.e.

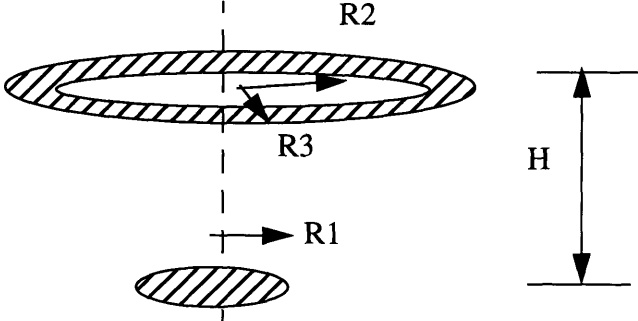


Figure 7.4: View factor configuration.

A coaxial annular ring is used to model the ring of optics which surrounds the laser beam and the aerosol droplet is modelled by the disk. The view factor for this configuration is given by the following formula, [22]:

$$F_{1-2} = \frac{1}{2} \left\{ R3^2 - R2^2 - \left[(1 + R3^2 + H^2)^2 - (4 \cdot R3^2) \right]^{\frac{1}{2}} + \left[(1 + R2^2 + H^2)^2 - (4 \cdot R2^2) \right]^{\frac{1}{2}} \right\} \quad (7.11)$$

H is the distance between the optics and the surface, R2 is the inner diameter of the optical ring while R3 is the outer diameter. For our situation, H is $26000\mu m$, R2 is $535\mu m$ and R3 is $635\mu m$. If R1 is allowed to vary between 0 and $400\mu m$ the resulting change in view factor is shown below.

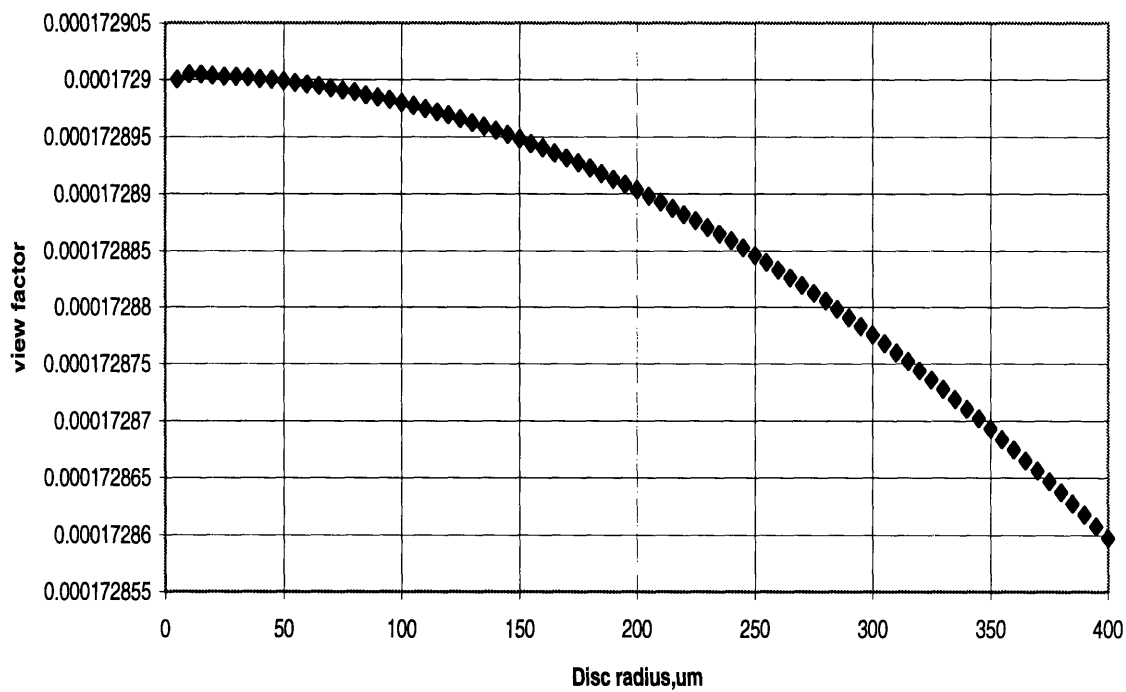


Figure 7.5: View factor versus disc radius.

The view factor does change as the area of the disc increases but this change is very small. The overall change in view factor between a disc radius of $5\mu m$ and a radius of $400\mu m$ is less than 0.025%. Therefore the view factor does not play a significant role in this setup and for all purposes can be treated as a constant, (0.000173). This insensitivity is mainly the result of the large value for H.

The emitted light from the droplet enters the optical receiving lens of the LIF. This light is proportional to the view factor (constant) times the surface area of the droplet times the droplet thickness. Therefore the voltage signal is also proportional to these quantities, i.e.

$$V \propto C_1 \cdot A \cdot t \quad (7.12)$$

Where A, is the surface area and t, the thickness and C_1 is a constant representing the view factor. The radius r, of the deposited aerosol can be modelled as being proportional to the aerosol thicknesses, t.

$$r \propto C_2 \cdot t$$

And the surface area (of a hemisphere) is given by:

$$A = \pi \cdot r^2$$

Putting these two results into eq.(7.12) gives;

$$V \propto C_1 \cdot \pi \cdot (C_2 \cdot t)^2 \cdot t$$

$$\Rightarrow V \propto C_3 \cdot t^3 \quad (7.13)$$

$$\Rightarrow V^{1/3} \propto t \propto r \quad (7.14)$$

Therefore for a hemispherical sphere it would appear the cubed root of the voltage is proportional to the thickness of deposition. The calibration technique used thin films of water with fixed area A, rather than spherical droplets, and so the voltage was directly proportional to the shim thickness. The above relationship would also hold even if the droplets were not completely hemispherical. Only the constant C_3 would change. This evidence suggests that the cubed root of voltage should be used to calculate film thicknesses. A new calibration technique is needed which will produce a calibration constant with a dimension of $(mV)^{1/3}/(\mu m)$.

7.2 LIF calibration

In order to try and establish a more accurate calibration procedure for the LIF system the following procedure was implemented. A droplet of water with fluorescein of known volume was placed on the sintra surface with a micro-syringe. The laser was focused directly over the droplet and the voltage was recorded. This was repeated for various droplet sizes and a graph was plotted of particle radius versus cubed root of voltage.

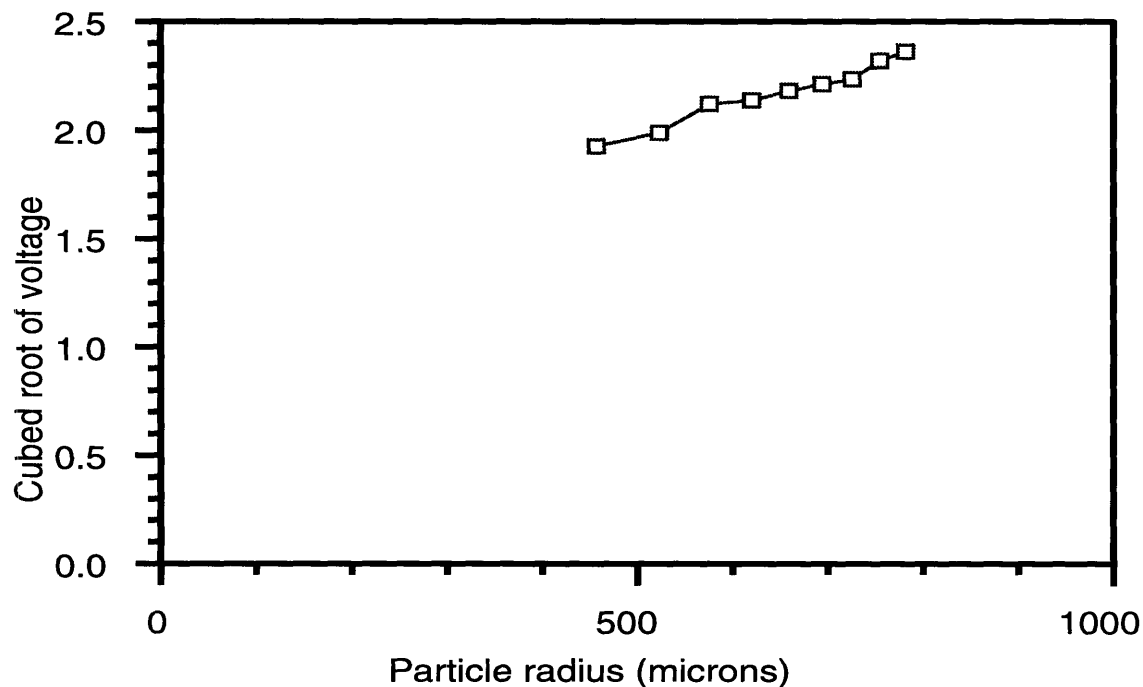


Figure 7.6: Cubed root of voltage versus particle thickness/radius.

The particle radius was found by assuming the droplet formed a hemisphere on the surface. Since the volume is known the radius can easily be found. The above graph appears to show the cubed root of voltage being proportional to the droplet radius. However this is slightly misleading as the range of radii examined is quite narrow. The reason for this is that larger droplets were too big to fit completely inside the laser probe and so could not be tested while smaller droplets evaporated too quickly for their true signal to be

recorded. The non-uniformity of the intensity of the laser beam was also a problem. The signal would vary depending on where the droplet was placed in the beam. Therefore it was always placed in the centre of the beam for consistency.

The slope of the above graph is $0.0111 (mV)^{1/3} / (\mu m)$. Using that calibration constant does not cause the two models to converge. They still differ from each other by a factor of over 1000. To illustrate why that calibration constant gives remarkably similar results to the first calibration constant the following graph is plotted.

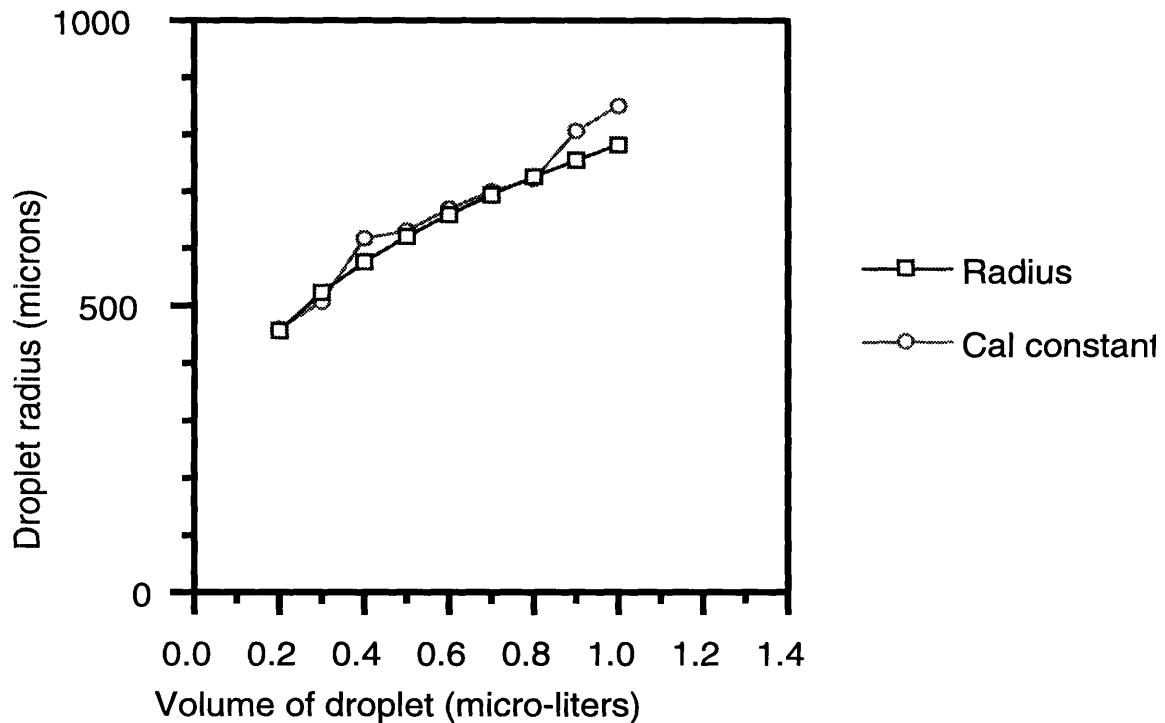


Figure 7.7: Droplet radius versus volume.

The volume of each droplet (plotted on the x-axis) is known from the syringe. The first radius (square boxes) is calculated from the volume of a hemisphere:

$$Vol = \frac{2}{3}\pi r^3$$

The second radius (circles) is calculated by dividing the direct voltage signal from the LIF by the calibration constant ($15.5 \text{ mV}/(\mu\text{m})$). In this range of radii this calibration constant gives almost the exact radius of each droplet. It would be expected then that both calibration constants, $15.5 \text{ mV}/(\mu\text{m})$ and $0.0111 (\text{mV})^{1/3}/(\mu\text{m})$ give similar results for the particle arrival rates. Its important to note that the range of radii examined is quite narrow and the particle size is 10 times larger than the average aerosol size produced by the AG. It is therefore not possible to estimate how the two signals vary as the aerosol diameters get smaller. The first curve (square boxes) will curve down sharply as the volume decreases since it is proportional to the cubed root of the volume. The second plot (circular markers) does not appear to be as curved as the first. If it is a straight line, then the results from its calibration constant ($15.5 \text{ mV}/(\mu\text{m})$) will be inaccurate at lower droplet diameters.

7.3 Oil experiments

Another way of examining the theory that the cubed root of the voltage is proportional to the deposition thickness, for liquid aerosols with high surface tension, is to use oil in the experiments instead of water. Oil droplets have the advantage of not evaporating and secondly they spread out when they deposit due to the lower surface tension between the oil and the sintra. The droplets form a film on the surface and since the calibration technique uses a film of liquid both values for λ should agree relatively well.

In section 6.3 the possibility of using the dye oil-glo which fluoresced underneath the laser light (488nm) was discussed. The dye was dissolved in the lubricating oil velocite-6. A calibration was carried out on the oil and dye. The procedure was the exact same as demonstrated in figure 7.1 and the results are presented below.

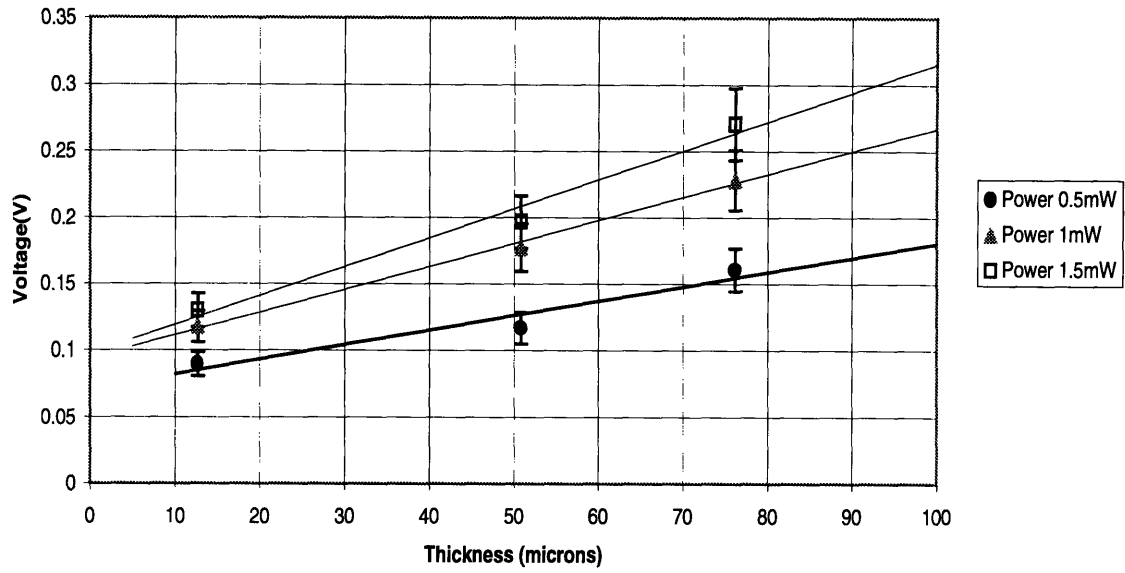


Figure 7.8: Calibration curves for oil glo at a concentration of 0.01% by volume.

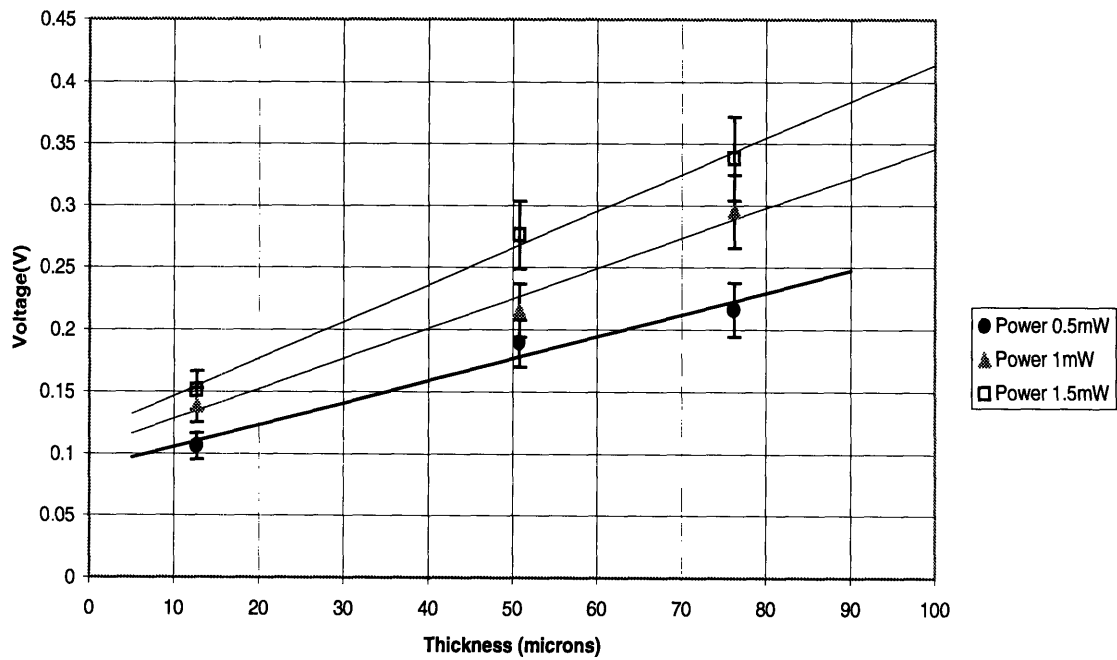


Figure 7.9: Calibration curves for oil glo at a concentration of 0.02% by volume.

The above two graphs are calibration curves for two different concentrations of oil glo. Each plot has three different lines which represent three different laser powers. The laser power was read from the lasers own internal power meter. The line which gave the strongest signal was obviously the 1.5mW laser power with an oil glo concentration of 0.02%. This line has a slope of $2.97\text{mV}/(\mu\text{m})$ which is still five times less sensitive than the $15.5\text{mV}/(\mu\text{m})$ slope that exists between fluorescein and water. It is however strong enough to be detected and was used for the experiments.

The compressed air nebulizer (see fig.(2.7)) was used to generate the oil aerosols. The velocity and diameter distributions of water particles generated by the nebulizer are shown in figure.6.2 and figure.6.3 respectively. The average velocity is 7.14m/s and the average volumetric diameter is $104.5\mu\text{m}$.

Another more serious problem was the effect the oil had on the wind tunnel. It penetrated into the lining of the tunnel and caused it to begin to peel off. After an experiment the tunnel had to be very thoroughly cleaned and the lining reset. This is a satisfactory method for the short term but in the longer term the oil will cause severe erosion and decay.

From the previous experiments with oil, the 120 second run was arbitrarily chosen as the experiment to be examined. The oil droplets deposited along the surface but spread out like films instead of forming hemispherical shaped droplets. The frequency histogram for the distribution is shown below.

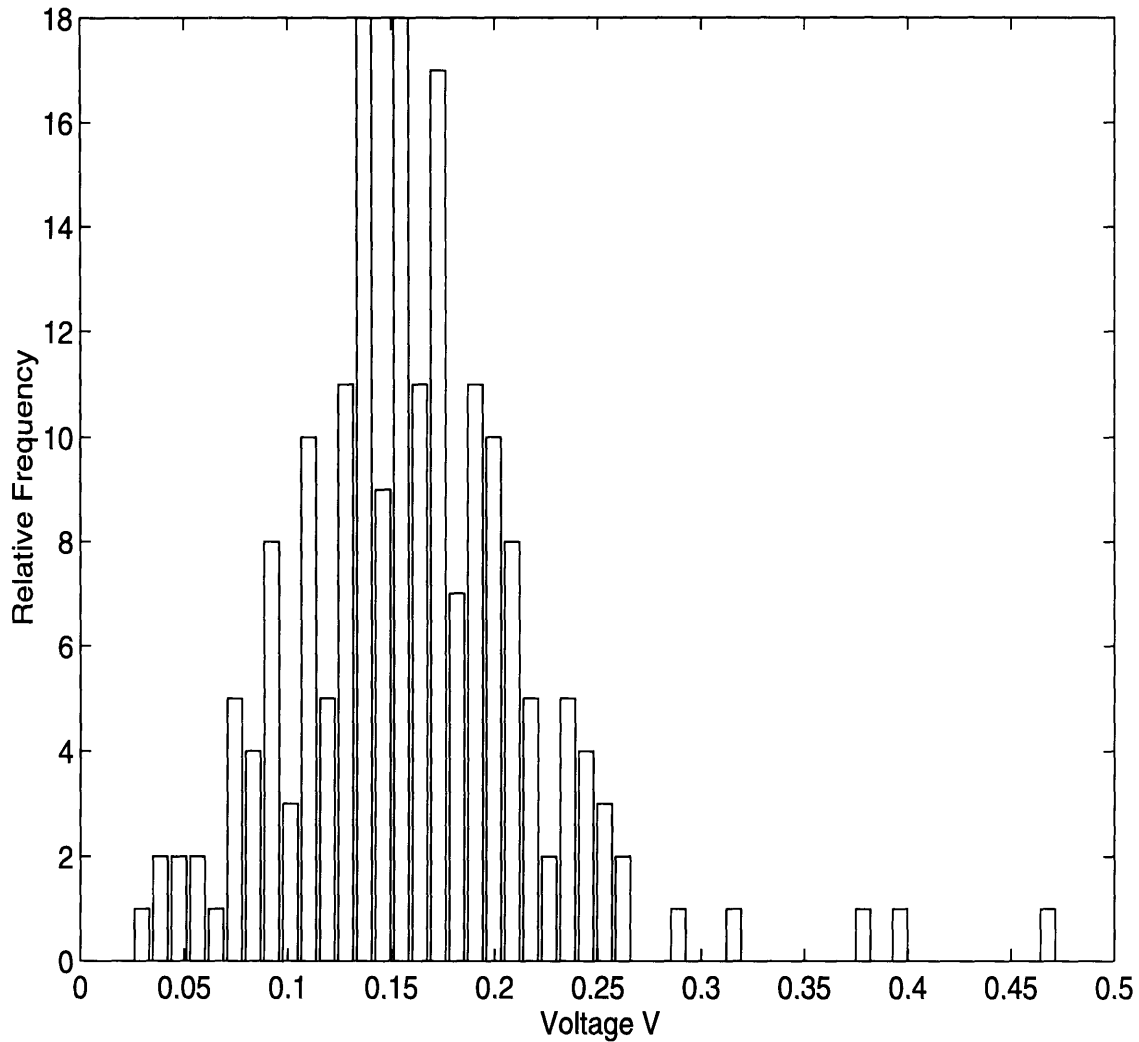


Figure 7.10: Frequency histogram for an experimental run time of 120 seconds.

The mean LIF voltage for this experiment is 160.6mV and the standard deviation is 60.4mV. Using eq.(7.1) this experiment has a particle arrival rate of:

$$\lambda = \left(\frac{160.6}{60.4} \right)^2 \frac{1}{0.5 \cdot 120} \quad (7.15)$$

$$\lambda = 0.1178 \text{ particles} \cdot \text{mm}^2 \cdot \text{sec} \quad (7.16)$$

From the second model for λ (eq.(7.2)) this experiment gives the result:

$$\lambda = \frac{(160.6/2.97) \cdot 500,000}{\frac{\pi}{6} (104.5)^3 (0.5) (120)} \quad (7.17)$$

$$\Rightarrow \lambda = 0.754 \text{ particles} \backslash \text{mm}^2 \backslash \text{sec} \quad (7.18)$$

Here the calibration constant is taken as $2.97 \text{ mV} / (\mu\text{m})$ and the mean volumetric diameter as $104.5 \mu\text{m}$. Equation 7.16 and 7.18 differ from each other by a factor of 6.5. This is not a large factor considering the case with water and fluorescein was three orders of magnitude apart. The factor of 6.5 could result from the oil not forming a perfect film on the surface, the laser power drifting during measurement taking, the concentration of oil glo in solution being different to 0.02% and variations over time in particle number density in the channel due to the nebulizer. This gives very strong evidence to suggest that the reason the two separate models for λ were not compatible for water based droplets is because of the curvature of the droplets on the surface as well as the more standard reasons such as evaporation, statistical errors, calibration errors and errors in estimated particle size.

7.4 Summary

There exists evidence to suggest that calibrating the LIF system for a thin liquid film is not adequate to yield thicknesses for deposited spherically shaped aerosols. The evidence for this comes from 4 sources:

Totally different values for the particle arrival rate from the two λ models

Radiation emitted from a spherical surface arguments

Individual droplet calibration techniques, (figure.(7.7))

Experimental oil results.

These suggest that the cubed root of voltage is proportional to the thickness of deposition for a spherical droplet. However none yield a specific value for this calibration constant. The modelling assumption for the original calibration procedure was that the voltage was proportional to the volume of the mixture in the probe area.

$$V \propto vol \quad (7.19)$$

If the volume is varied by varying the thickness, as in the calibration procedure, then the voltage will be proportional to the thickness. For a hemispherical droplet it was shown that the voltage is proportional to the radius cubed, eq.(7.13).

$$V \propto r^3$$

The volume of the hemisphere is given by;

$$vol = \frac{2}{3}\pi r^3$$

Therefore combining these two results yields that the voltage is also proportional to the volume of mixture in the probe area for a hemispherical droplet. Therefore the theory behind the LIF calibration is correct. The voltage is proportional to the volume of fluorescent material in the probe area. The important factor is the way the thickness varies with varying volume. If the volume is shaped like a cylinder (as in the calibration technique) then the thickness is directly proportional to volume but if it is shaped like a sphere then the thickness cubed is proportional to the volume. It should therefore in theory be possible to obtain one universal calibration constant relating the voltage to the volume. This was attempted in figure.(7.6). The droplets are large (400 - 800 μm) so laser power non-uniformity caused problems. The slope from this curve was 0.0111 $mV^{1/3}\mu m$. Cubing this gives a value of $1.36 \times 10^{-6} mV\mu m^3$. This has the correct dimensions of a universal calibration constant. The original constant of 15.5 $mV\mu m$ can be used to try and validate this. If this value is divided by the laser probe area in μm^2 ,

$$\frac{15.5}{500,000} = 3.1 \times 10^{-5} mV\mu m^3$$

This 'universal constant' differs from the first one by a factor of 22.7. This can be accounted for by reasons such as, droplet evaporating during calibration, non-uniform laser intensity, different sized droplets and inaccuracies in the shim thicknesses.

It is still not known which of the previous calibration constants are correct. It would appear that a universal calibration constant that relates voltage to volume may need more work to quantify accurately.

Conclusions

The motivation behind this thesis was to examine the statistical convergence of aerosol deposition. This was done by measuring the standard deviation to mean ratio for a fixed particle deposition rate in a turbulent channel flow at different times. A model was developed which related these quantities together, eq.(4.12).

$$\frac{\sigma}{\mu} = \frac{1}{\sqrt{\lambda AT}}$$

Computer simulations were performed which indicated the validity of this model. They also indicated that aerosol polydispersity had a small effect on convergence and that our sample size of over 200 points were enough to calculate a sample mean that was sufficiently close to the true mean. Experiments were carried out both with water and oil and the results for both agreed very well with the above model. However the ratio, $\frac{\sigma}{\mu}$, failed to converge to an acceptably small value of 0.1. The simulation and experiments both predicted very long times to converge or else very high particle deposition rates. Neither the times or the number densities were achievable in practice.

It would seem a fair assumption then to treat turbulent aerosol deposition like turbulent fluid velocities. It is not possible to sample turbulence at a point in the flow and correlate that velocity to the flow field velocity. The turbulent velocity must be sampled at several points over the entire flow field and a statistical average taken. The same applies for aerosol deposition. It is not possible to sample the deposition at a point. The deposition must also be sampled at several points and a statistical average taken.

The LIF system developed is capable of measuring deposition at a small area, ($0.5mm^2$). However measurements at a point are insufficient to obtain an overall flow dep-

osition rate. A larger area has to be sampled and a sample mean taken. In this regard the LIF system is very useful as large samples (~ 150) can be taken over small areas, ($\sim 1\text{ cm}^2$).

Evaporation effects were dealt with. Various surfactants when added to the water fluorescein mixture were found to actually increase the evaporation rate. The two most effective methods of reducing evaporation effects during our experiments were to use a liquid with a low vapor pressure such as oil or to humidify the channel by increasing the aerosol number density inside it.

The calibration procedure for the LIF system presented problems. It is reasonably certain that the intensity of the returning signal is proportional to the laser power, the concentration of fluorescent dye in the liquid and the volume of liquid in the probe area. However the droplet shape (e.g. flat or spherical) may also effect the signal strength. Until this phenomena is more clearly understood the particle arrival rate from the statistical model, λ may not be used to calculate particle arrival rates unless solid monodisperse particles are used for aerosols. This is because, λ may be affected by other unexplained phenomena such as polydispersity, droplet spreading and surface curvature effects. However once the experimental conditions remain constant (e.g. type of aerosol, deposition surface, sampling technique, etc.) then λ can be calculated and used to estimate the convergence rate over time for that exact experimental procedure.

References

- [1] Abuzeid, S., Busnaina, A.A. and Ahmadi, G. (1991) "Wall deposition of aerosol particles in a turbulent channel flow." J. Aerosol Sci., Vol. 22, No.1, 43-62
- [2] Beckwith, T.G., Marangoni, R.D. and Lienhard, J.H. (1993) Mechanical Measurements. (Addison-Wesley, Massachusetts)
- [3] Bendat, J.S. and Piersol, A.G. (1971) Random Data: Analysis and Measurement Procedures. (John Wiley & Sons, New York).
- [4] Benjamin, J.R. and Cornell, C.A. (1970) Probability, Statistics and Decision for Civil Engineers. (McGraw-Hill, New York).
- [5] Bixler, A.D. (1989) "The circulating fluidized bed combustor challenge." EPRI CFB Materials Workshop, Argonne Illinois, June 19-23, 1989.
- [6] Child, M.S. (1992) "The Design, Fabrication and Testing of a Wind Tunnel for the study of the Turbulent Transport of Aerosols." S.B.Thesis, Department of Mechanical Engineering, M.I.T, February, 1992.
- [7] Colmenares, J. (1992) "Measurement of the Velocity Response of Inertial Aerosols in Grid-Turbulence and in Channel Flow." S.M. Thesis, Department of Mechanical Engineering, Massachusetts Institute of Technology, February, 1992.
- [8] Cooper, D.W. (1986) "Particulate contamination and microelectronics manufacturing: an introduction." Aerosol Sci. Technol. 5, 287-299
- [9] Crow, F.R. (1961) "Reducing Reservoir Evaporation." Agricultural Engineering, Vol.42, No.5, pp. 240-243.
- [10] Crow, F.R. and Mitchell, A.L. (1975) "Wind effects on chemical films for evaporation suppression at Lake Hefner." Water Resources Research, Vol.11, No.3, pp. 493-495.
- [11] Davies, C.N. (1978) Fundamentals of Aerosol Science. (Wiley, New York)
- [12] Eisner, H.S., Quince, B.W., and Slack, C. (1960) "The stabilization of water mists of insoluble monolayers." Disc. Faraday Soc. No.30, pp. 85-95.
- [13] Elsner, R.W. and Friedman, M.A. (1989) "CFB Materials related issues at CUEA nucla station." EPRI CFB Materials Workshop, Argonne Illinois, June 19-23, 1989
- [14] Exciton, personal communication

- [15] Feller, W. (1957) An Introduction to Probability Theory and its Applications. (John Wiley & Sons, New York).
- [16] Feng, M.Y. (1993) "Ultrafine aerosol deposition in planar channel flow." B.S. Thesis, Department of Mechanical Engineering, M.I.T., 1993.
- [17] Fluid Jet Associates(1993) "Operating instructions for basic drop generator."
- [18] Friedlander, S.K. (1957) Smoke, Dust and Haze: Fundamentals of Aerosol Behavior. (Wiley & Sons, New York: New York).
- [19] Fuchs, N.A. (1964) The Mechanics of Aerosols. (Pergamon Press, New York).
- [20] Hinds, William C. (1982) Aerosol Technology: Properties, Behavior and Measurement of Airborne Particles. (Wiley, New York).
- [21] Hoult, David P., Shaw II, Byron, T. and Wong, Victor W. (1992) "Development of engine lubricant film thickness diagnostic using fiber optics and laser fluorescence." SAE Paper #920651, 1992, SAE Transactions, vol. 101.
- [22] Howell, J.R. (1982) A Catalog of Radiation Configuration Factors. (McGraw-Hill, New York)
- [23] Kim, C.S., Lewars, G.G., Eldridge, M.A., and Sackner, M.A. (1984) "Deposition of aerosol particles in a straight tube with an abrupt obstruction." J. Aerosol Sci., vol. 15, no. 2., pp. 167-176.
- [24] Lienhard, John H. (1987) A Heat Transfer Textbook. (Prentice-Hall, Englewood Cliffs, New Jersey, second edition).
- [25] Miller, J.R. (1989) "Operating experience on a 19MW CFBC." EPRI CFB Materials Workshop, Argonne Illinois, June 19-23, 1989.
- [26] Nielsen, L.K., Smyth, G.K., Greenfield, P.F. (1991) "Hemocytometer cell count distributions: Implications of non-poisson behavior." Biotechnol. Prog., Vol. 7, No. 6, pp. 560-563.
- [27] Nowicki, J.L., (1994) "A laser induced fluorescence system to quantify aerosol deposition." S.M. Thesis, Department of Mechanical Engineering, M.I.T., February, 1994.
- [28] Roth, K.W.,(1995) "Deposition and dispersion of inertial aerosols in secondary and turbulent flow structures." Ph.D. Thesis, Department of Mechanical Engineering, Massachusetts Institute of Technology, February, 1995.
- [29] Smeltzer, C.E., Gulden, M.E. and Compton, W.A., (1969) "Mechanisms of metal removal by impacting dust particles." ASME Paper No. 69-WA/Met-8.

- [30] Snead, C.C. and Zung, J.T., (1968) "The effects of insoluble films upon the evaporation kinetics of liquid droplets." Journal of Colloid and Interface Science, Vol.27, No.1, pp. 25-31.
- [31] Sweeney, T.D., Blanchard, J.D., Zeltner, T.B., Carter, J.E. and Brain, J.D. (1990) "Delivery of aerosolized drugs to the lungs with a metered-dose inhaler: Qualitative analysis of regional deposition." J. Aerosol Sci., vol. 21, pp. 350-354.
- [32] Tabakoff, W., Hamed, A., Metwally, M. (1991) "Effect of particle size distribution on particle dynamics and blade erosion in axial flow turbines." J. of Eng. for Gas Turbines and Power, vol. 113, p.607-615.
- [33] Tyagi, A., Bayoumi, M.A., (1991) "A generalized Poisson based model defect spatial distribution in wafer scale integration." International Conference on Wafer Scale Integration. San Francisco, Jan 29-31, 1991.
- [34] Willeke, K. and Baron, P.A. (1993) Aerosol Measurement: Principles, Techniques and Applications. (Van Nostrand Reinhold, New York).
- [35] Yoon, D.H., (1991) "Diameter distribution for a compressed air nebulizer atomizing system." B.S. Thesis, Department of Mechanical Engineering, M.I.T., February 1991.

Appendix A

A.1 Fortran code for numerics

This is the Fortran code written (by J.Moran) to simulation the particle deposition process and to estimate the statistical convergence rate numerically.

```
c This is declares all variables.
c
integer J, time, row1(100), col1(100), T, lambda
integer c, B, test(207,159,31), G, bin
real mdiam(207,159)
integer dia(31 ), number, y, lamba
real std
real rndnum, xx, xm, x, seed2
real a,m,i, num(30 ), mn, sum(207,159), rati
print*, 'Input a value for Lambda.'
read *, lamba
print *, 'Input a seed value for the random number generator'
read *, idum
print*, 'Input a value for the second seed generator.'
read *, seed2
c
print*, 'The distribution you are using comes from test 14.'
print*, ' '
print*, ' '
c
c For run 13 there are 31 bins.
c For run 14 there are 27 bins.
c For run 15 there are 26 bins.

bin = 27
c
c This reads in the relative frequency in the distribution of particles
c
open(2, file = 'count14.txt')
do 100 y=1,bin
read (2,*) count14
num(y) = count14
100 continue
```

```

c
c This reads in the diameter of particles in each bin.
c
c  print*, 'Input the diameter of particles in each bin.'
  open(3, file = 'diam14.txt')
  do 105 y=1,bin
  read(3,*) diam14
  dia(y) = diam14
105 continue

```

```

c
c This opens a file to put the output data into.

```

```

c
  open(8,file = 'output.txt')

```

```

c
c This calculates the total number of particles.

```

```

c
  number = 0
  do 110 y=1,bin
  number = number + num(y)
110 continue

```

```

c
c This normalizes our distribution.

```

```

  do 115 y=1,bin
  num(y) = num(y)/number
115 continue

```

```

  print *, '   Time:      Mean:      Std:      Ratio:'

```

```

c This loop calculates the mean, std and ratio for different times varying
c in increments of (say) 50 seconds apart.

```

```

  time = 200
6  if (time.GT.1200) go to 8

```

```

c this normalises the distribution

```

```

  do 120 y=1,bin
  lambda = lamba*num(y) + 1

```

c This section initialises the deposition matrix.

```
c
  do 40 J=1,207
  do 45 T=1,159
  test(J,T,y) = 0
45  continue
40  continue
```

c

c This loop increments the matrix by lambda every 'time' seconds.

c

```
  do 3 G = 1,time
```

c

c This generates random numbers in the rows of the matrix.

c

```
  Data a,m,i/1027,1048576,1/
  do 10 J=1,lambda
  if (i.EQ.1) then
  x = idum
  i = 0
  xm = m
  endif
  x = raa1(idum)*10000
  x = mod(a*x,m)
  xx = x
  rndnum = (xx/xm*207) + 1
  row1(J) = rndnum
  idum = rndnum*5126
10  continue
```

c

c This generates random numbers for the columns in the matrix.

c

```
  do 20 J=1,lambda
  if (i.EQ.0) then
c  idum = seed2
  x = seed2
  i = 1
  xm = m
  endif
  x = raa1(idum)*10000
  x = mod(a*x,m)
```

```

xx = x
rndnum = (xx/xm*159) + 1
coll(J) = rndnum
idum = rndnum*5378
20  continue

```

c

c This section just prints out the two lists of random numbers.

c This gives our deposition matrix Lambda random values every second.

```

do 50 T=1,lambda
J = row1(T)
B = coll(T)
test(J,B,y) = test(J,B,y) + 1
50  continue

```

```

3  continue

```

```

120 continue

```

c This section calculates the mean of the 210 selected points on the matrix.

```

mn = 0
c = 1
210 if(c.GT.207) go to 215
J = 1
220 if(J.GT.159) go to 225

```

```

sum(c,J) = 0
do 200 y = 1,bin
sum(c,J) = sum(c,J) + test(c,J,y)
200 continue
mdiam(c,J) = 0
do 205 y = 1,bin
mdiam(c,J) = mdiam(c,J) + (test(c,J,y)*dia (y))
205 continue

```

c if (sum(c,J).EQ.0) then

```

mn = mn + mdiam(c,J)

```

```

    J = J + 11
    go to 220
225  continue
    c = c + 15
    go to 210
215  continue
    mn = mn/210

    std = 0
    c = 1
230  if(c.GT.207) go to 235
    J = 1
240  if(J.GT.159) go to 245
    std = std + ((mdiam(c,J) - mn)**2)

    J = J + 11
    go to 240
245  continue
    c = c + 15
    go to 230
235  continue

    rati = std/mn

    print *, time, mn, std, rati

    write(8,*) time, mn, std, rati

    time = time + 20
    go to 6
8  continue

c This closes the data file.
c
    close(8)
    stop
    end

```

c This is the random number generator used as a function in Fortran.

```

function raa1(idum)
integer idum, IA, IM, IQ, IR, NTAB, NDIV
real raa1, AM, EPS, RNMX

parameter (IA=16807, IM=2147483647, AM=1./IM)
parameter (IQ=127773, IR=2836, NTAB=32, NDIV=1+(IM-1)/NTAB)
parameter (EPS=1.2e-7, RNMX=1.-EPS)

integer j,k,iv(NTAB), iy

save iv, iy
data iv/NTAB*0/, iy/0/
if (idum.LE.0.or.iy.EQ.0) then
idum = max(-idum, 1)
do 11 j=NTAB+8,1,-1
k=idum/IQ
idum = IA*(idum-k*IQ)-IR*k
if (idum.LT.0) idum=idum + IM
if (j.LT.NTAB) iv(j) = idum
11  continue
iy = iv(1)
endif
k=idum/IQ
idum = IA*(idum-k*IQ)-IR*k
if (idum.LT.0) idum = idum + IM
j = 1+iy/NDIV

iy = iv(j)
iv(j) = idum
raa1 = min(AM*iy, RNMX)

return

end

```


Appendix B

B.1 Quick Basic code for data acquisition system

The following program was written to control the DAS-8 data acquisition board by Andy Pfahnl and James Moran. The code used was Quick Basic.

```
'--- Sealing test program for DAS-8 used in array mode 5 ---  
'-----  
'  
    DIM d%(6)  
    COMMON SHARED d%()  
    DECLARE SUB das8 (mode%, BYVAL dummy%, flag%)  
    DIM a%(12000)  
  
    KEY OFF  
  
400 '--- Prompt user for data output file  
410 fa$ = "acp"  
420 PRINT : INPUT "enter file name (acp): "; f$  
430 IF f$ = "" THEN f$ = fa$  
435 '  
440 '---- Make data file  
445 'g1$ = "c:\"  
450 e1$ = ".dat"  
  
600 '--- Prompt user for desired sample rate  
610 fa = 400  
620 PRINT : INPUT "Enter desired sample rate (400 samples/sec) : ", f  
630 IF f = 0 THEN f = fa  
  
640 '--- Prompt user for duration of scan  
650 dsa = 1  
660 PRINT  
670 INPUT "Duration of scan (1 seconds) : ", ds  
680 IF ds = 0 THEN ds = dsa  
  
700 '--- Number of conversions = duration x sample rate
```

```

710 nc = (ds * f)

740 OPEN f$ + e1$ FOR OUTPUT AS #1
750 DO

800 '--- Initialize DAS-8, mode 0
810 B% = &H308           'Set this for correct base address
820 d%(0) = B%           'I/O address of DAS-8 (change to suit)
830 MD% = 0              'initialize mode
840 flag% = 0            'declare error variable
850 CALL das8(MD%, VARPTR(d%(0)), flag%)
860 IF flag% <> 0 THEN PRINT "Error in initialization": STOP

900 '--- Set timer rate, mode 10
910 MD% = 10
920 d%(0) = 2            'Operate on counter #2
930 d%(1) = 3            'Configuration #2 = rate generator
940 CALL das8(MD%, VARPTR(d%(0)), flag%)
950 IF flag% <> 0 THEN PRINT "Error in setting counter 2 configuration": STOP

1000 '--- Output frequency = 2386.4/N KHz
1010 n = (2386.4 / f) * 1000
1020 IF n < 2 OR n > 65535! THEN PRINT "Warning! A sample rate of "; f; " sam-
ples/sec is outside the range of Counter 2": GOTO 700
1030 MD% = 11            'Mode 11 to load counter
1040 d%(0) = 2            'Operate on counter #2
1050 IF n < 32767 THEN d%(1) = n ELSE d%(1) = n - 65536! 'correct for integer
1060 CALL das8(MD%, VARPTR(d%(0)), flag%)
1070 IF flag% <> 0 THEN PRINT "Error in loading counter 2": STOP

1100 '--- Set scan limits, mode 1
1105 MD% = 1
1110 PRINT : LL% = 0: d%(0) = LL%
1120 UL% = 0: d%(1) = UL%
1130 CALL das8(MD%, VARPTR(d%(0)), flag%)
1140 IF flag% <> 0 THEN PRINT "Error in setting channel scan limits": STOP

1200 '--- Acquire data, mode 5

```

```

1250 MD% = 5                'Mode 5, do conversions direct to array
1260 d%(0) = -1            'Set to -1 to indicate that d%(2) will have offset
                            'and d%(3) will have segment of array
1261 d%(2) = VARPTR(a%(0))
1262 d%(3) = VARSEG(a%(0))
1270 d%(1) = nc            'Number of conversions
1290 CALL das8(MD%, VARPTR(d%(0)), flag%)
1300 IF flag% <> 0 THEN PRINT "Error in setting mode 5"

2000 var = 0
2010 FOR i = 1 TO nc - 1
2020 var = (a%(i) / 2048) * 5 + var
2025 'PRINT i / f; ((a%(i) / 2048) * 5)
2030 NEXT i
2040 dat = (var / (nc - 1) * 3)
2045 PRINT dat
2050 PRINT : INPUT "press s to stop:", data$
2052 IF data$ = "" THEN
2053 pt = pt + 1
2054 PRINT #1, pt, ",", dat
2056 END IF
2060 LOOP UNTIL data$ = "s"
2070 CLOSE #1
2080 END

```

Appendix C

C.1 Uncertainty tests on sample mean and standard deviation

The error bars for the mean voltages were calculated using the student t-test at an uncertainty level of 95% and assuming a sample size greater than 30. The formula used was:

$$\bar{x} - \left(1.96 \cdot \frac{s_x}{\sqrt{n}} \right) < \mu < \bar{x} + \left(1.96 \cdot \frac{s_x}{\sqrt{n}} \right)$$

Where: μ is the true mean which confidence limits are applied to

\bar{x} is the sample mean

s_x is the sample standard deviation

n is the sample size (in this case between 200 - 240 points or samples)

In order to calculate the error bars on the sample standard deviation the chi-square test was used. This is slightly more complicated than the t-test. The limits on the true standard deviation squared or variance is given by:

$$\frac{(n-1) \cdot s_x^2}{\chi_{\alpha/2}^2} < \sigma^2 < \frac{(n-1) \cdot s_x^2}{\chi_{(1-\alpha/2)}^2}$$

Where: α is equal to one minus your uncertainty limit. Therefore in our case α is 5% or 0.05. The above formula is derived under the assumption that the variable χ_i , is Gaussian distributed; however, the central limit theorem ensures that it will apply to a Poisson distributed χ_i when the sample size n is large.

σ^2 is the true variance.

χ_x^2 for a sample size greater than 30 is given by the following expression.

$$\chi_x^2 = \frac{1}{2} \cdot (Z_x + \sqrt{2n-1})^2$$

Z_x is the standard normal distribution. For a 95% uncertainty level its value becomes equal to ± 1.96 .

The uncertainty level in the ratio, r , of the standard deviation to the mean, i.e. $\frac{s_x}{x}$ can be calculated directly from the uncertainty levels in both the standard deviation and the mean.

$$\begin{aligned} \frac{s_x \pm \Delta s_x}{x \pm \Delta x} &= r \pm \Delta r \\ \Delta r^2 &= \frac{\partial}{\partial s_x} r^2 (\Delta s_x)^2 + \frac{\partial}{\partial x} r^2 (\Delta x)^2 \\ &= \left(\left(\frac{r}{s_x} \right)^2 \cdot \Delta s_x^2 + \left(\frac{r}{x} \right)^2 \cdot \Delta x^2 \right) \\ \left(\frac{\Delta r}{r} \right)^2 &= \left(\frac{\Delta s_x}{s_x} \right)^2 + \left(\frac{\Delta x}{x} \right)^2 \end{aligned}$$

From the last equation the value of Δr can be calculated from all the other known quantities.